Table of contents

Materials and methods

Experimental

Unless otherwise noted, all reactions were run under an argon atmosphere in an oven-dried glassware. Reactions were stirred using Teflon-coated magnetic stir bars. Cyamerulic chloride was prepared according to the literature [1]. Melem was synthesized as small needles by heating melamine 12h at 450 °C, follow by sublimation of the crude product under high vacuum (diffusion pump) at 400°C. All other reagents and analytical grade solvents were obtained from commercial suppliers. Toluene was distilled over Na and THF over Na/benzophenon. AcN (Sigma Aldrich anhydrous) and DMSO (Sigma Aldrich anhydrous) was used as received. nBu_4PF_6 (Sigma Aldrich) was recrystallized in ethanol, then dried 3 days at 60°C under vacuum. Column chromatography was performed on silica gel (Merck Geduran Si 60, particle size 0.040-0.063 mm).

NMR spectra were acquired on a Bruker 400 (^1H at 400 MHz, ^{13}C at 100 MHz) magnetic resonance spectrometer, equipped with a temperature control module (range 223K-353K). ^1H chemical shifts are reported relative to the residual solvent peak (toluene = 7.09 ppm; chloroform = 7.24 ppm) as follows: chemical shift (δ), multiplicity (s = singlet, bs = broad singlet, d = doublet, t = triplet, q = quartet, p = pentet, m = multiplet), coupling constant(s) in Hz, integration. ^{13}C chemical shifts are reported relative to the deuterated solvent ^{13}C signals (Toluene = 137.86 ppm; chloroform = 77.23 ppm). “Core” mention is used for ^{13}C attributions involving carbon atoms of the heptazine core.

UV-Vis measurements were performed in acetonitrile in a Hellma 110-QS quartz cell (light path 10 mm) on a Perkin-Elmer Lambda 950 spectrometer equipped with an integration sphere for solid state measurement. Fluorescence measurements were performed in acetonitrile in a Hellma 117.100F-QS quartz cell (light path 10x10 mm) on a Perkin-Elmer LS55 fluorescence spectrometer. Fluorescence quantum yields were measured on a Horiba Fluorolog spectrometer equipped with an integrating sphere. Sample where hold in a suprasil silica tube. Infrared spectra were recorded on a Thermo Scientific Nicolet iS50 Fourier transform spectrometer (FTIR) and are reported in wavenumbers (cm^{-1}). Samples were prepared in dry KBr pellets.

Cyclic voltammetry was performed in a glove box equipped with a biologic SP300 potentiostat (with an impedance spectroscopy, a low current and an analogic card option). Measurements were performed in a three electrodes configuration, working electrode: glassy C (3mm diameter), counter electrode: platinum plate, reference: Ag/AgCl homemade electrode, electrolyte: AcN/0.1M nBu_4PF_6. The study of **1a** in reduction is performing in DMSO/0.1M nBu_4PF_6. All potential was calibrated using ferrocene as standard ($E^0_{Fc+/Fc}$= 0.630V/NHE in AcN[2], $E^0_{Fc+/Fc}$= 0.628V/NHE in DMSO[3]). Before each voltamogram, working electrode was polished on a cloth impregnated with 0.05µm alumina then rinsed several time with AcN.

Elemental analyses were carried out at the Centre régional de mesures physiques de l'Ouest (CRMPO) in Rennes, France.

Computational methods

DFT (Density Functional Theory) calculations have been performed with the code ADF 2012 (Amsterdam Density Functional) developed by E. J. Baerends[4]. Triple-*zeta* basis set quality has been used throughout all calculations.

Full geometry optimizations have been obtained at the GGA level with the VBP exchange-correlation potential (VBP for VWN + BP: Vosko, Wilk & Nusair[5] + gradient corrective terms by Becke[6] for the exchange and Perdew[7] for the correlation) for all neutral species. Full (gga) geometry optimization (ADF high precision level set to 6) was possible for the monomer **1a** in the *three* redox states because of its C_3 symmetry, allowing for a detailed study of the impact of redox changes upon geometrical features. By contrast, orbital near-degeneracy (and therefore convergence problem) was encountered for the *oxidized* states of both **2** and **3** at the gga level. All redox potentials and subsequent molecular orbitals' plots (see below) have been based on the neutral geometries, for which we succeeded in getting electronic convergence at the B3LYP[8] level for the three redox states (though at the price of very time-consuming calculations for the oxidized states of both **2** and **3**).

Solvation energies ΔG_{solv}(ox) and ΔG_{solv}(red) for the redox couple (ox/red) which are necessary for the calculation of redox potentials rely on the COSMO module (COnductor-like Screening MOdel)[7, 9] modeling the acetonitrile solvent as a dielectric continuum of constant $\varepsilon = 37$, with an average solvent radius of R = 2.76 Å ("name=acetonitrile" in the ADF input). Bonding energies E_{ox} and E_{red} for each redox couple (ox/red) are computed with the hybrid exchange-correlation B3LYP (run with the no-frozen core option) a potential mixing in (20%) of Hartree-Fock exchange within the DFT exchange-correlation potential. The difference IP(red) = $E_{ox} - E_{red}$ is the ionization potential. The final estimation of the redox potential is E^O(ox/red) = IP(red) + ΔG_{solv}(ox) - ΔG_{solv}(red) -4.28, where 4.28 V stands for the absolute standard hydrogen electrode potential serving as a reference[10] (notice that the variations in values obtained by various approaches, in the range 4.05-4.44 V, suggest an uncertainty in the absolute value of about ± 0.2 V: see note 105 of Ref.[11]).

To help identify the specific features of the UV-visible absorption spectra recorded for **1a**, **2** and **3**, we performed TD-DFT calculations relying on the SAOP (Statistical Average Of Potential) exchange-potential[12], specifically designed to exhibit the proper (−1/*r*) asymptotic behavior outside the molecular model. The simulated spectra have been generated by taking into account all first 30 excitations $(E_i)_{i=1-30}$ yielded by the implemented TD-DFT procedure (Davidson's algorithm)[13]. Notice that no *a priori* selection of the transitions has been performed. The analytical expression used for the simulated spectra is as follows: $\Sigma_i\ f_i \times [10^6/\sigma \cdot \mathrm{sqrt}(\pi)] \cdot \exp - [(8066 \times 1240/\sigma^2) \cdot (1/E - 1/E_i)]$, where f_i is the oscillator strength for transition *i*, σ defines a common broadness factor for the peaks of a given spectrum (set to 1000 in this study), *E* and E_i are expressed in wavelength units (nm), and 8066 and 1240 are appropriate conversion factors (1240/nm = eV and eV × 8066 = cm^{-1}).

We moreover computed IR spectra with the analytical IR module of ADF (all calculations at ADF precision level 6). For that, we first geometry-optimized all three neutral oligomers with the Stoll treatment of correlation[14], as already done before[15] (the choice of the analytical procedure restricts that of the exchange-correlation potentials compatible with that module).

All molecular orbital pictures have been produced from ADF TAPE21 files via a home-made Python (+ Mayavi) code written by N. Onofrio (now at Purdue University, IN, USA).

Synthesis

Preparation of 1a

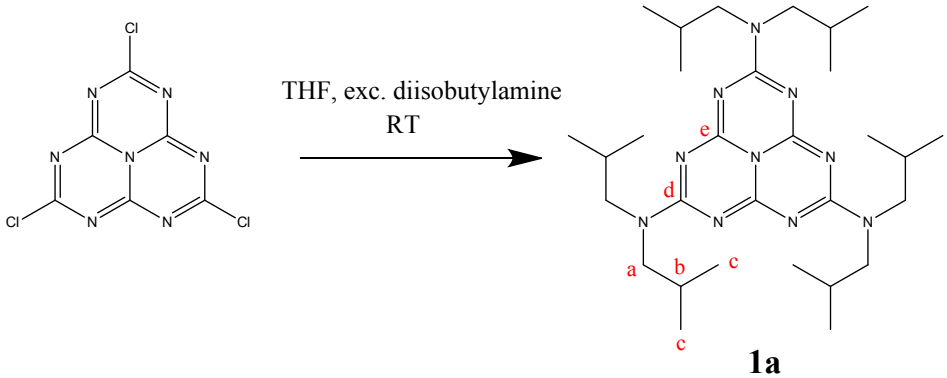

1a

Cyamerulic chloride (504 mg, 1.823 mmol, 1 eq) was solubilized in anhydrous THF (100 mL) under Ar atmosphere and magnetic stirring. Large excess of diisobutylamine (3 mL, 17.16 mmol, 9.4 eq) was added to the mixture. Solution was stirred at ambient temperature overnight. Solvent was evaporated, and the reaction mixture was dissolved in $CHCl_3$ (20mL), washed with water (3x20mL). Solvent was dried and evaporated prior purification of the crude product by recrystallization in acetonitrile, to afford the desired product **1a** as small transparent needles (960.8mg, 95%).
Single crystals suitable for X-ray diffraction were obtained by slow diffusion of hexane in a solution of **1** (20mg / 1mL) in dichloromethane.[16]

^{1}H NMR (Toluene) δ= a 3.41-3.39 (d, 7.6Hz, 2H), b 2.15-2.01 (m, 6.9Hz, 1H), c 0.78-0.76 (d, 6.7Hz, 6H) ppm

^{13}C NMR (Toluene) δ= d 165.0, e 156.0, a 55.1, b 27.7, c 20.5 ppm

IR (KBr pellet): 807, 1033, 1102, 1129, 1262, 1284, 1342, 1361, 1385, 1428, 1490, 1525, 1636, 2870, 2959 cm^{-1}

UV/vis (acetonitrile): 315 (ε=2000 $L.mol^{-1}.cm^{-1}$), 273 (89400), 248 (49100) nm

MS [M+H$^+$]: 555.6 m/z

Elemental analysis: $C_{30}H_{54}N_{10}$ calcd. (%) C 64.94, H 9.81, N 25.25; found (%) C 63.95, H 9.56, N 24.17

Preparation of 1b

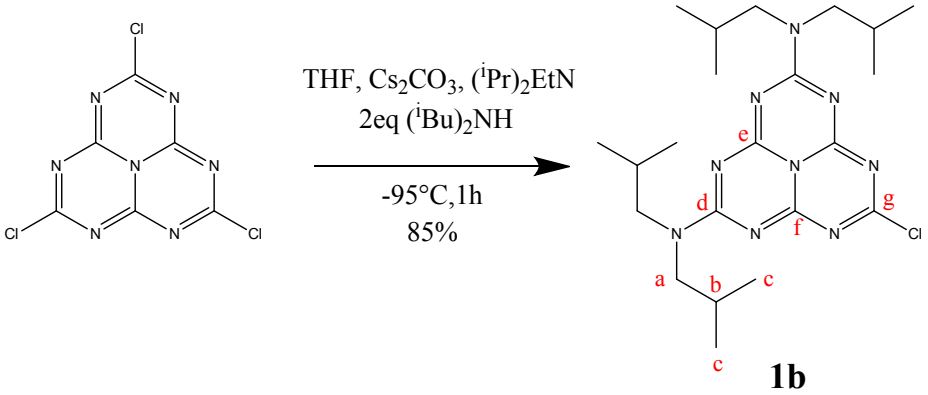

1b

Cyamerulic chloride (129 mg, 0.467 mmol, 1 eq) was solubilized in anhydrous THF (200 mL) under Ar atmosphere and magnetic stirring. Cs_2CO_3 (831 mg, 2.55 mmol, 5.5 eq) was added to the solution. Solution was cooled down in a liquid N_2/toluene bath to -95°C. Diisopropylethylamine (154 µL, d=0.782, 0.932 mmol, 2 eq), then diisobutylamine (163 µL, d=0.74, 0.933 mmol, 2 eq) were added to the mixture. Solution was stirred at low temperature for 1h, then left to reach room temperature and then at ambient temperature overnight. Solvent was evaporated, and the reaction mixture was dissolved in $CHCl_3$ (20mL), washed with water (3x20mL). Solvent was dried and evaporated prior purification of the crude product using column chromatography (silica, hexane/EtOAc, 85:15) to afford the desired product **1b** as a white solid (169.2mg, 85%).

^{1}H NMR ($CDCl_3$) δ= a 3.48-3.45 (dd, 2H), b 2.17-2.00 (m, 1H), c 0.90-0.85 (dd, 6H) ppm

^{13}C NMR ($CDCl_3$) δ= g 171.6, d 163.2, e-f (155.2, 154.2), a 55.4-55.3 (d), b 27.3-27.1 (d), c 20.2-20.1 (d) ppm

IR (KBr pellet): 808, 944, 969, 1181, 1227, 1279, 1297, 1341, 1360, 1387, 1432, 1474, 1531, 1552, 1624, 1652, 1763, 2870, 2960 cm^{-1}

UV/vis (acetonitrile): 365 (ε=1700 $L.mol^{-1}.cm^{-1}$), 347 (2500), 268 (46800), 254 (51600), 204 (23100) nm

MS [M+H$^+$]: 462.5 m/z

Elemental analysis: $C_{22}H_{36}N_9Cl$ calcd. (%) C 57.19, H 7.85, N 27.28; found (%) C 56.81, H 7.77, N 26.52

Preparation of 1c

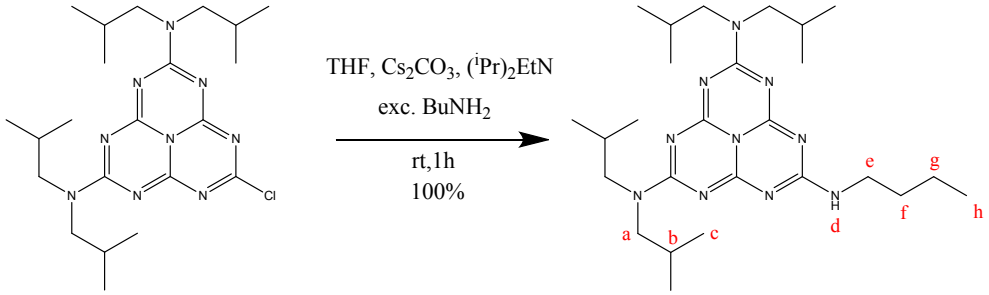

1b **1c**

1b (105.1 mg, 0.228 mmol, 1 eq) was solubilized in anhydrous toluene (30 mL) under Ar atmosphere and magnetic stirring. Cs_2CO_3 (446 mg, 1.37 mmol, 6 eq) was added to the solution. Large excess of n-butylamine (800 µL, 35 eq) was added to the mixture. Solution was stirred at ambient temperature overnight. Solvent was evaporated, and the reaction mixture was dissolved in $CHCl_3$ (20mL), washed with water (3x20mL). The solvent was dried with Na_2SO_4, filtered and evaporated. Desired product **1c** was obtained without further purification as a white solid in a quantitative yield (113.6 mg).

^{1}H NMR ($CDCl_3$) δ= d 5.38 (t, 1H), a-e 3.49-3.42 (m, 10H), b 2.14-2.04 (m, 4H), f 1.54-1.47 (m, 2H), g 1.40-1.30 (m, 2H), c-h 0.92-0.85 (m, 27H) ppm

^{13}C NMR ($CDCl_3$) δ= core (164.4, 163.8, 163.6, 155.7, 155.0, 154.6), a 54.9, e 41.1, f 31.9, b 27.2, c-g 20.3- 20.2, h 14.0 ppm

IR (KBr pellet): 807, 1032, 1103, 1140, 1191, 1269, 1341, 1354, 1387, 1400, 1427, 1479, 1514, 1568, 1609, 1642, 2870, 2930, 2959, 3096, 3230 cm^{-1}

UV/vis (acetonitrile): 320 (ε=2000 $L.mol^{-1}.cm^{-1}$), 269 (84900), 244 (50000) nm

MS [M+H$^+$]: 499.4 m/z

Elemental analysis: $C_{26}H_{46}N_{10}$ calcd. (%) C 62.62, H 9.30, N 28.09; found (%) C 62.17, H 9.16, N 26.98

Preparation of 1d

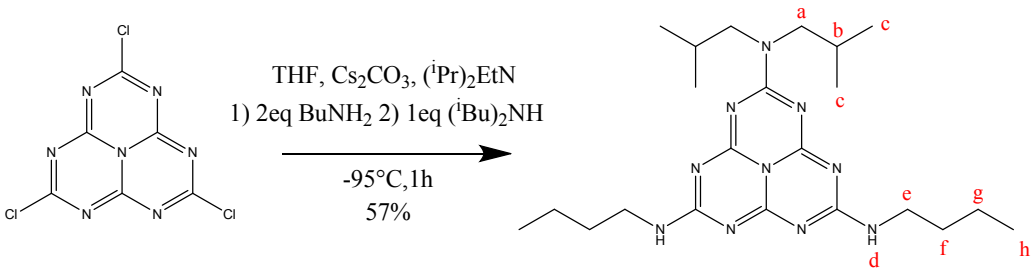

1d

Cyamerulic chloride (109 mg, 0.394 mmol, 1 eq) was solubilized in anhydrous THF (100 mL), under Ar atmosphere and magnetic stirring. Cs_2CO_3 (757mg, 2.32 mmol, 5.9 eq) was added to the solution. Solution was cooled down in a liquid N_2/toluene bath. Diisopropylethylamine (130 µL, d=0.782, 0.787 mmol, 2 eq), then n-butylamine (78 µL, d=0.74, 0.789 mmol, 2 eq) were added to the mixture. Solution was stirred at low temperature for 1h, and then at ambient temperature overnight. Diisobutylamine (130 µL, d=0.782, 0.787 mmol, 2 eq) is then added, and left for reaction for 2h. Solvent was evaporated, and the reaction mixture was dissolved in $CHCl_3$ (20mL), washed with water (3x20mL). Solvent was dried and evaporated prior purification of the crude product using column chromatography (silica, hexane/EtOAc, 1:9) to afford the desired product **1d** as a white solid (98.5mg, 57%).

^{1}H NMR ($CDCl_3$) δ= d 5.71-5.59 (m, 2H), a-e 3.55-3.44 (m, 8H), b 2.17-2.08 (m, 2H), f 1.59-1.51 (m, 4H), g 1.42-1.34 (m, 4H), c-h 0.97-0.90 (m, 18H) ppm, (mixture of conformer)

^{13}C NMR ($CDCl_3$) δ= core (164.1, 163.9, 163.3, 163.1, 156.5, 155.5, 154.6-154.5, 155.3), a 54.8-54.7, e 41.1-41.0, f 31.6, b 26.9, c-g 20.0-19.9, h 13.8 ppm, (mixture of conformers)

IR (KBr pellet): 807, 1268, 1307, 1360, 1387, 1403, 1429, 1474, 1515, 1558, 1644, 2871, 2958, 3096, 3242 cm^{-1}

UV/vis (acetonitrile): 317 (ε=1000 $L.mol^{-1}.cm^{-1}$), 264 (72900), 239 (44900) nm

MS [M+H$^+$]: 443.3 m/z

Elemental analysis: $C_{22}H_{38}N_{10}$ calcd. (%) C 59.70, H 8.65, N 31.65; found (%) C 59.36, H 8.59, N 30.66

Preparation of 2

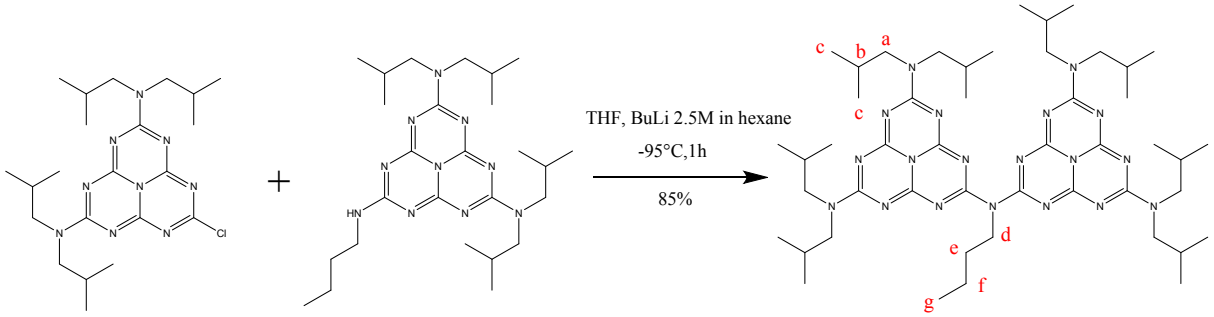

1b **1c** **2**

1c (135.9 mg, 0.273 mmol, 1 eq) was solubilized in anhydrous THF (20 mL) under Ar atmosphere and magnetic stirring. Solution was cooled down in a liquid N_2/toluene bath. BuLi (2.5M in hexane, 145µL, 0.363 mmol, 1.3 eq) was slowly added to the mixture. **1b** (130.3 mg, 0.282 mmol, 1 eq) was solubilized in anhydrous THF (1.5 mL) under Ar atmosphere and then added to reaction mixture. Solution was stirred at low temperature for 1h, and then left at room temperature overnight; the solvent was evaporated, and the reaction mixture was dissolved in $CHCl_3$ (20mL), washed with water (3x20mL). Solvent was dried and evaporated prior purification of the crude product using column chromatography (silica, CH_2Cl_2/EtOH, 98:2) to afford the desired product **2** as a white solid (215.3 mg, 85%).

Single crystals suitable for X-ray diffraction were obtained by the slow evaporation at 60°C of a solution of **2** in nitrobenzene.

^{1}H NMR δ= d 4.34-4.30 (t, 2H), a 3.50-3.47 (dd, 16H), b 2.32-2.18 (m, 8H), e 1.97-1.90 (m, 2H), f 1.40-1.31 (m, 2H), c-g 0.97-0.90 (dd+t, 51H) ppm

^{13}C NMR δ= core (167.8, 163.9, 156.4, 155.1), a 55.2-55.1, d 47.6, e 31.4, b 27.2-27.1, c-f 20.0-19.9, g 13.8 ppm

IR (KBr pellet): 810, 1101, 1132, 1188, 1223, 1258, 1280, 1341, 1361, 1383, 1430, 1466, 1518, 1582, 1644, 2871, 2959 cm^{-1}

UV/vis (acetonitrile): 368 (ε=2400 $L.mol^{-1}.cm^{-1}$), 353 (4000), 304 (63100), 276 (90200), 258 (87000) nm

MS [M+H$^+$]: 924.7 m/z

Elemental analysis: $C_{48}H_{81}N_{19}$ calcd. (%) C 62.37, H 8.83, N 28.79; found (%) C 61.90, H 8.73, N 26.64

Preparation of 3

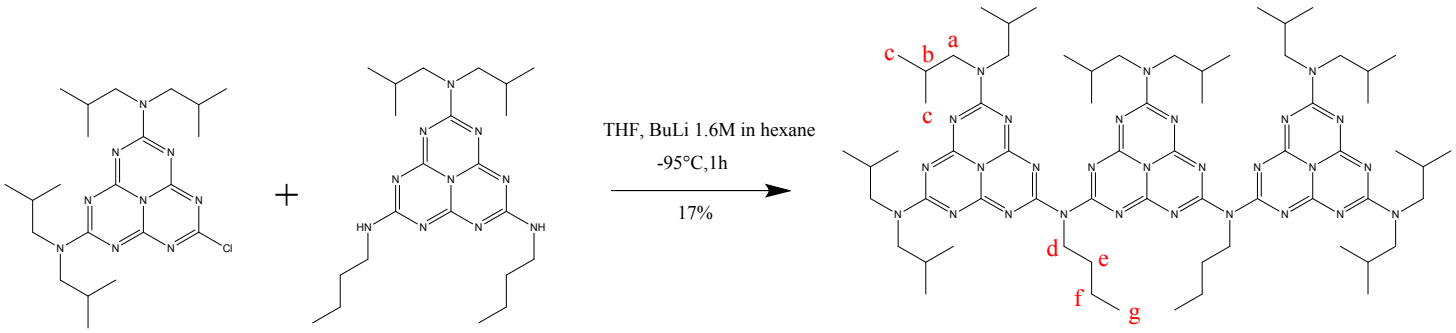

1b **1c** **3**

1d (52.9 mg, 0.119 mmol, 1 eq) was solubilized in anhydrous THF (20 mL) under Ar atmosphere and magnetic stirring. Solution was cooled down in a liquid N_2/toluene bath. BuLi (1.6M in hexane, 180µL, 0.288 mmol, 2.4 eq) was slowly added to the mixture. **1b** (110.0 mg, 0.238 mmol, 2 eq) was solubilized in anhydrous THF (1.5 mL) under Ar atmosphere and then added to reaction mixture. Solution was stirred at low temperature for 1h, and then left for reaction at room temperature overnight; the solvent was evaporated, and the reaction mixture was dissolved in $CHCl_3$ (20mL), washed with water (3x20mL). Solvent was dried and evaporated prior purification of the crude product using column chromatography (silica, hexane/EtOAc, 90:10 to 70:30), and washing with pentane, to afford the desired product **3** as a white solid (26.3 mg, 17%).

^{1}H NMR (Toluene) δ= d 4.23-4.19 (t, 4H), a 3.39-3.35 (t, 20H), b 2.23-2.0- (m, 10H), e 1.91-1.83 (m, 4H), f 1.33-1.24 (m, 4H), c-g 0.89-0.78 (m, 66H)

^{13}C NMR (Toluene) δ= core (168.7, 168.0, 164.3, 158.3, 157.1, 156.7, 155.7), a 56.3-55.9-55.8, d 48.3, e 32.0, b 27.9-27.7, c-f 20.6, g 14.5 ppm

IR (KBr pellet): 809, 1101, 1189, 1221, 1263, 1283, 1341, 1361, 1385, 1429, 1467, 1518, 1643, 2871, 2959 cm^{-1}

UV/vis (acetonitrile): 370 (ε=4900 $L.mol^{-1}.cm^{-1}$), 355 (6800), 313 (99400), 272 (111300), 256 (113300) nm

MS [M+H$^+$]: 1293.8 m/z

Elemental analysis: $C_{66}H_{108}N_{28}$ calcd. (%) C 61.27, H 8.41, N 30.31; found (%) C 60.77, H 8.32, N 28.78

IR spectra

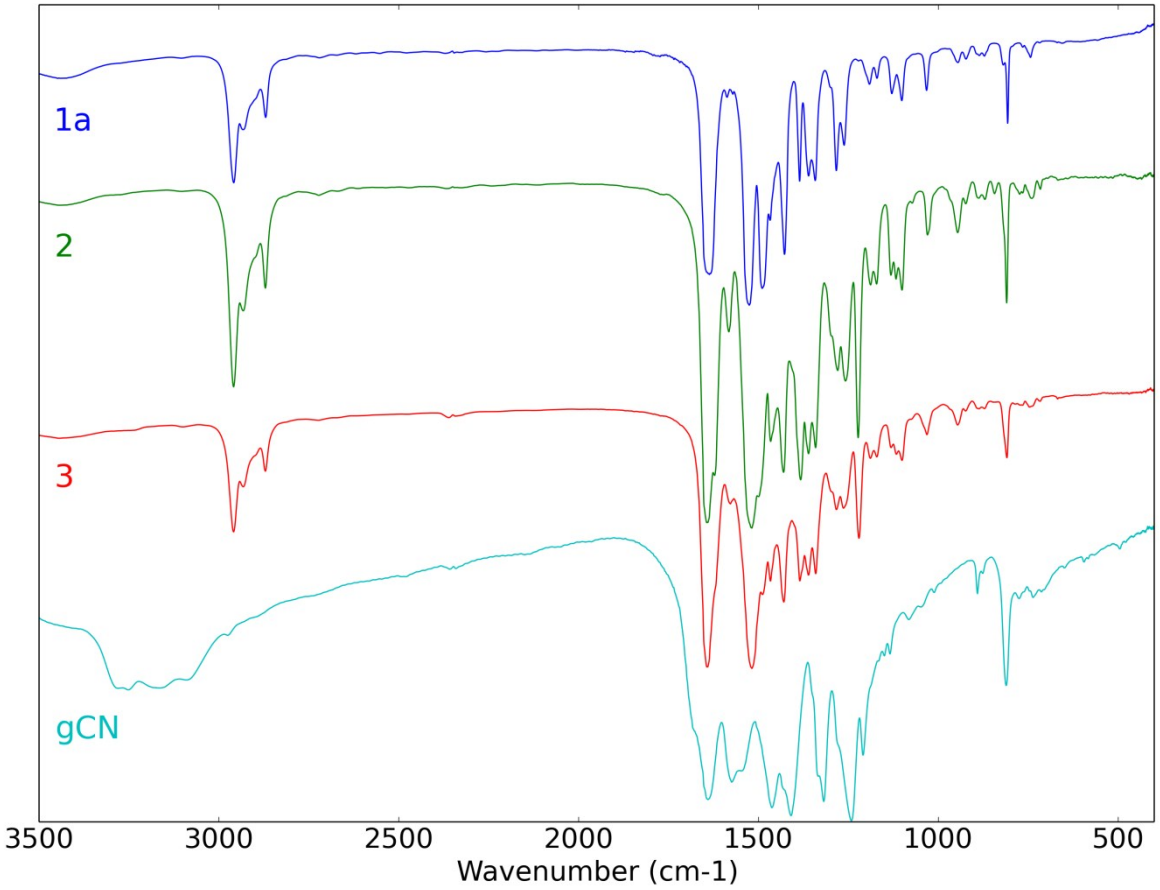

Figure S1 : IR spectra (KBr pellet) of oligomers, with gCN for comparison.

Figure S2 :
IR spectra (KBr pellet)
of **1a**.

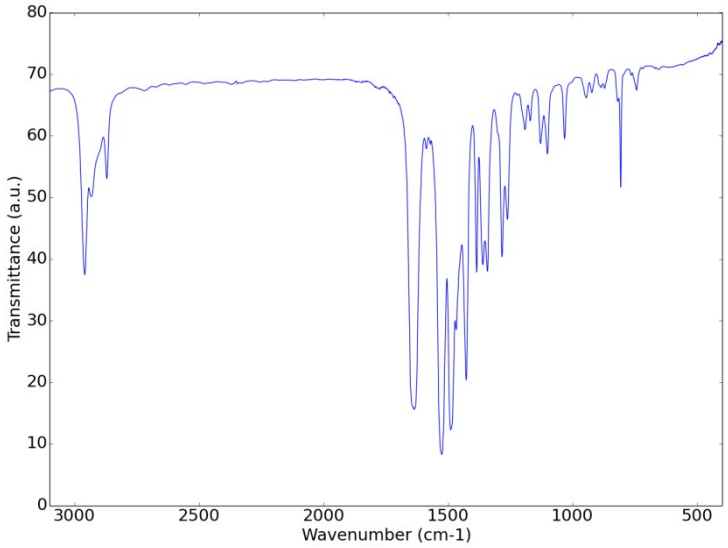

Figure S3 :
IR spectra (KBr pellet)
of **1b**.

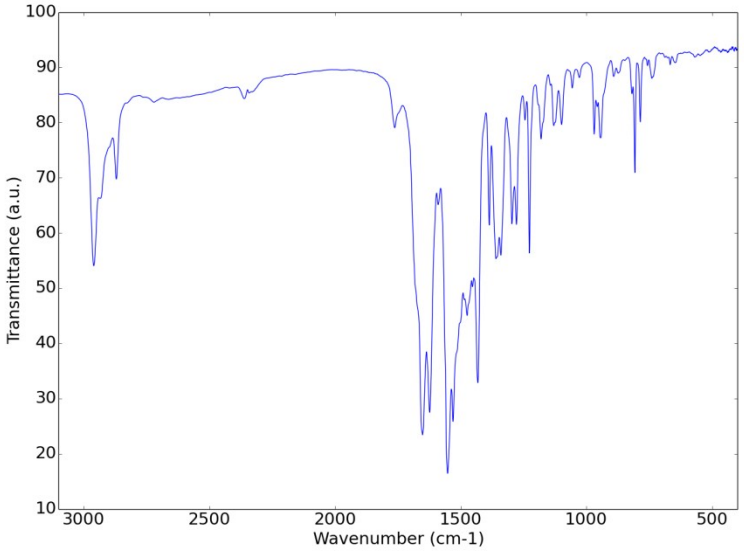

Figure S4 :
IR spectra (KBr pellet)
of **1c**.

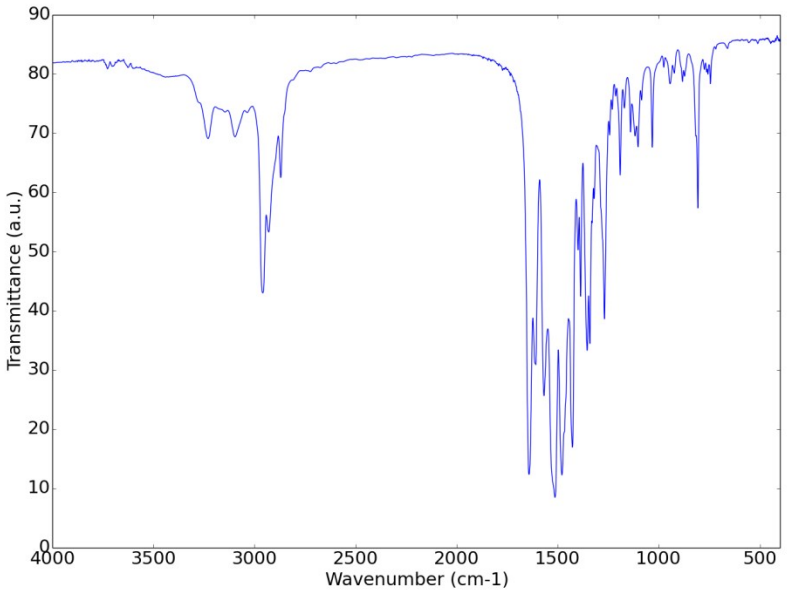

Figure S5 :
IR spectra (KBr pellet)
of **1d**.

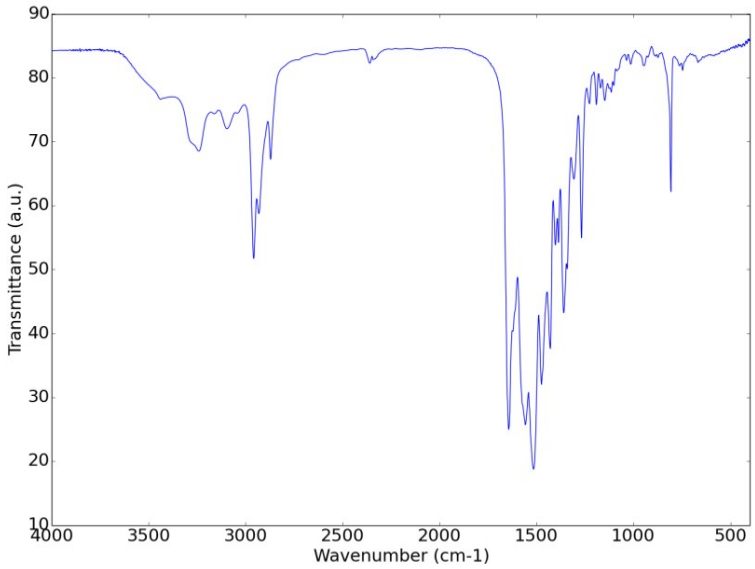

Figure S6 :
IR spectra (KBr pellet)
of **2**.

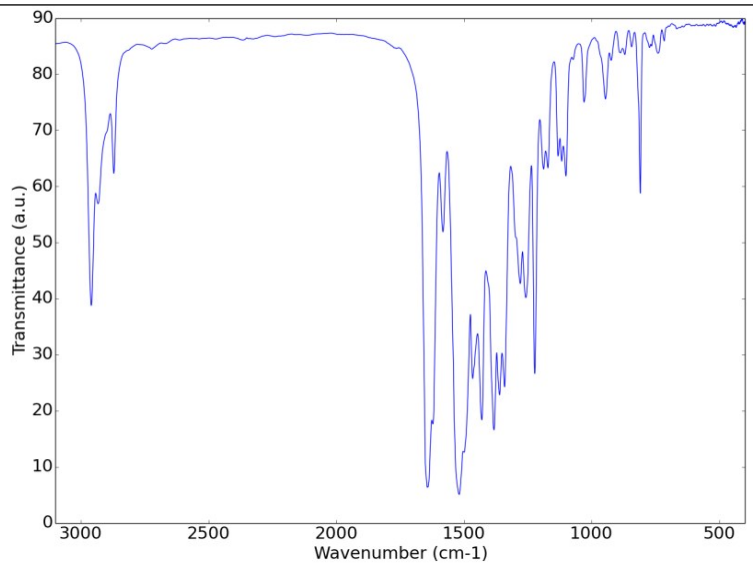

Figure S7 :
IR spectra (KBr pellet)
of **3**.

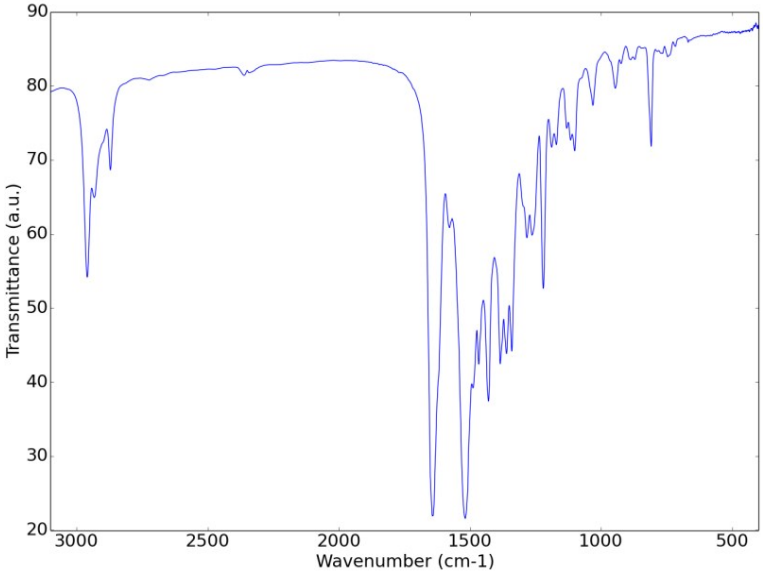

DFT calculations

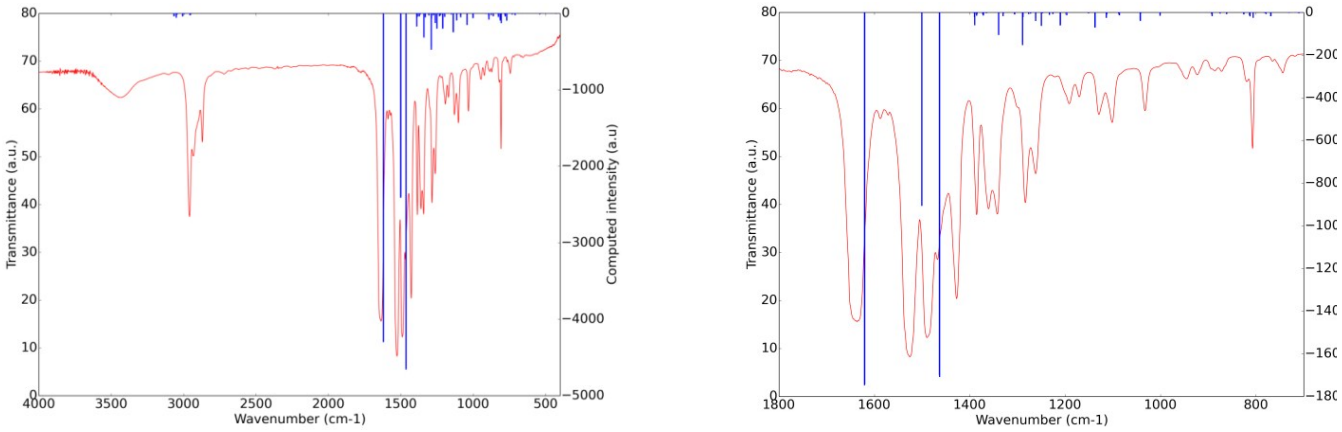

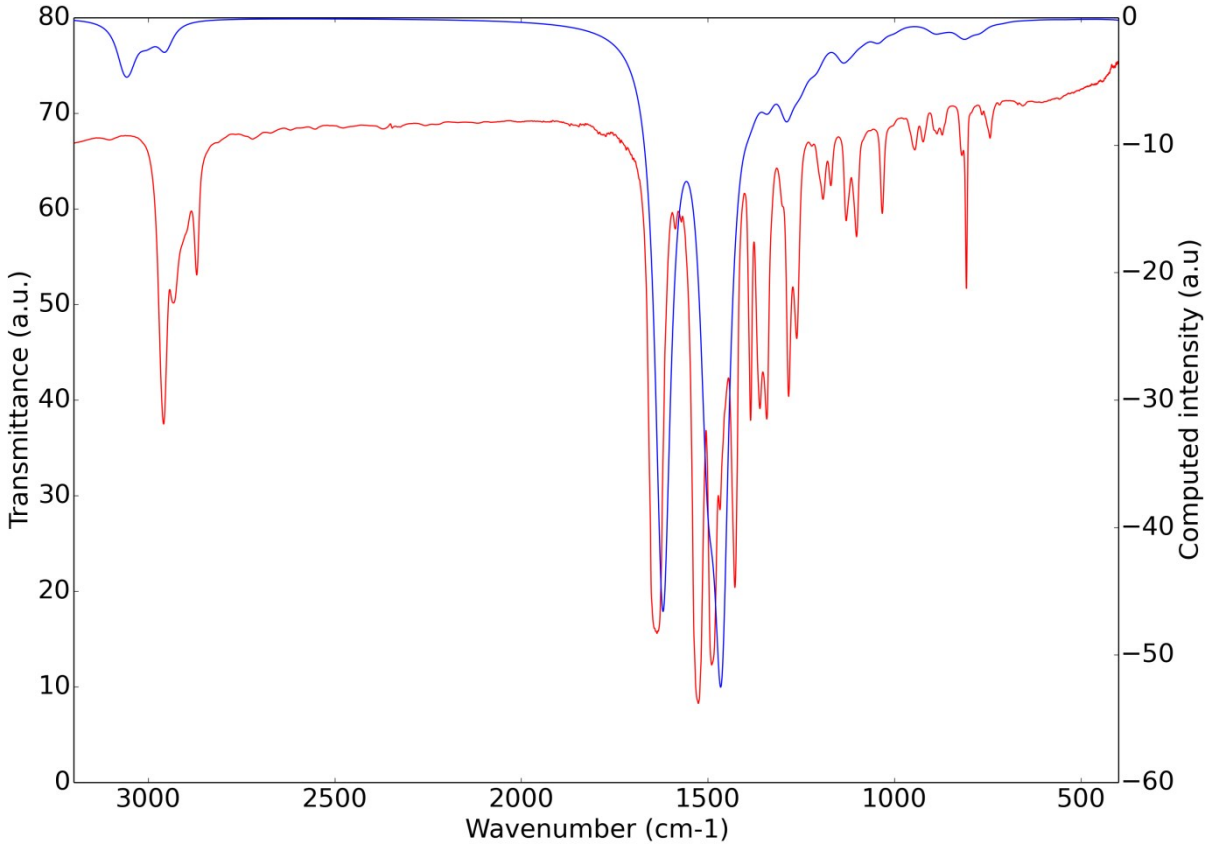

Figure S8 : top left: Simulated infrared spectrum for **1a** (blue bars: single transitions) versus experimental spectrum (red); top right: zoom in the 700-1800 cm-1 region; bottom: simulated Lorentzian envelope with FWHM=50cm^{-1} (blue) versus experimental spectrum (red).

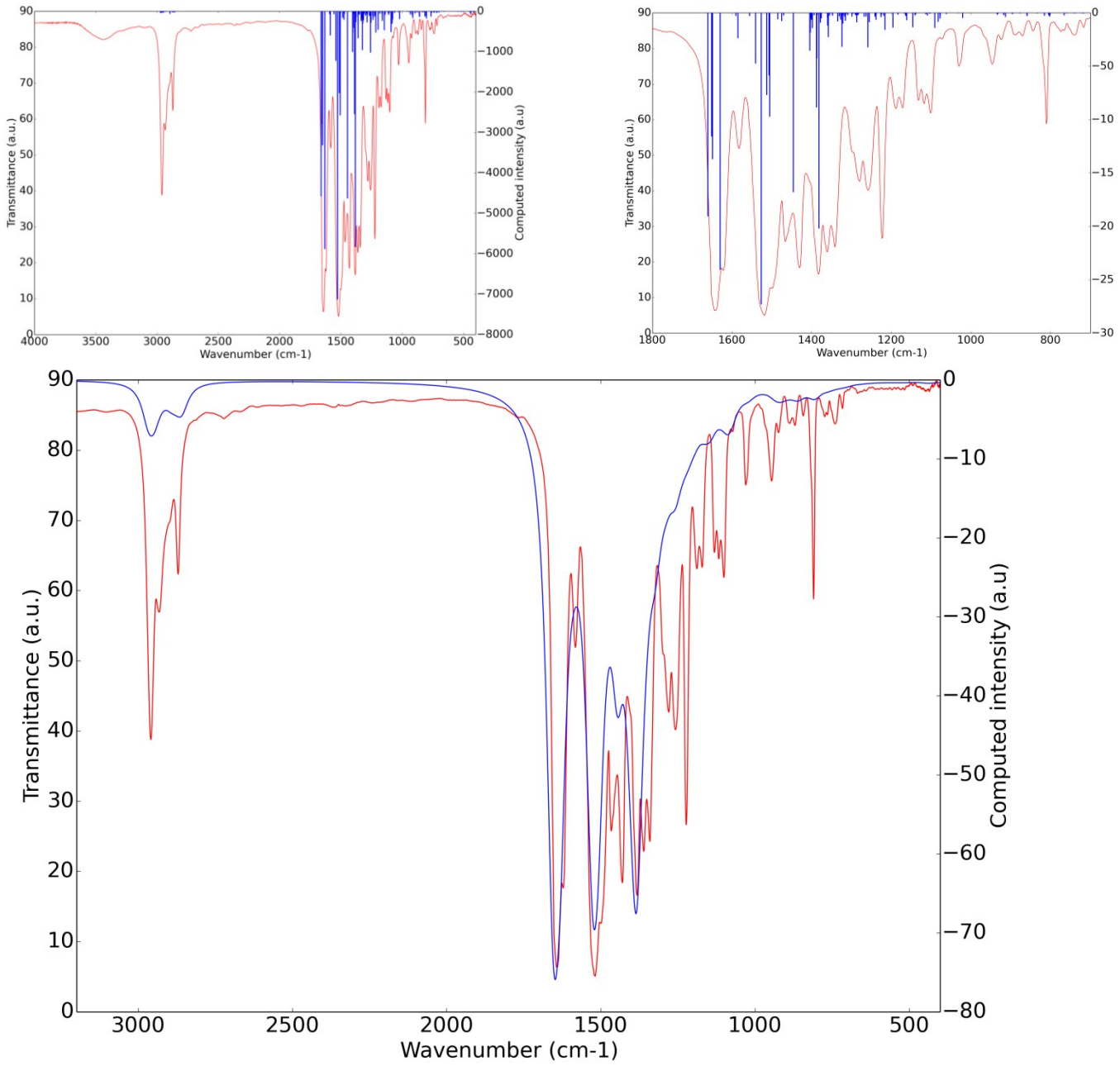

Figure S9 : top left: Simulated infrared spectrum for **2** (blue bars: single transitions) versus experimental spectrum (red); top right: zoom in the 700-1800 cm-1 region; bottom: simulated Lorentzian envelope with FWHM=50cm^{-1} (blue) versus experimental spectrum (red).

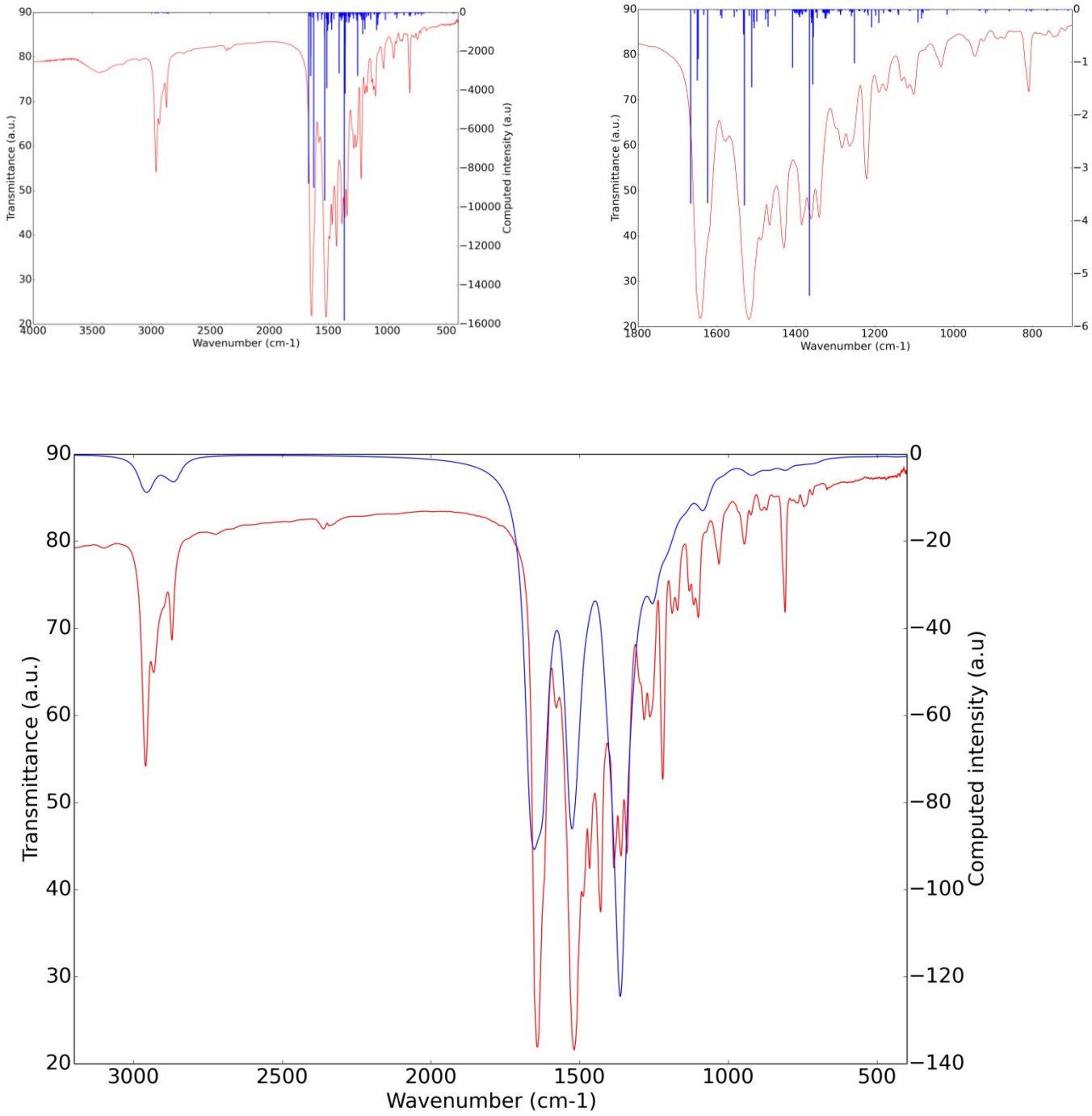

Figure S10 : top left: Simulated infrared spectrum for **3** (blue bars: single transitions) versus experimental spectrum (red); top right: zoom in the 700-1800 cm-1 region; bottom: simulated Lorentzian envelope with FWHM=50cm^{-1} (blue) versus experimental spectrum (red).

Although the general features of the experimental spectra are reproduced, these DFT calculations did not turn out to be very informative. We therefore did not attempt to further extract information out of these spectra (both measured & computed).

^{1}H NMR and ^{13}C NMR spectra

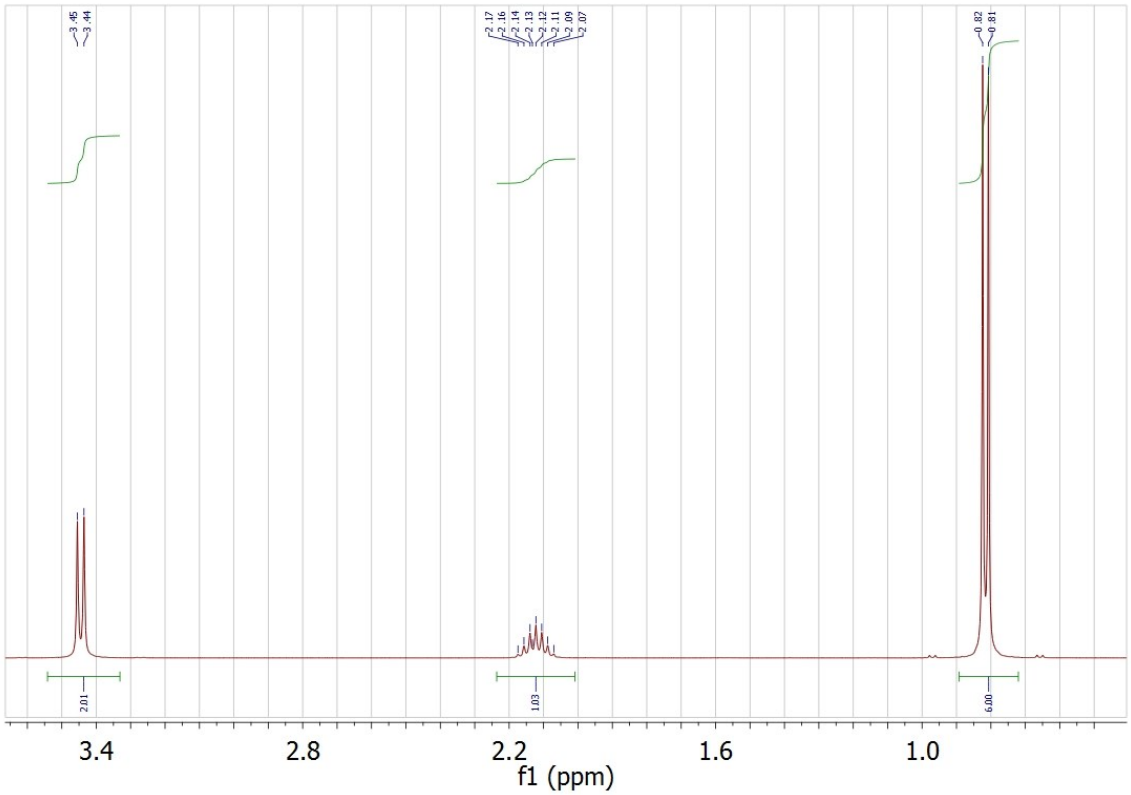

Figure S11 : ^{1}H NMR spectrum of compound **1a** (d_8-toluene, 400 MHz, 298 K).

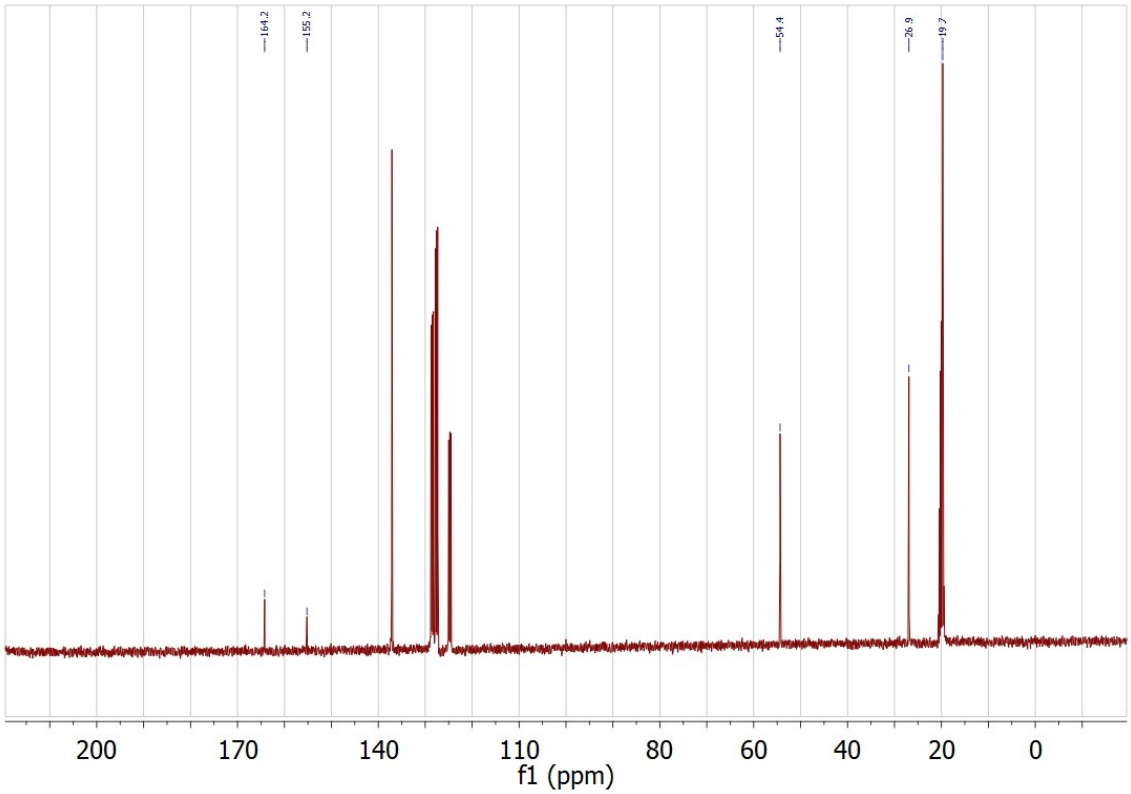

Figure S12 : ^{13}C NMR spectrum of compound **1a** (d_8-toluene, 100 MHz, 298 K).

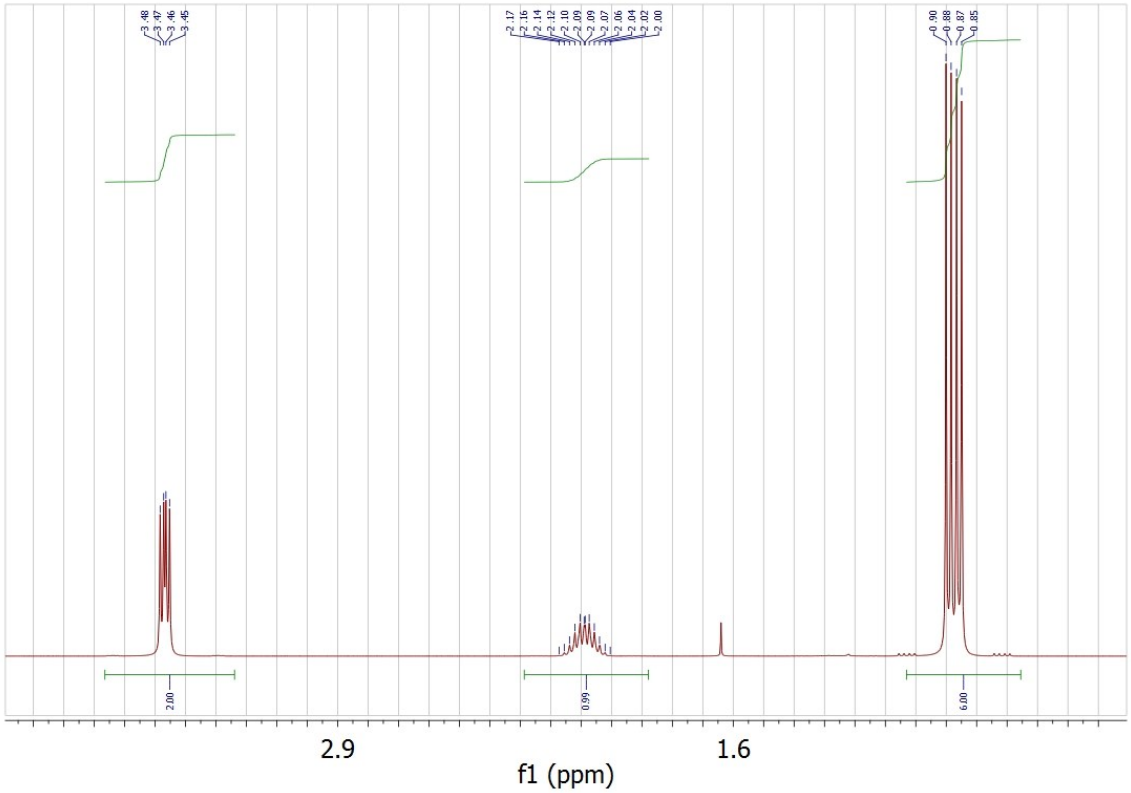

Figure S13 : ^{1}H NMR spectrum of compound **1b** ($CDCl_3$, 400 MHz, 298 K).

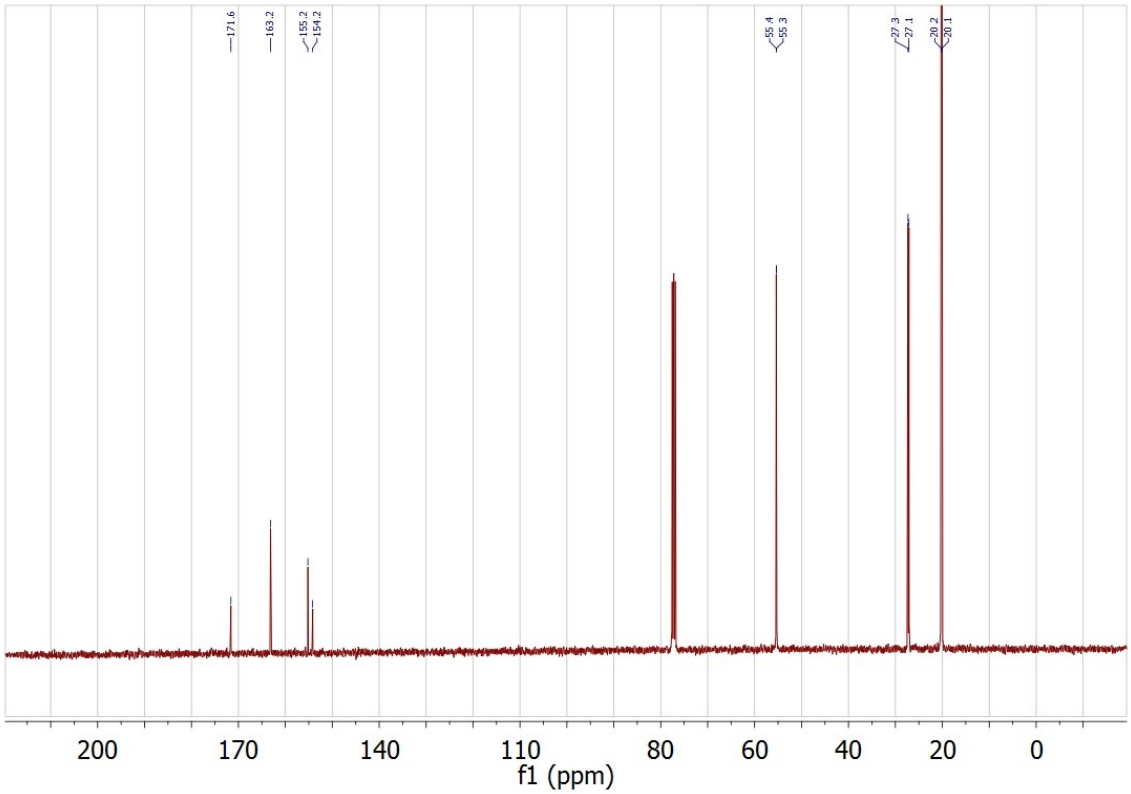

Figure S14 : ^{13}C NMR spectrum of compound **1b** ($CDCl_3$, 100 MHz, 298 K).

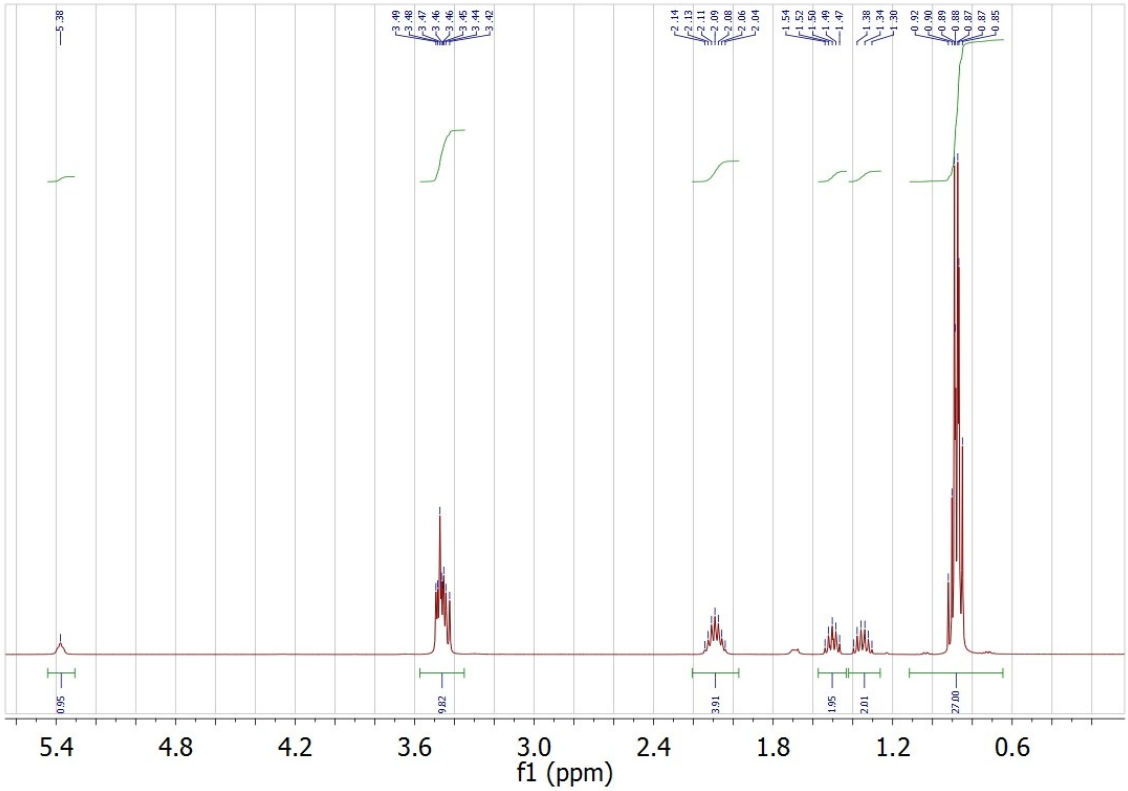

Figure S15 : ^{1}H NMR spectrum of compound **1c** ($CDCl_3$, 400 MHz, 298 K).

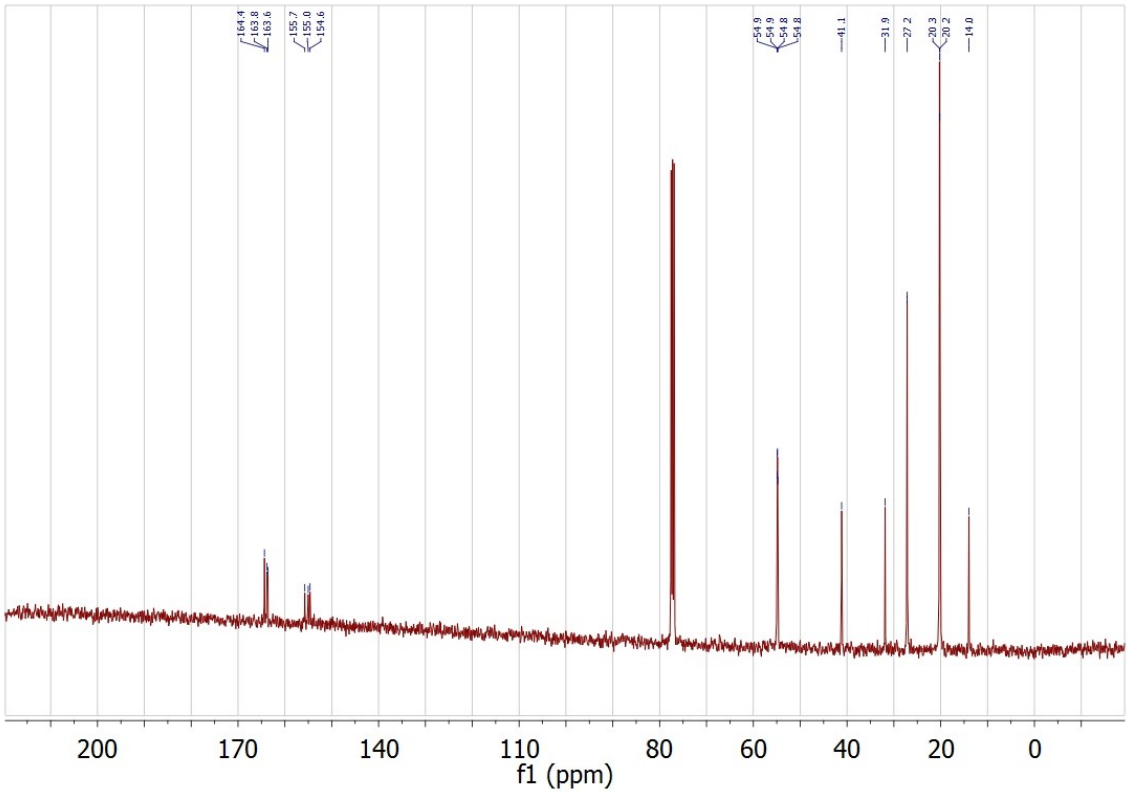

Figure S16 : ^{13}C NMR spectrum of compound **1c** ($CDCl_3$, 100 MHz, 298 K).

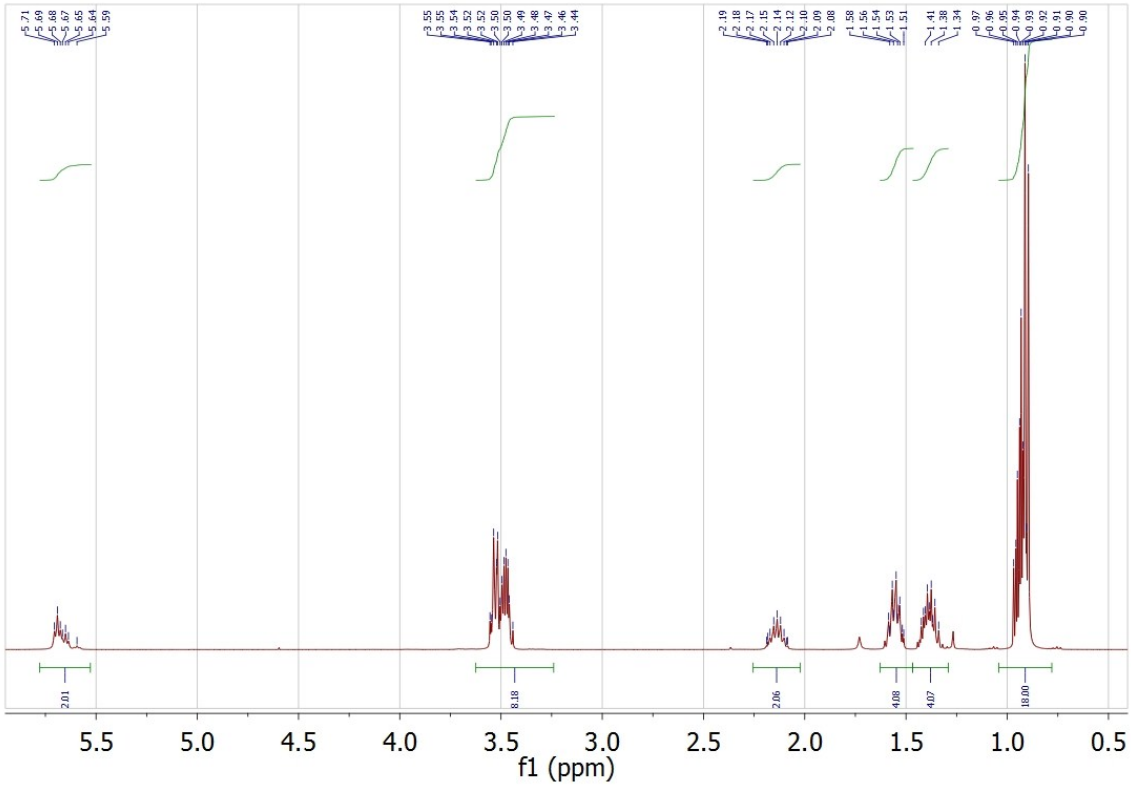

Figure S17 : ^{1}H NMR spectrum of compound **1d** ($CDCl_3$, 400 MHz, 298 K).

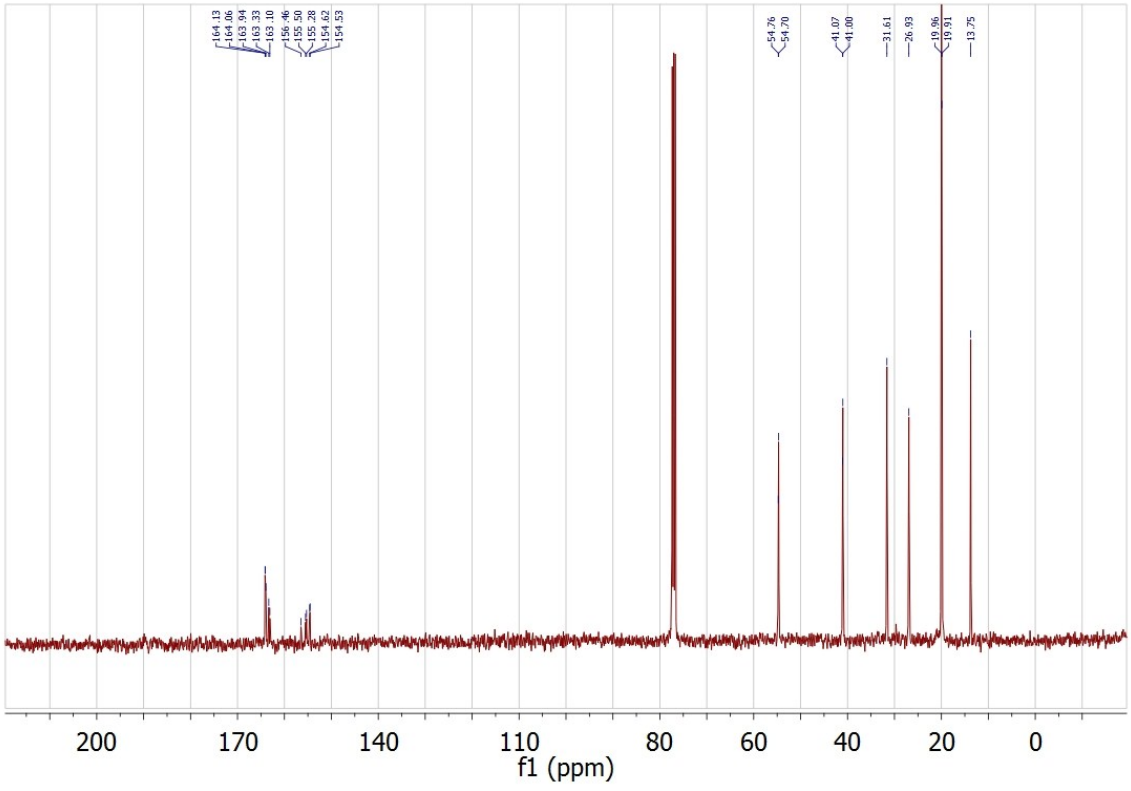

Figure S18 : ^{13}C NMR spectrum of compound **1d** ($CDCl_3$, 100 MHz, 298 K).

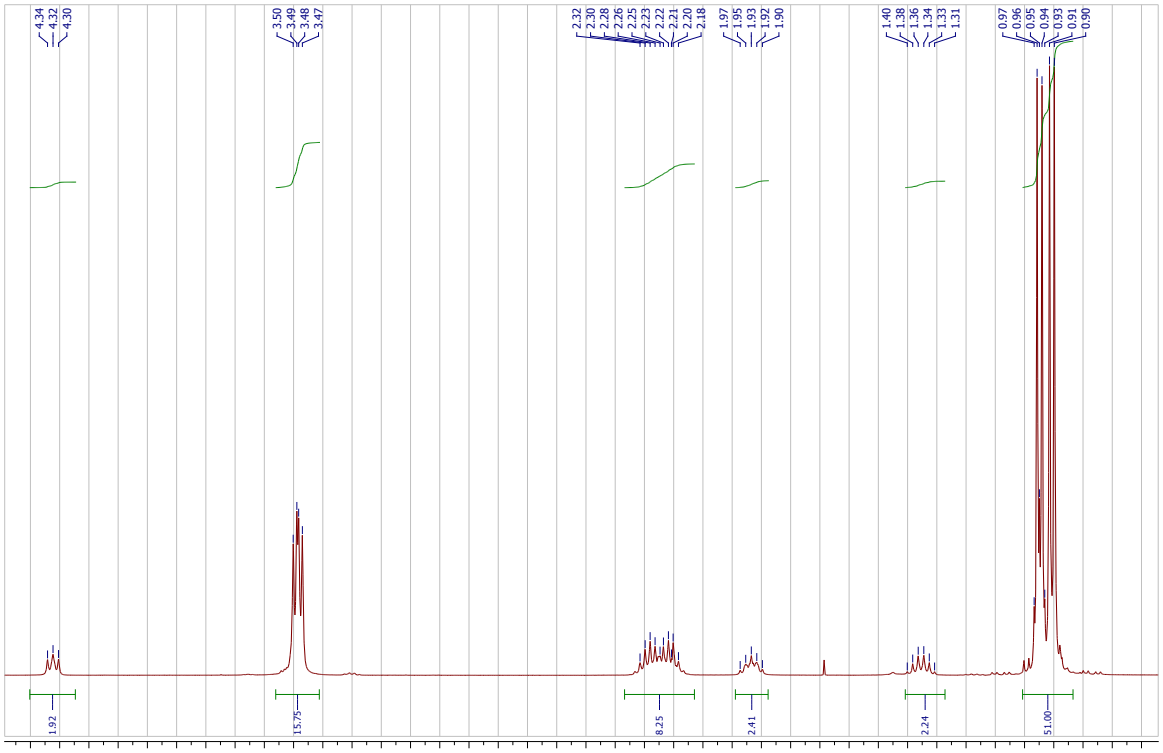

Figure S19 : ^{1}H NMR spectrum of compound **2** (d_8-toluene, 400 MHz, 298 K).

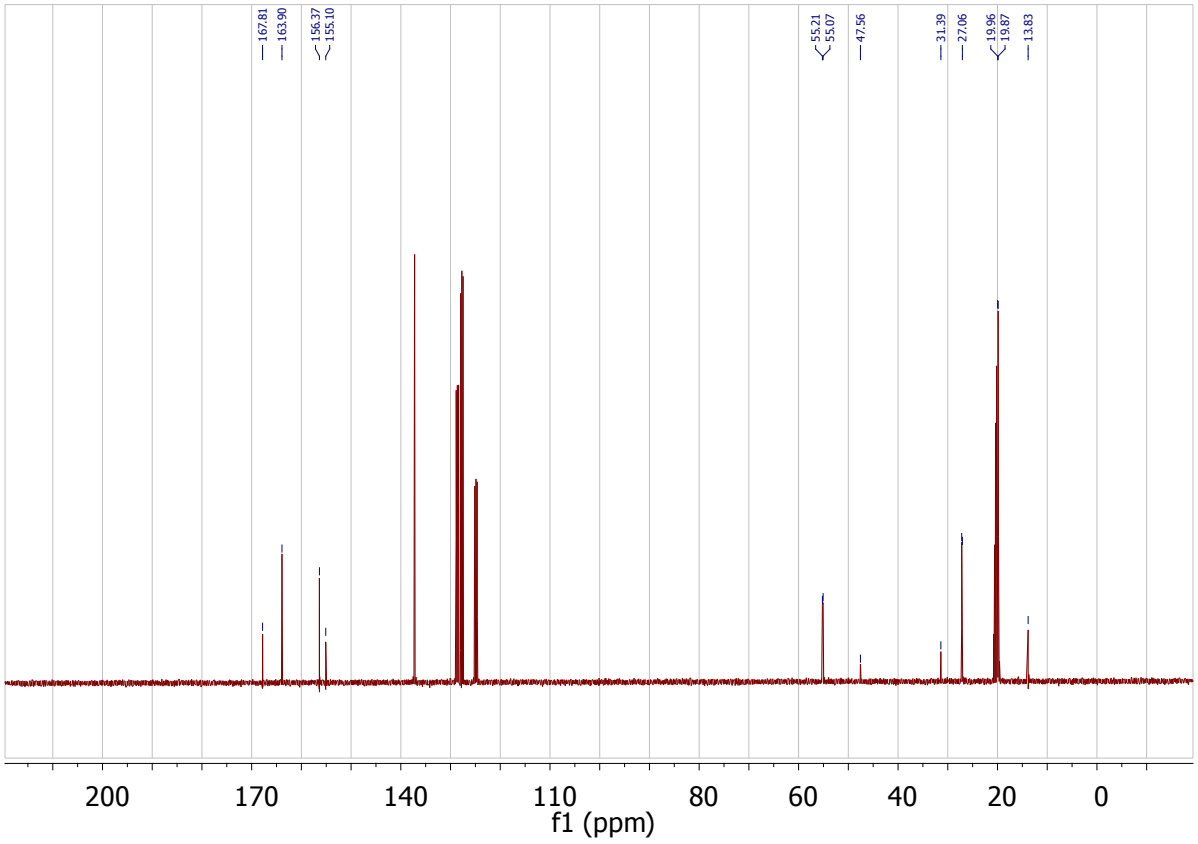

Figure S20 : ^{13}C NMR spectrum of compound **2** (d_8-toluene, 100 MHz, 298 K).

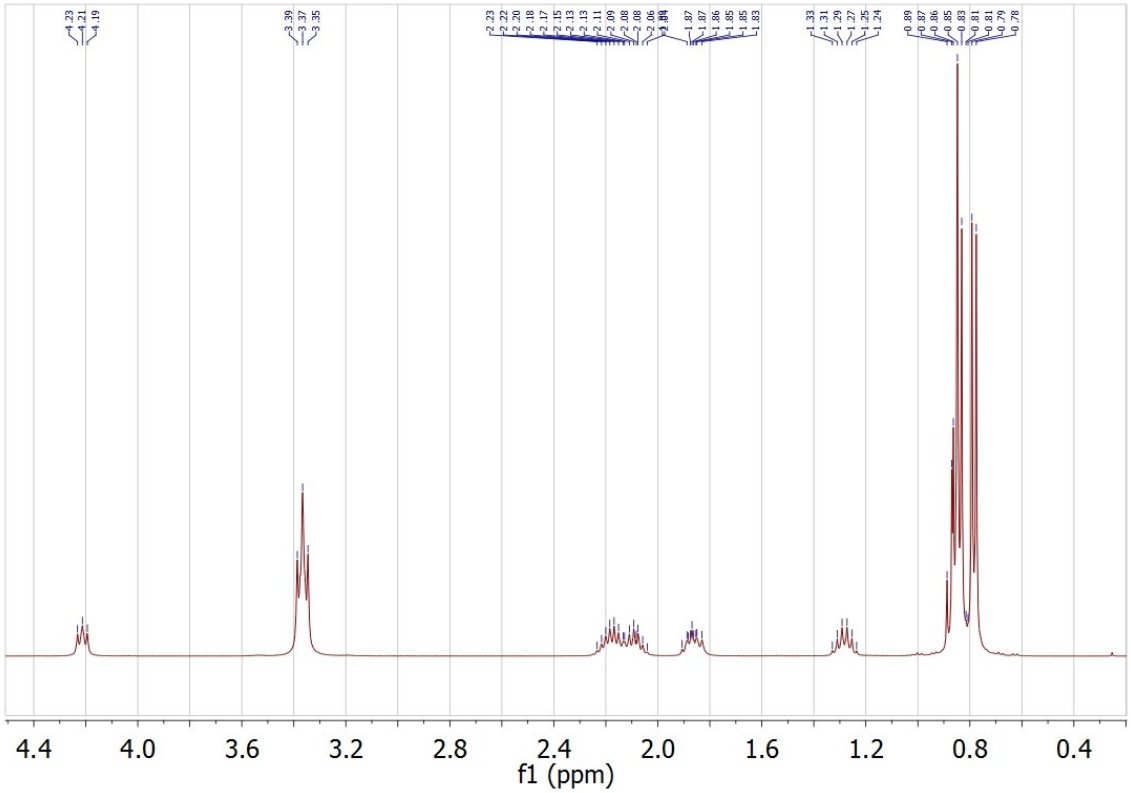

Figure S21 : ^{1}H NMR spectrum of compound **3** (d_8-toluene, 400 MHz, 298 K).

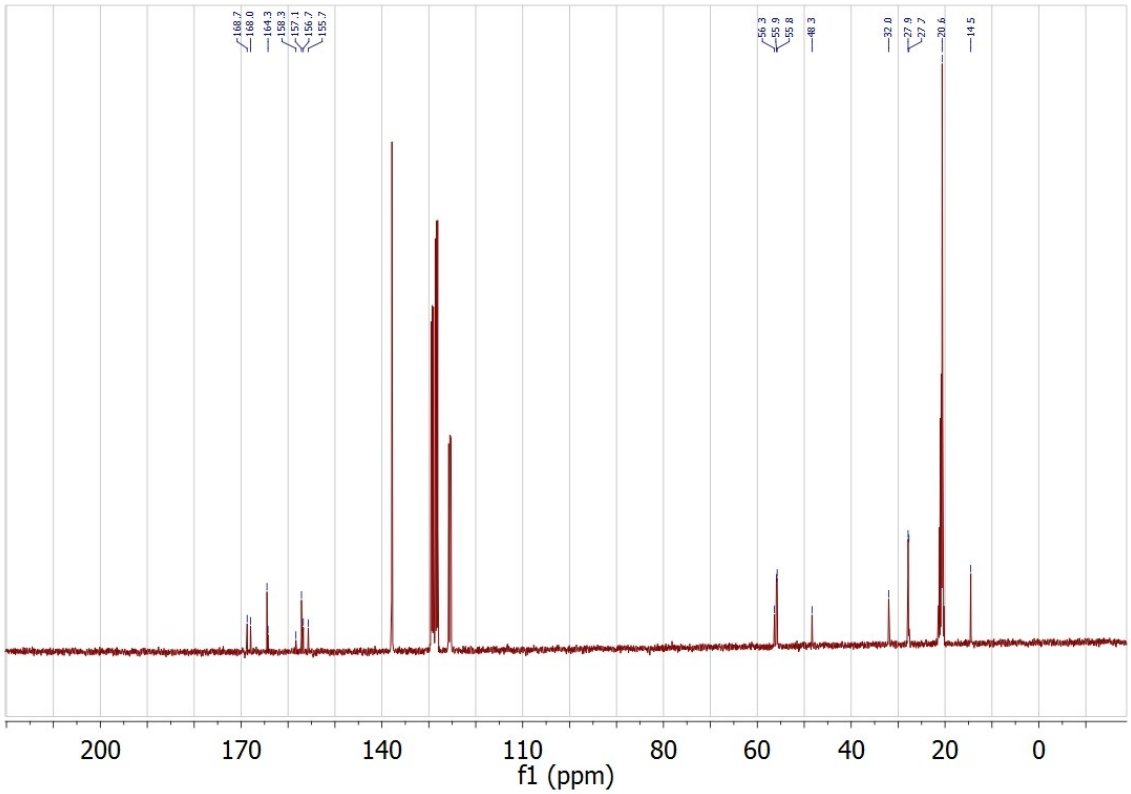

Figure S22 : ^{13}C NMR spectrum of compound **3** (d_8-toluene, 100 MHz, 298 K).

Variable temperature NMR

Methodology

We used the Eyring method[17] to calculate the activation free energy of rotation at the coalescence temperature. The Eyring equation used is the following:

$$\Delta G = 19.14 * T_c[9.972 + \log\left(\frac{T_c}{\delta\nu}\right)] \text{ with } \Delta G \text{ in J.mol}^{-1}$$

In this equation, T_c (in K) is the coalescence temperature and $\delta\nu$ (in Hz) is the chemical shift difference between the two sites. $\delta\nu$ is calculated on the spectrum registered at the lowest temperature.

Temperature range varies from 223K to 353K. Spectra are plotted from 223K (bottom) to 353K (top), with a 10K step.

Only the hydrogen atoms of the diisobutyl groupings are studied here, given that there is no splitting in the signals of the n-butyl grouping linked to the bridging nitrogen atoms.

Results for 1a

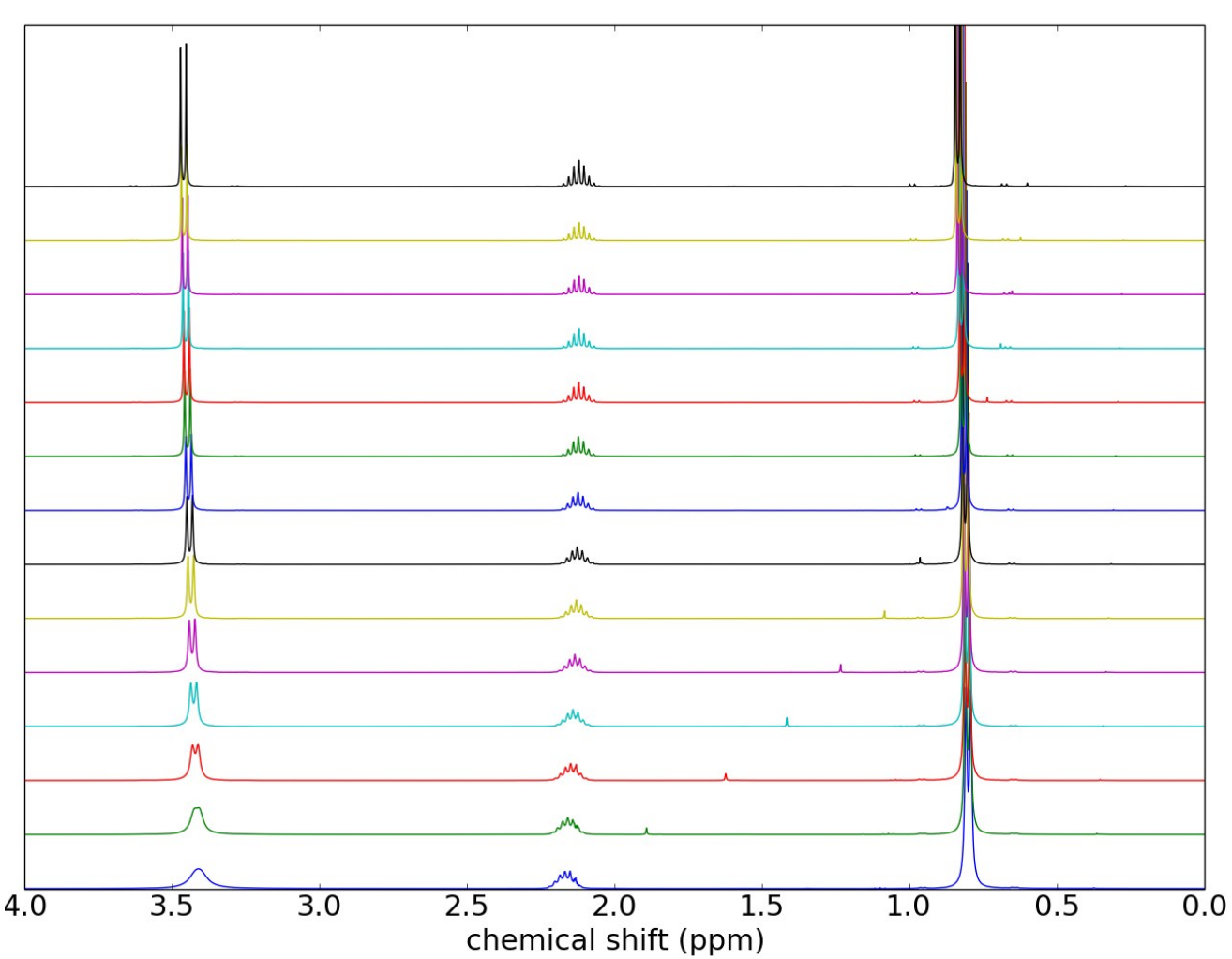

Figure S23 : Evolution of **1a** ^{1}H NMR spectrum from 223K (bottom) to 353K (top), with a 10K step.

Results for 2

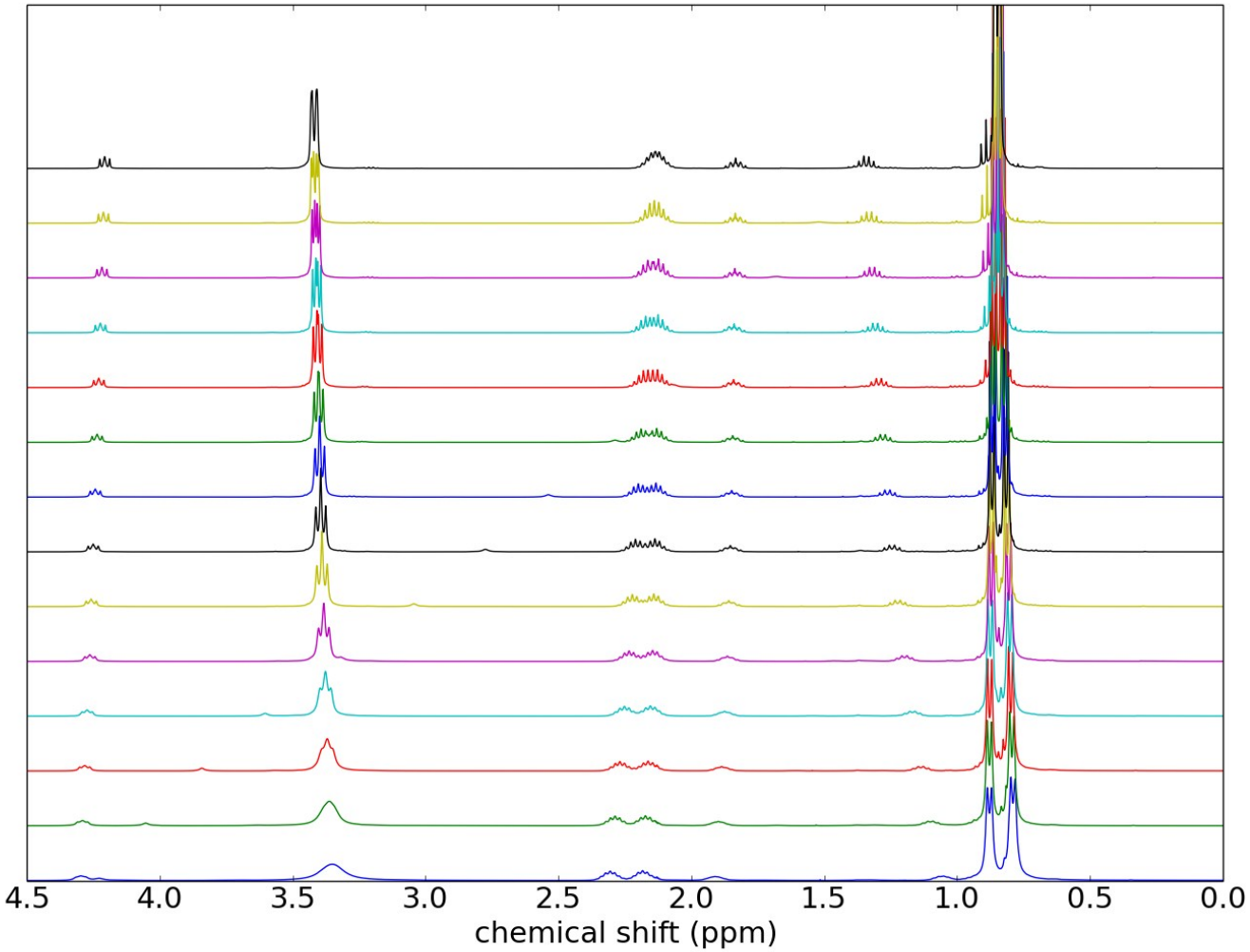

N-CH_2-CH-$(CH_3)_2$			
δ (ppm)	T_c (K)	$\delta\nu$ (Hz)	ΔG (kJ.mol^{-1})
3.40	353	7.95	78.5

Figure S24: Evolution of **2** ^{1}H NMR spectrum from 223K (bottom) to 353K (top), with a 10K step.

Results for 3

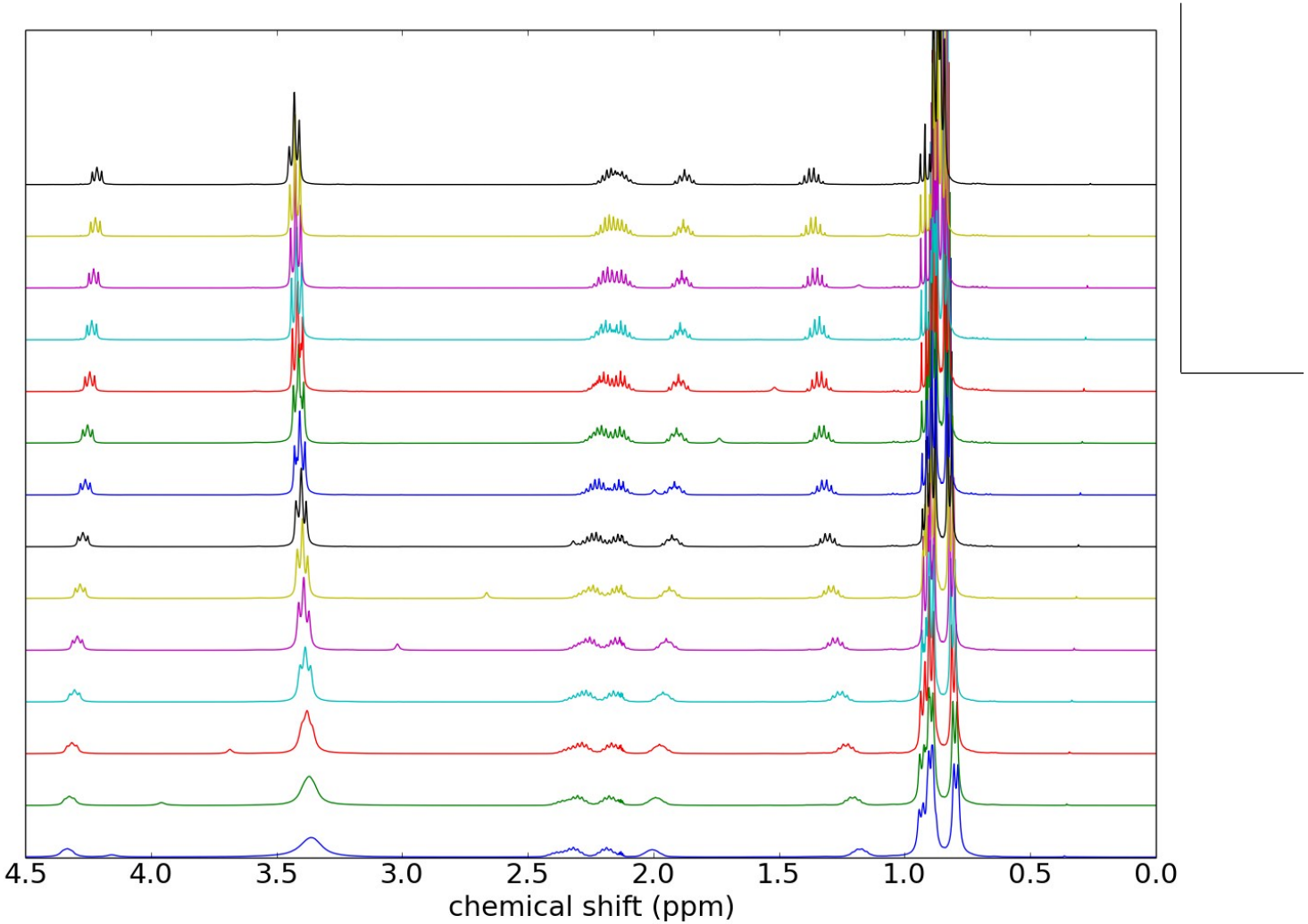

Figure S25 : Evolution of **3** ^{1}H NMR spectrum from 223K (bottom) to 353K (top), with a 10K step.

X-Ray diffraction

Diffraction data were taken using an Oxford-Diffraction XCalibur S kappa geometry diffractometer (Mo-Kα radiation, graphite monochromator, λ = 0.71073 Å). Data were collected at 150 K. The cell parameters were obtained with intensities detected on three batches of 5 frames. The crystal-detector distance was 4.5 cm. The number of settings and frames has been established taking in consideration the Laue symmetry of the cell by CrysAlisPro Oxford-diffraction software[18]. 253 for **1a**, 488 for **2** narrow data were collected for 1° increments in ω with a 30 s exposure time for **1a** and 120 s for **2**. Unique intensities detected on all frames using the Oxford-diffraction Red program were used to refine the values of the cell parameters. The crystal shape determination allows analytical absorption correction to be applied using with the ABSPACK Oxford-diffraction program[19]. Space groups were determined from systematic absences, and they were confirmed by the successful solution of the structure. The structures were solved by charge flipping method using Superflip software[20]. All non-hydrogen atoms were found by difference Fourier syntheses and refined on F^2. Hydrogen atoms were fixed in ideal position and refined with a riding model. Full crystallographic details are given in Table S1.

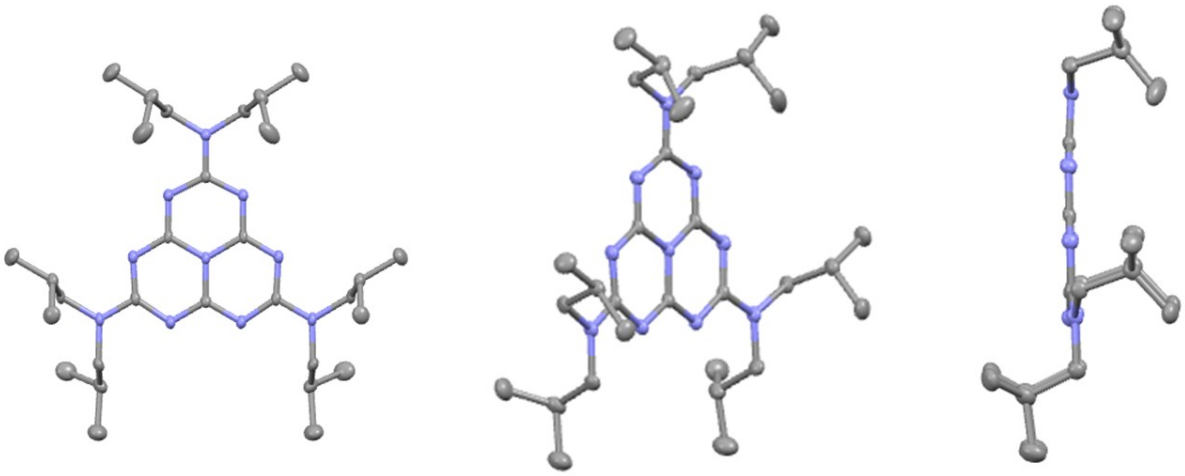

Figure S26 : the Mercury[21] representations of 1a with 50% probability ellipsoids, in different orientations , according to single-crystal X-ray analysis (dichloromethane molecules and hydrogen atoms were omitted for clarity).

Compound	**1a**	**2**
Formula	$C_{31}\ H_{56}\ Cl_2\ N_{10}$	$C_{60}\ H_{91}\ N_{21}\ O_4$
Crystal size [mm]	0.731 x 0.179 x 0.089	0.286 x 0.170 x 0.115
Crystal system	Monoclinic	Monoclinic
Space group	$P2_1/m$	$P2_1/c$
V [Å^3]	1758.4(3)	6430.7(9)
a [Å]	5.8762(9)	21.4140(19)
b [Å]	23.960(2)	11.9388(9)
c [Å]	12.4969(12)	25.308(2)
α [°]	90	90
β [°]	91.956(10)	96.333(8)
γ [°]	90	90
Z	2	4
Absorption coefficient [mm^{-1}]	0.221	0.080
F (000)	692	2520
T [K]	150	150
Total no. reflexions	10754	56382
Unique reflexions [R(int)]	5406 [0.0477]	13115[0.1151]
Final R indices [I>2σ(I)]	R1=0.0788, wR2=0.200	R1=0.0677, wR2=0.1180
Largest diff. peak and hole [eA^{-3}]	0.672 and -0.922	0.903 and -0.245
GOF	1.051	1.005

Table S1 : X-ray crystallographic data.

UV/vis spectra

Experimental

Figure S27 :
UV/Vis absorption spectra of **1a** in acetonitrile, at room temperature.

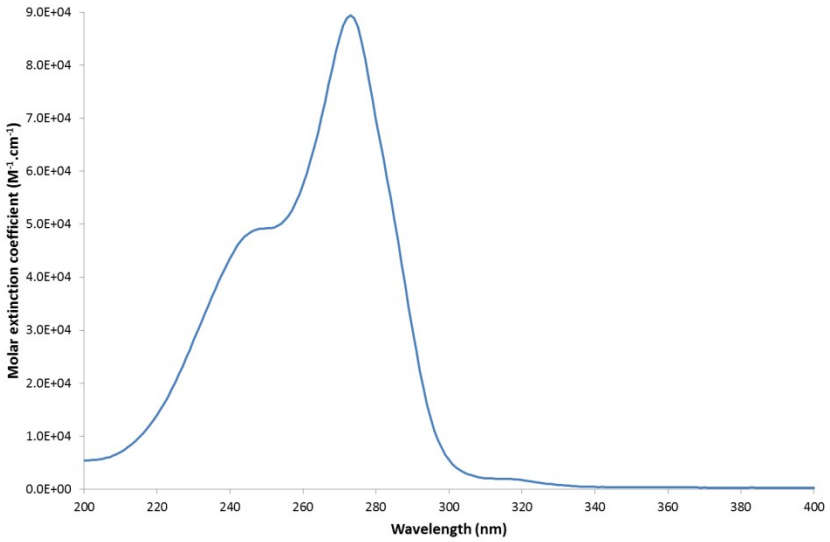

Figure S28 :
UV/Vis absorption spectra of **1b** in acetonitrile, at room temperature.

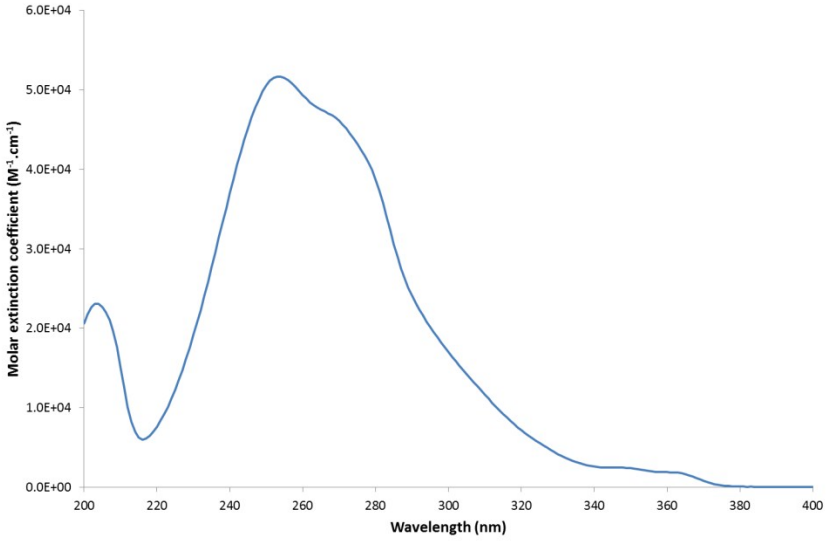

Figure S29 :
UV/Vis absorption spectra of **1c** in acetonitrile, at room temperature.

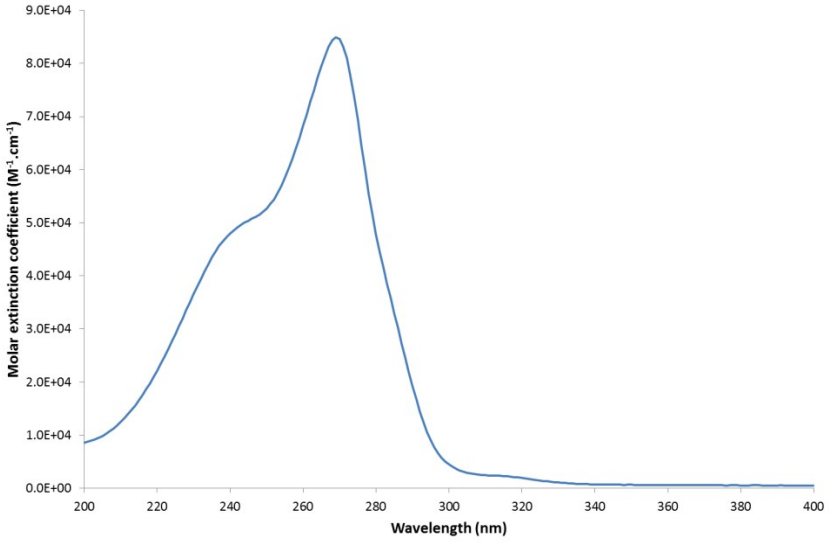

Figure S30 :
UV/Vis absorption spectra of **1d** in acetonitrile, at room temperature.

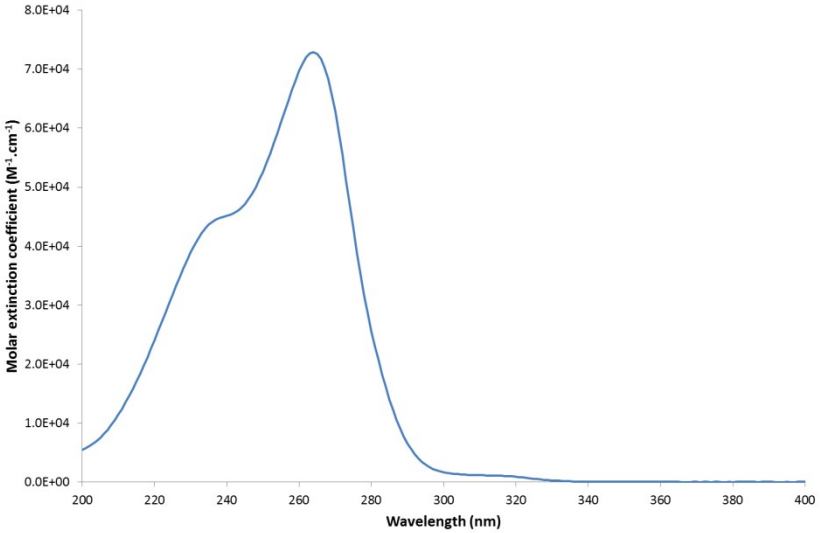

Figure S31 :
UV/Vis absorption spectra of **2** in acetonitrile, at room temperature.

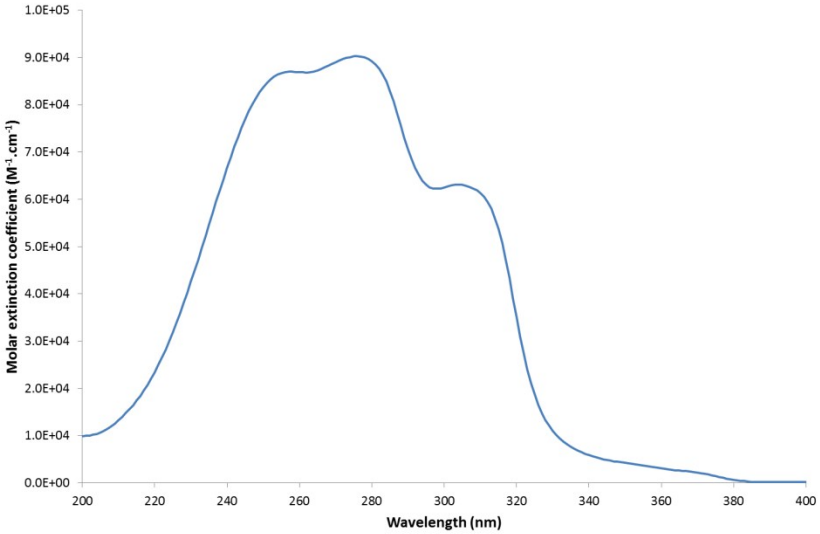

Figure S32 :
UV/Vis absorption spectra of **3** in acetonitrile, at room temperature.

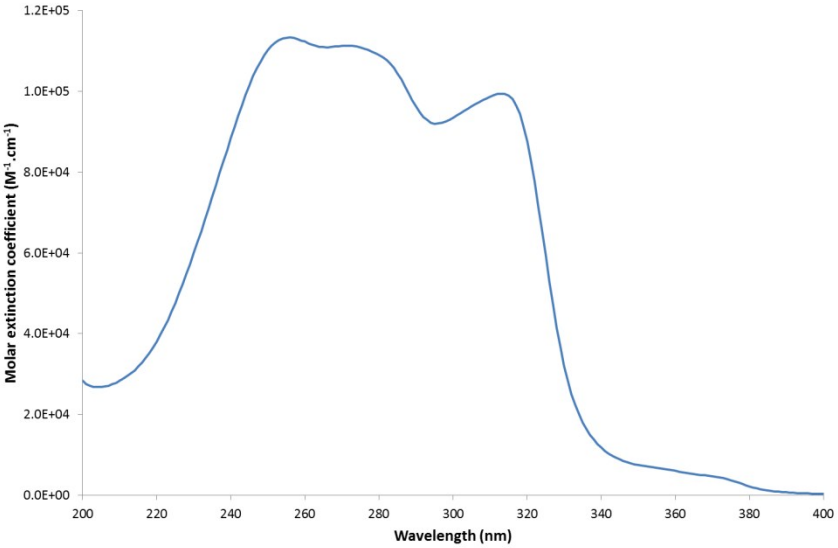

DFT calculations

Glossary

First a scheme with the name used for the different type of atoms in the studied molecules is presented:

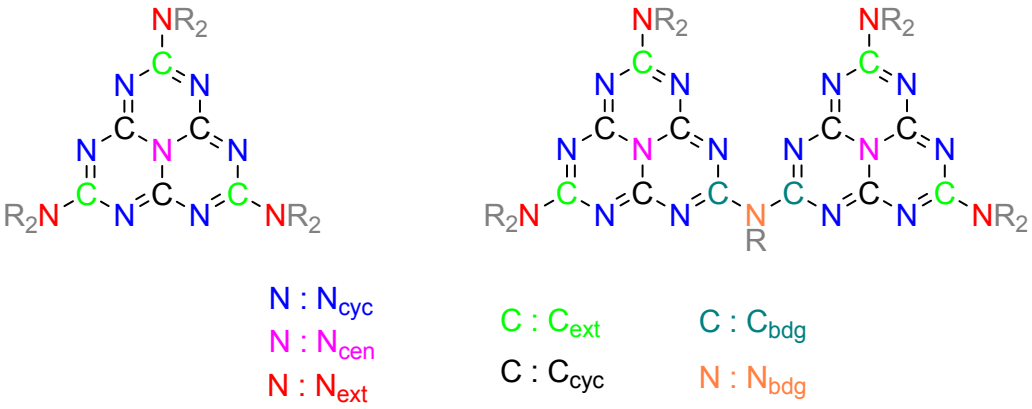

General comment

The electronic structures computed for all systems (monomer **1a**, dimer **2** and trimer **3**) exhibit a significant HOMO-LUMO gap in their neutral redox states (3.56 eV, 2.97 eV and 2.90 eV, respectively; see Table S12) as well as near orbital degeneracy of the occupied orbitals. As a consequence, the relative order of the occupied orbitals close to (and including) the HOMO turns out to be very sensitive to the choice of exchange-correlation (XC) potential, resulting sometimes into orbital permutations in the neutral states (for which UV-visible spectra have been computed) as well as electronic convergence problems for the oxidized states (solved for the monomer **1a** thanks to its C_3 molecular symmetry: see DFT Methodology section). In the present section devoted to UV-visible spectra, the orbitals referred to in Tables S2-3 (neutral monomer), Tables S6-7 (neutral dimer) and Tables S10-11 (neutral trimer) are computed with the SAOP XC potential. To establish a correspondence with those orbitals computed with the B3LYP XC potential (used for redox potentials' calculations) and reported (for some of them) at the end of the Supplementary Material, see Table S2 for some of the molecular orbitals for the three neutral states.

MO correspondence for the oligomers' neutral states					
Monomer		**Dimer**		**Trimer**	
B3LYP	**SAOP**	**B3LYP**	**SAOP**	**B3LYP**	**SAOP**
153: LUMO	153: LUMO	252: LUMO	252: LUMO	351: LUMO	351: LUMO
152: HOMO	150	251: HOMO	251: HOMO	350: HOMO	350: HOMO
150/151	151/152: HOMO(deg.)	250	248	349	348
149	149	249	250	348	349
148	148	248	249	347	347

Table S2 : MO correspondence for the oligomers' neutral states.

Monomer models

We performed TD-DFT calculations of UV-visible spectra for three monomer models, with a C_3 symmetry: i) a **1a** model, with three planar C_{ext}-N_{ext} dihedral angles (i.e. the core group and the three ligands are coplanar); ii) other models where the three peripheral ligands have been rotated by 15°, 30°, 45°, 60°, 75° and 90°, to see the influence of these ligands' orientations on one specific transition discussed below (i.e. C_{ext}-N_{ext} dihedral angle); iii) melem models where the three peripheral NH_2 have been rotated by 15°, 30°, 45°, 60°, 75° and 90°.

1a model

#	Exc. E(nm)	f(a.u.)	orbitals	main character
6	322	0.0915	152→153(79%)	N_{ext}→C_{ext}
7	322	0.0915	151→153(79%)	N_{ext}→C_{ext}
18	292	0.0502	151→155(31%),152→154(31%)	N_{ext}→ $(C/N)_{cyc}$
19	292	0.0502	152→155(31%),151→154(31%)	N_{ext}→ $(C/N)_{cyc}$
26	278	0.0455	149→154(63%)	N_{ext}/N_{cyc} → $(C/N)_{cyc}$
27	278	0.0455	149→155(63%)	N_{ext}/N_{cyc} → $(C/N)_{cyc}$
37	261	0.0525	146→154(33%),147→155(33%),148→154(22%)	N_{cyc}→ $(C/N)_{cyc}$
38	261	0.0525	147→154(33%),146→155(33%),148→155(22%)	N_{cyc}→ $(C/N)_{cyc}$
41	256	0.8583	150→154(42%), etc.	N_{cyc}→ $(C/N)_{cyc}$
42	256	0.8583	150→155(42%), etc.	N_{cyc}→ $(C/N)_{cyc}$

Table S3 : Results for **1a** model. Excitation numbers (#), wavelengths (nm), oscillator strength (a.u.), molecular orbitals involved, and main characters of the TD-DFT computed transitions.

The main features of the monomer experimental UV-visible spectrum are correctly reproduced by the data computed for the **1a** model, that is, two main experimental peaks around 247 nm and 273 nm, computed at 256 nm and 261/278/292 nm (average: 277 nm), respectively, and the minor shoulder measured at 315 nm and computed at 322 nm. From Table S4, we observe that three molecular orbitals (# 149, 151 and 152) contain a dominant Next contribution, which impact the nature of the first 6 transitions reported in Table S3 (# 6, 7, 18, 19, 26, 27) as they will depend on the relative orientation of the external ligands (via Next) w.r.t. the planar core group. Notice in particular from Table S3 the character of the transition computed at 322 nm: N_{ext} → C_{ext} involving the direct bond between the planar core group (via C_{ext}) and the ligand (via N_{ext}). We expect this transition to be affected by the transition from monomer to dimer.

Notice that the second transition (ext→core) at 0° (278 nm) could be associated with that computed at 292 nm (f=0.100) due to molecular orbital mixture resulting into very similar characters, in which case one would have a composite peak (278-292 nm) of combined (not added) intensities (0.091 & 0.100) depending on the intrinsic peaks' widths.

There is still an overall discrepancy between experimental and TD-DFT relative intensities. In order to check this, we performed an additional TD-DFT calculation for the monomer **1a** with the B3LYP XC potential (Figure S34). This however did not improve the quality of the computed spectrum when compared to experiment, and we did not pursue further this along these lines, as our SAOP results are sufficient to interpret our data for all oligomers (**1a**, **2** and **3**).

Because of the expected sensitivity of the first 6 transitions reported in Table S3 on the relative orientation of the ligands (via Next), we performed additional TD-DFT calculations for which the external ligands have been rotated by 15°, 30°, 45°, 60°, 75° and 90°.

# orb. (occ.)	N_{cen}	N_{cyc}	C_{cyc}	N_{ext}	C_{ext}	main character
146 (2)	7.2%	**75.3%**				N_{cyc}
147 (2)	7.2%	**77.4%**				N_{cyc}
148 (2)		**70.2%**				N_{cyc}
149 (2)	9.8%	23.7%		**30.9%**		N_{ext}/N_{cyc}
150 (2)		**95.9%**				N_{cyc}
151 (2)		22.7%		**44.0%**		N_{ext}/N_{cyc}
152 (2)		25.8%		**44.0%**		N_{ext}/N_{cyc}
153 (0)	13.2%		24.6%	16.6%	**42.3%**	C_{cyc}
154 (0)		**40.2%**	**40.9%**	5.0%	14.4%	$(C/N)_{cyc}$
155 (0)		**35.5%**	**40.9%**	6.0%	17.3%	$(C/N)_{cyc}$

Table S4 : Results for **1a** model. Content (> 5%) of the main molecular orbitals involved in the TD-DFT computed transitions.

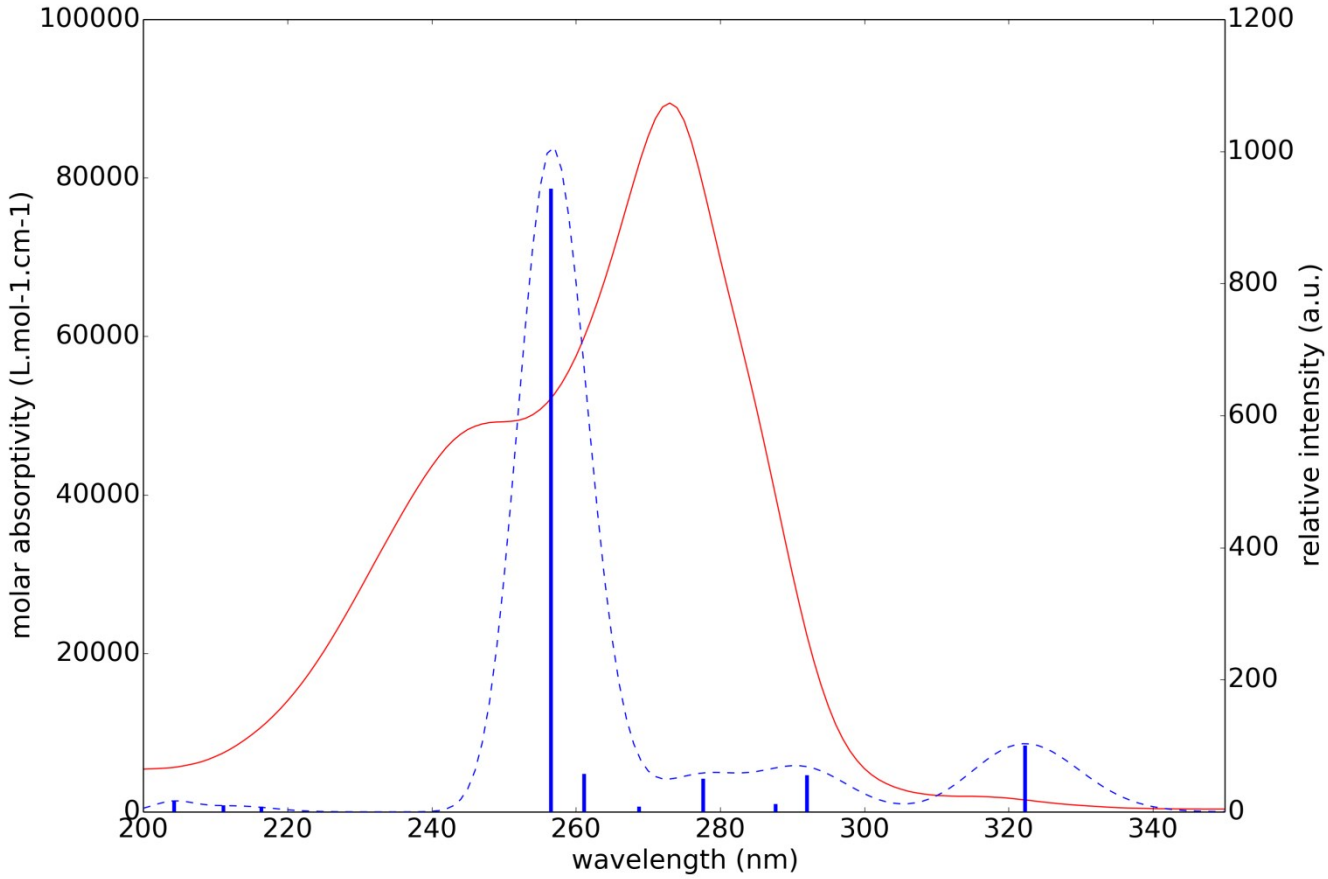

Figure S33 : Simulated UV-visible spectrum for **1a** model (dashed blue line: simulated envelope); blue bars: single transitions) versus experimental spectrum (red).

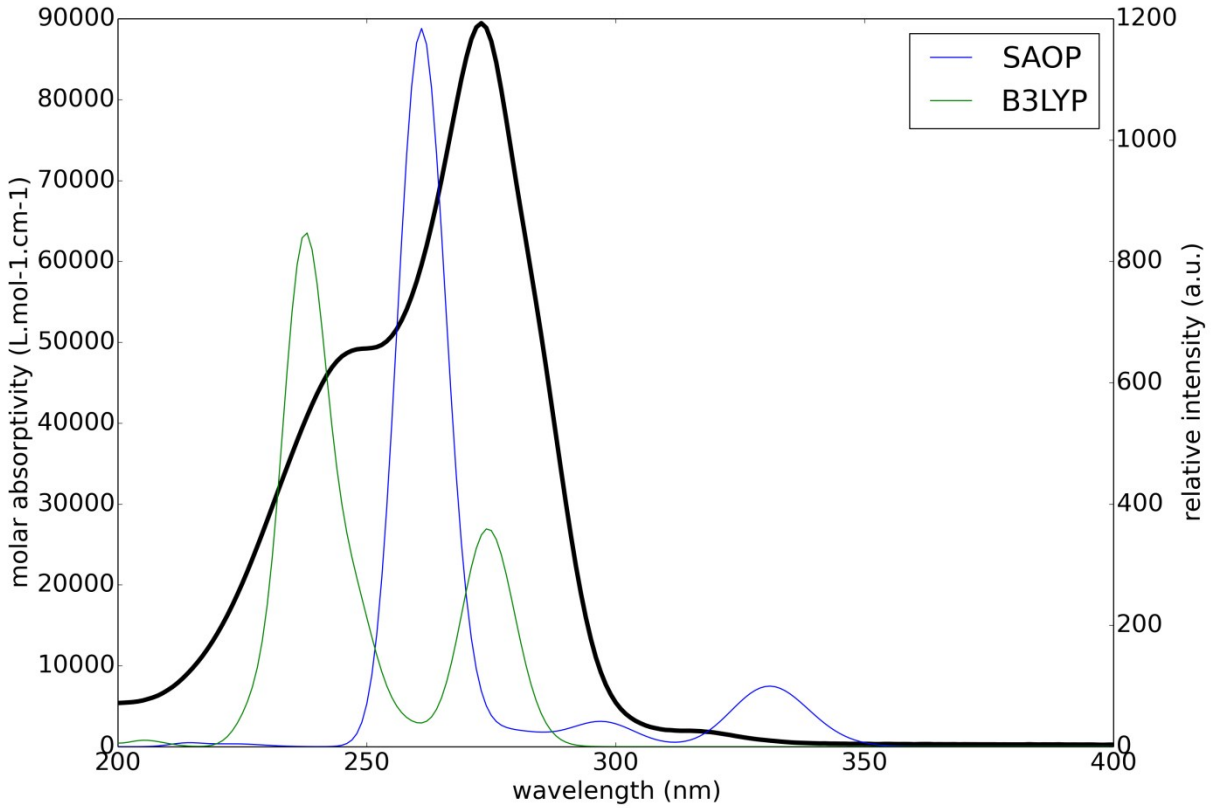

Figure S34 : Influence of the DFT potential on the simulated absorption spectra versus experimental spectrum (black). The B3LYP potential turned out to be unreliable here, especially to reproduced any features above 300 nm.

Rotation of peripheral groups in 1a models

We followed the variation of three specific peaks as a function of the relative (concerted, i.e., while keeping an overall C_3 symmetry) rotation of the peripheral ligands w.r.t. the planar core, rotation measured by the dihedral angle around N_{ext}-C_{ext}. Results are shown in Table S5. The first peak corresponds to (the most red-shifted) $N_{ext}/N_{cyc})\rightarrow C_{ext}$ (or "ext→ext") transition (expected therefore to be very sensitive to rotation), the second one to a $N_{ext}/N_{cyc}\rightarrow (C/N)_{cyc}$ (or "ext→core") transition (expected to be less sensitive than the previous one), and the third one to a $N_{cyc}\rightarrow(C/N)_{cyc}$ (or "core→core") transition (expected to be little sensitive to rotation).

The relative degree of sensitivity is as anticipated based on the transitions 'characters (Figure S35). This goes hand-in-hand with the progressive decrease of the HOMO-LUMO gap (computed by TD-DFT as the transition # 1): 352 nm (0°), 425 nm (45°) and 810 nm (90°).

Moreover, in terms of oscillator strengths, it can be observed that the (oscillator) strength of the third (core→core) transition (proportional to the transition energy × the transition dipole moment squared, decreasing along y; core in xy plane) turns out to be very sensitive to rotation, whereas the other two transitions are much less sensitive with that respect.

	$N_{ext}/N_{cyc} \rightarrow C_{ext}$ **(ext→ext)**	$N_{ext} \rightarrow (C/N)_{cyc}$ **(ext→core)**	$N_{cyc} \rightarrow (C/N)_{cyc}$ **(core→core)**	HOMO-LUMO gap
0°	322 nm f = 0.183	278/292 nm f = 0.091/0.100	256 nm f = 1.712	348 nm
15°	325 nm f = 0.188	281/291 nm f = 0.089/0.093	257 nm f = 1.834	351 nm
30°	346 nm f = 0.214	291 nm f = 0.274	266 nm f = 1.400	378 nm
45°	386 nm f = 0.239	313 nm f = 0.482	276 nm f = 0.644	425 nm
60°	455 nm f = 0.226	356 nm f = 0.332	284 nm f = 0.402	502 nm
75°	583 nm f = 0.118	425 nm f = 0.097	290 nm f = 0.253	645 nm
90°	750 nm f = 0.003	482 nm f = 0.001	294 nm f = 0.073	810 nm

Table S5 : Evolution of different transitions' wavelengths for different rotations of the **1a** model.

	Relative energies (kJ/mol/group)	
Rotation angle	**Monomer 1a**	**Melem**
0°	0.0	0.0
15°	4.2	5.3
30°	17.7	20.2
45°	38.2	42.6
60°	63.4	70.4
75°	89.3	93.8
90°	107.1	106.2

Table S6 : Relative energies (kJ/mol/group) for monomer **1a** and melem as a function of the rotation angle between the heptazine plane and the external NR_2 group at the DFT-XC(gga)level (see DFT Methodology section).

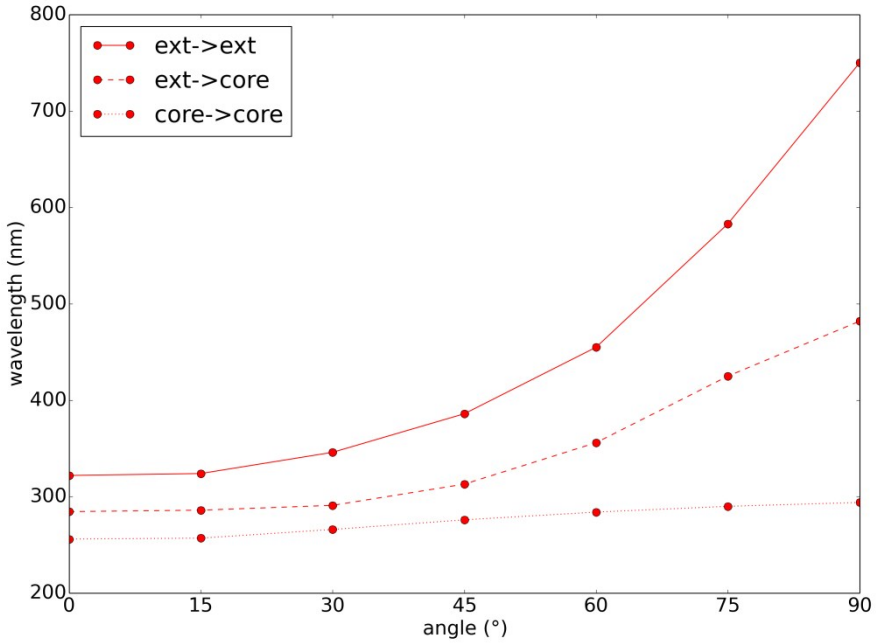

Figure S35 : Evolution of the transition wavelengths with $N(^{i}Bu)_2$ rotation for **1a** models.

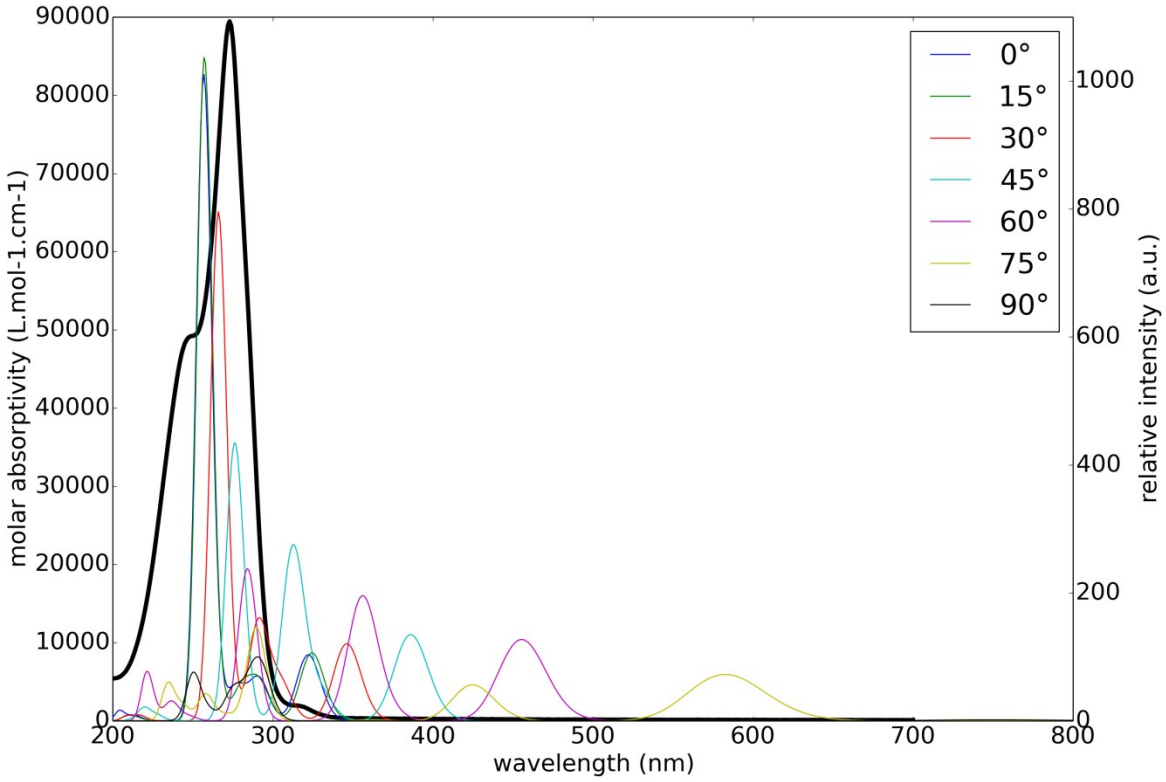

Figure S36 : Simulated UV-visible spectra for the rotated **1a**, compared with experimental spectra (thick black line).

Melem models

We followed the variation for melem of two specific peaks as a function of the relative (concerted, i.e., while keeping an overall C_3 symmetry) rotation of the peripheral NH_2 w.r.t. the planar core, rotation measured by the angle H-N_{ext}-C_{ext}-C_{cyc} angle (0°, 15°, 30°, 45°, 60°, 75° and 90°). The first peak corresponds to the most red-shifted transition of the type N_{cyc}→(C_{cyc}/C_{ext}) transition, and the second one to a N_{ext}→(C_{cyc}/C_{ext}) transition.

The two transitions are sensitive to rotation: the first and second peak have respectively 154 and 80 nm red-shifts at 75° compared to 0°. The conclusion is that the presence of alkyl chains leads to an offset compared to hydrogen, and that a rotation of the peripheral groups leads to a red-shift, which is amplified with alkyl chains.

	N_{cyc}→(C_{cyc}/C_{ext})	N_{ext}→(C_{cyc}/C_{ext})	HOMO-LUMO gap
0°	264 nm f = 0.145	212 nm f = 2.009	337 nm
15°	266 nm f = 0.117	215 nm f = 1.922	342 nm
30°	307 nm f = 0.008	223 nm f = 1.653	357 nm
45°	330 nm f = 0.017	238 nm f = 1.193	382 nm
60°	363 nm f = 0.027	264 nm f = 0.497	413 nm
75°	418 nm f = 0.043	285/292 nm f = 0.104/0.145	444 nm
90°	f = 0.0	293 nm f = 0.169	492 nm

Table S7 : Evolution of different transitions' wavelengths for different rotations of the melem model.

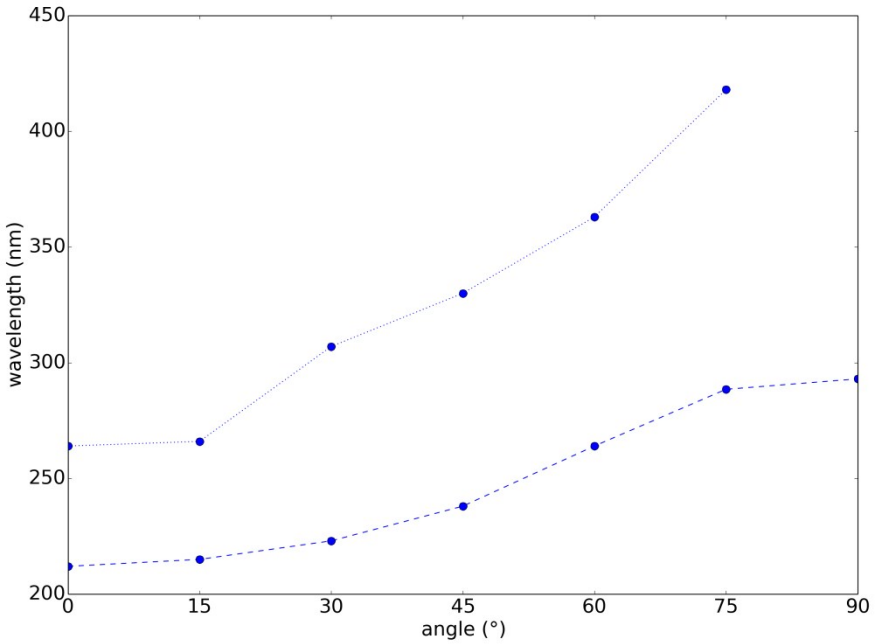

Figure S37 : Evolution of the transition wavelengths with NH_2 rotation for melem models

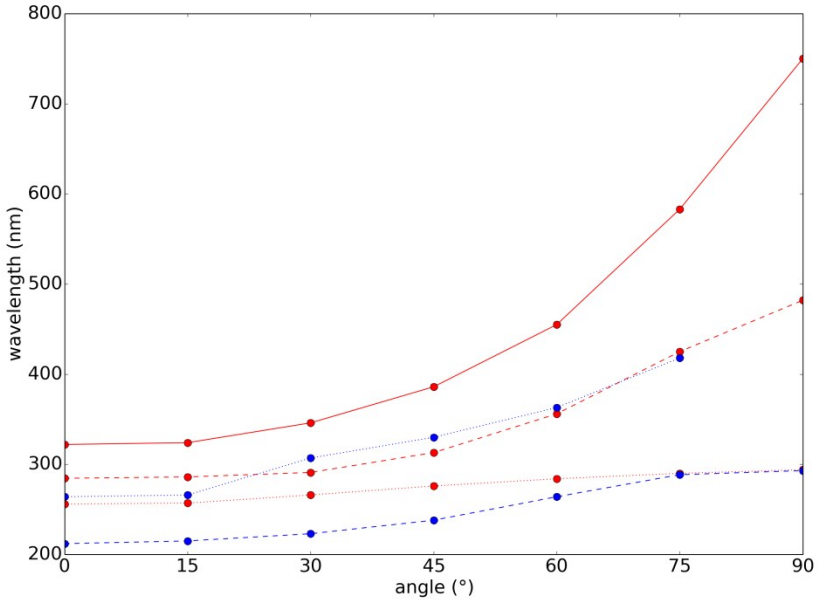

Figure S38 : Evolution of the transition wavelengths with $N(^{i}Bu)_2$ (red dots) and NH_2 (blue dots) rotation for **1a** and melem models

Dimer model

We performed TD-DFT calculations of UV-visible spectra for three dimer models: i) an optimized model of **2**, with four coplanar C_{ext}-N_{ext} dihedral angles, and a dihedral angle between the two heptazine units of 26.9° ii) another model where the four peripheral ligands have been rotated by 30°, to see the influence of these ligands' orientations; iii) dimelem models where the four peripheral NH_2 and the dihedral angle between the two heptazine have been simultaneously rotated by 30°, 60° and 90°; iv) dimelem models where the four peripheral NH_2 have a 0° angle, and the dihedral angle between the two heptazines has been rotated by 30°, 60° and 90°.

Optimized model of 2

#	Exc. E(nm)	f(a.u.)	orbitals	main character
11	370	0.1577	**247**→252(92%)	$N_{ext}/N_{cyc} \rightarrow C_{bdg}/C_{cyc}$
14	354	0.0557	245→252(92%)	$N_{cyc} \rightarrow C_{bdg}/C_{cyc}$
34	323	0.1762	239→252(32%),**241**→252(24%), etc.	$N_{cyc} \rightarrow C_{bdg}/C_{cyc}$
40	316	0.2157	239→252(60%)	$N_{cyc} \rightarrow C_{bdg}/C_{cyc}$
46	310	0.1369	251→255(70%)	$N_{cyc} \rightarrow (C/N)_{cyc}$
54	304	0.0520	250→254(39%)	$N_{ext}/N_{cyc} \rightarrow (C/N)_{cyc}$, C_{ext}
88	286	0.0485	245→255(57%)	$N_{cyc} \rightarrow (C/N)_{cyc}$
101	278	0.0571	245→256(24%),246→256(14%),etc.	$N_{cyc} \rightarrow (C/N)_{cyc}$
117	272	0.0628	245→**257**(33%), 243→255(24%),etc.	$N_{cyc} \rightarrow (C/N)_{cyc}$
140	261	0.0770	243→**257**(44%), etc.	$N_{cyc} \rightarrow (C/N)_{cyc}$
141	260	0.1070	**241**→256(28%), 240→256(16%),etc.	$N_{cyc} \rightarrow (C/N)_{cyc}$
142	259	0.0664	**244**→**257**(36%), **242**→**257**(13%),etc.	$N_{cyc} \rightarrow (C/N)_{cyc}$
144	258	0.0558	240→256(18%), 243→**257**(10%),etc.	$N_{cyc} \rightarrow (C/N)_{cyc}$
147	257	0.0132	239→255(80%), etc.	$N_{cyc} \rightarrow (C/N)_{cyc}$
148	257	0.6618	248→**257**(15%), etc.	$N_{cyc} \rightarrow (C/N)_{cyc}$
149	256	0.3245	**242**→**257**(26%), **241**→**257**(12%),etc.	$N_{cyc} \rightarrow (C/N)_{cyc}$
150	255	0.2421	**241**→**257**(43%), 240→**257**(17%),etc.	$N_{cyc} \rightarrow (C/N)_{cyc}$

Table S8 : Results for the optimized **2** model. Excitation numbers (#), wavelengths (nm), oscillator strength (a.u.), molecular orbitals involved, and main characters of the TD-DFT computed transitions.

The main features of the experimental spectrum are reproduced computationally, that is five apparent peaks at 257 nm (computed: 256 nm), 276 nm (computed: 261, 272, 278 and 286 nm), 317 nm (computed: 310, 316 and 323 nm), 354 nm and 370 nm (cf. Figure S39) to be compared to the experimental peaks at 256 nm, 274 nm, 304 nm and 350 nm and 367 nm, respectively. It is especially interesting to notice that the monomeric feature predicted by TD-DFT at 346 nm in case of external ligand rotation w.r.t. the planar core group ($N_{ext} \rightarrow C_{ext}$) now appears computationally for **2** at 370 nm (identified with the experimental peak at 367 nm).

# orb.	N_{bdg}	N_{cen}	N_{cyc}	C_{cyc}	N_{ext}	C_{ext}	C_{bdg}	main character
239			75.3%					N_{cyc}
240			73.7%					N_{cyc}
241	**5.7%**	7.1%	55.7%					N_{cyc}
242	**9.3%**	6.6%	53.9%					N_{cyc}
243			62.5%					N_{cyc}
244	**5.6%**		62.6%					N_{cyc}
245			73.2%					N_{cyc}
246		6.8%	18.1%		32.8%			N_{ext}
247	**7.8%**		27.0%		27.4%			N_{ext}/N_{cyc}
248			97.5%					N_{cyc}
250			38.4%		34.0%			N_{ext}/N_{cyc}
251			68.0%		9.4%			N_{cyc}
252		9.9%	8.7%	20.7%		9.0%	**31.0%**	C_{bdg}/C_{cyc}
254			23.7%	33.2%	7.2%	19.8%		$(C/N)_{cyc}$, C_{ext}
255			29.0%	39.2%		14.4%		$(C/N)_{cyc}$
256			29.6%	38.2%		15.3%		$(C/N)_{cyc}$
257	**7.0%**		28.8%	40.1%			**14.9%**	$(C/N)_{cyc}$

Table S9 : Results for the optimized **2** model. Content (> 5%) of the main molecular orbitals involved in the TD-DFT computed transitions.

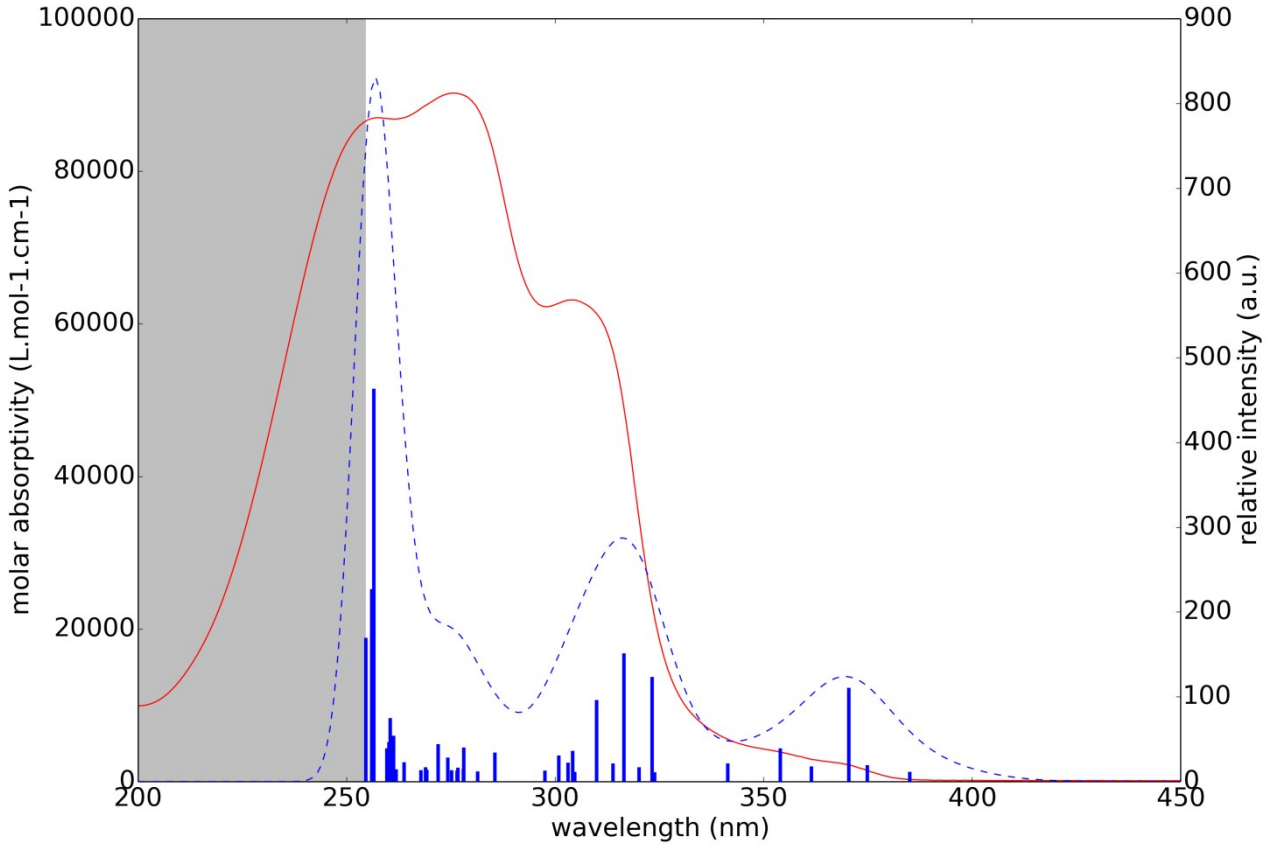

Figure S39 : Simulated UV-visible spectrum for **2** model (dashed blue line: simulated; blue bars: single transitions) versus experimental spectrum (red). Grey area: no calculations.

Rotation of peripheral groups in 2 models

TD-DFT calculations on **2** in which all peripheral $N(^iBu)_2$ are rotated by 30° are also performed. Results are shown in Table S9. As observed for **1a**, a red-shift of all transitions occurs when the peripheral groups are rotated, which is more important when the external atoms orbitals are involved in the transition.

	$N_{ext}/N_{cyc} \rightarrow C_{ext}/C_{cyc}$ **(ext→ext)**	$N_{cyc} \rightarrow C_{ext}/C_{cyc}$ **(core→ext)**	$N_{cyc} \rightarrow (C/N)_{cyc}$ **(core→core)**	HOMO-LUMO gap
0°	370 nm f = 0.158	323 nm f = 0.216	257 nm f = 0.662	418 nm
30°	398 nm f = 0.103	334 nm f = 0.134	261 nm f = 0.391	419 nm
shift	+28 nm	+11 nm	+4 nm	

Table S10 : Transitions' wavelengths for a 0° and 30° rotation of the $N(^iBu)_2$ groups of **2** model.

	Relative energies (kJ/mol)
Rotation angle	**Dimer 2**
0°	5.4
41.7	0.0
90°	12.6

Table S11 : Relative energies (kJ/mol/group) for dimer **2** as a function of the rotation angle between the two heptazine planes at the DFT-XC(gga)level (see DFT Methodology section).

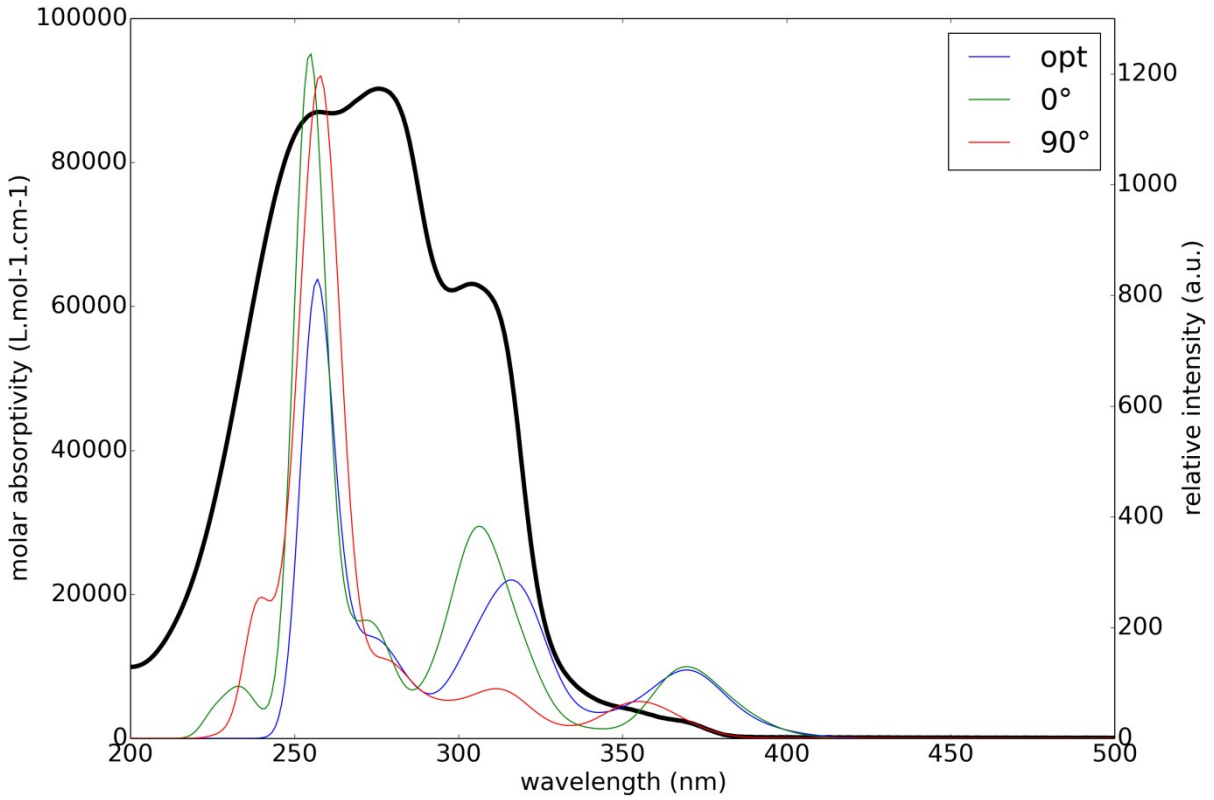

Figure S40 : influence of the dihedral angle between the two heptazine units on the computed absorption spectra of **2** (black line: experimental spectrum ; blue line : optimized geometry)

Rotations in dimelem

TD-DFT calculations on dimelem in which all groups and only the dihedral angle between the two units are rotated, from 0° to 90° (30° step), are also performed. They show that there is a significant little red-shift in the first case (+98nm between 0° and 90°), while there is almost none (+4nm) when only the bridge is rotated. Intensities also slightly decrease when only the bridge is rotated, while there is a dramatic drop when every group is rotated.

	Only bridge rotation		Every group rotation	
	$N_{bdg} \rightarrow C_{bdg}$ **(ext→ext)**	HOMO-LUMO gap	$N_{bdg} \rightarrow C_{bdg}$ **(ext→ext)**	HOMO-LUMO gap
0°	309 nm f = 0.358	400 nm	309 nm f = 0.358	400 nm
30°	309 nm f = 0.399	399 nm	316 nm f = 0.207	412 nm
60°	310 nm f = 0.349	404 nm	333 nm f = 0.098	423 nm
90°	313 nm f = 0.292	407 nm	374 nm f = 0.006	498 nm

Table S12 : Evolution of different transitions' wavelengths for different rotations of the dimelem model.

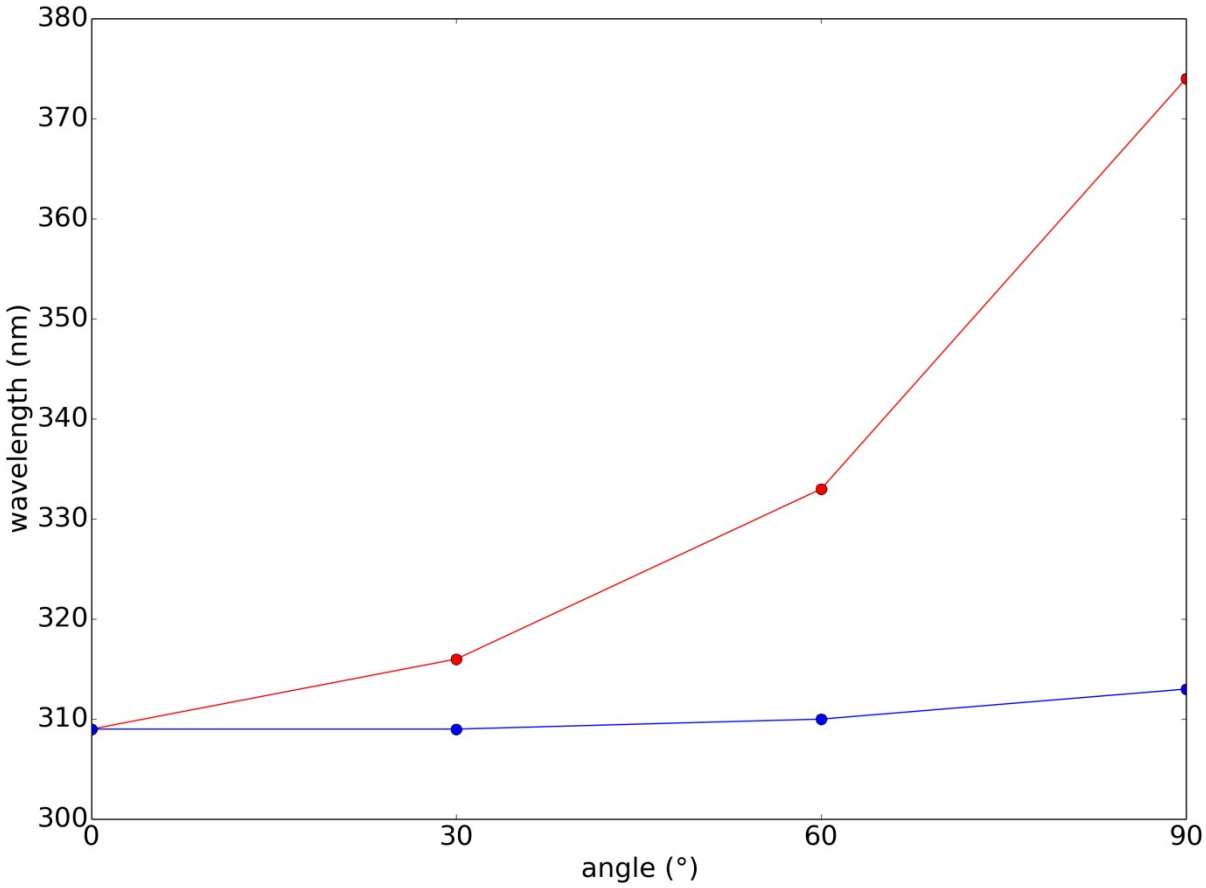

Figure S41 : Influence of the dihedral angle between heptazine units on the ext -> ext transition, for dimelem (blue: only the bridging angle is changed; red: all peripheral NH_2 are tilted by 30°)

Trimer model

We performed TD-DFT calculations of UV-visible spectra for a **3** model. To avoid high calculation time, only the transitions corresponding to the tail of the absorption spectrum (>315nm) were computed.

Focusing here on the red-shifted part of the experimental spectrum (i.e. above 315 nm), we find two small peaks located at about 355 nm and 370 nm. These two features are correctly predicted with apparent peaks (cf. Figure S42) at 350 nm (338, 350 and 359 nm in Table S11) and 390 nm (383 and 395 nm in Table S11).

Interestingly, the two peaks computed around 390 nm correspond mainly to $N_{ext} \rightarrow C_{ext}$ transitions, i.e. they do not contain any N_{bdg} contributions.

On the other hand, one finds two N_{bdg} contributions, the first one in the transition # 29 computed at 368 nm, and the other one in the transition # 54 computed at 338 nm (cf. Table S11). The first value (368 nm, but low f value: 0.0382 a.u.) is reminiscent of what was computed for the dimer (transition # 11 at 370 nm, also containing some N_{bdg} contribution).

#	Exc. E(nm)	f(a.u.)	orbitals	main character
12	400	0.0234	345→351(46%),346→351(42%)	$N_{cyc} \rightarrow C_{bdg}/C_{cyc}$
13	399	0.0386	346→351(46%),344→351(34%)	$N_{cyc} \rightarrow C_{bdg}/C_{cyc}$
14	395	0.0551	344→351(55%),345→351(31%)	$N_{ext}/N_{cyc} \rightarrow C_{bdg}/C_{cyc}$
20	383	0.0465	343→351(80%)	$N_{ext}/N_{cyc} \rightarrow C_{bdg}/C_{cyc}$
21	381	0.0335	350→352(77%)	$N_{cyc} \rightarrow C_{bdg}/C_{cyc}$
27	371	0.0284	348→352(72%)	$N_{cyc} \rightarrow C_{bdg}/C_{cyc}$
29	368	0.0382	**341**→351(83%)	$N_{bdg}/N_{cyc} \rightarrow C_{bdg}/C_{cyc}$
32	364	0.0204	347→352(91%)	N_{ext}/N_{cyc} C_{bdg}/C_{cyc}
37	359	0.1757	345→352(41%), 344→352(16%)	$N_{cyc} \rightarrow C_{bdg}/C_{cyc}$
46	350	0.2278	336→351(71%)	$N_{cyc} \rightarrow C_{bdg}/C_{cyc}$
54	338	0.1124	**335**→351(52%), **341**→352(21%)	$N_{bdg}/N_{cyc} \rightarrow C_{bdg}/C_{cyc}$

Table S13 : Results for the optimized **3** model. Excitation numbers (#), wavelengths (nm), oscillator strength (a.u.), molecular orbitals involved, and main characters of the TD-DFT computed transitions.

# orb.	N_{bdg}	N_{cen}	N_{cyc}	C_{cyc}	N_{ext}	C_{ext}	C_{bdg}	main character
335	**19.3%**	8.1%	31.7%					N_{bdg}/N_{cyc}
336			58.1%					N_{cyc}
339			61.9%					N_{cyc}
340	**11.6%**		47.0%					N_{bdg}/N_{cyc}
341	**9.7%**		58.7%					N_{bdg}/N_{cyc})
343			20.7%		31.2%			N_{ext}/N_{cyc}
344			30.0%		27.8%			N_{ext}/N_{cyc}
345			60.5%		12.2%			N_{cyc}
346			53.7%		20.3%			N_{cyc}
347			34.2%		34.2%			N_{ext}/N_{cyc}
348			63.5%		10.8%			N_{cyc}
350			56.3%		11.5%			N_{cyc}
351		12.4%	8.9%	22.3%		5.3%	**35.2%**	C_{bdg}/C_{cyc}
352		8.0%	14.2%	21.8%		8.9%	**26.4%**	C_{bdg}/C_{cyc}

Table S14 : Results for the **3** model. Content (> 5%) of the main molecular orbitals involved in the TD-DFT computed transitions.

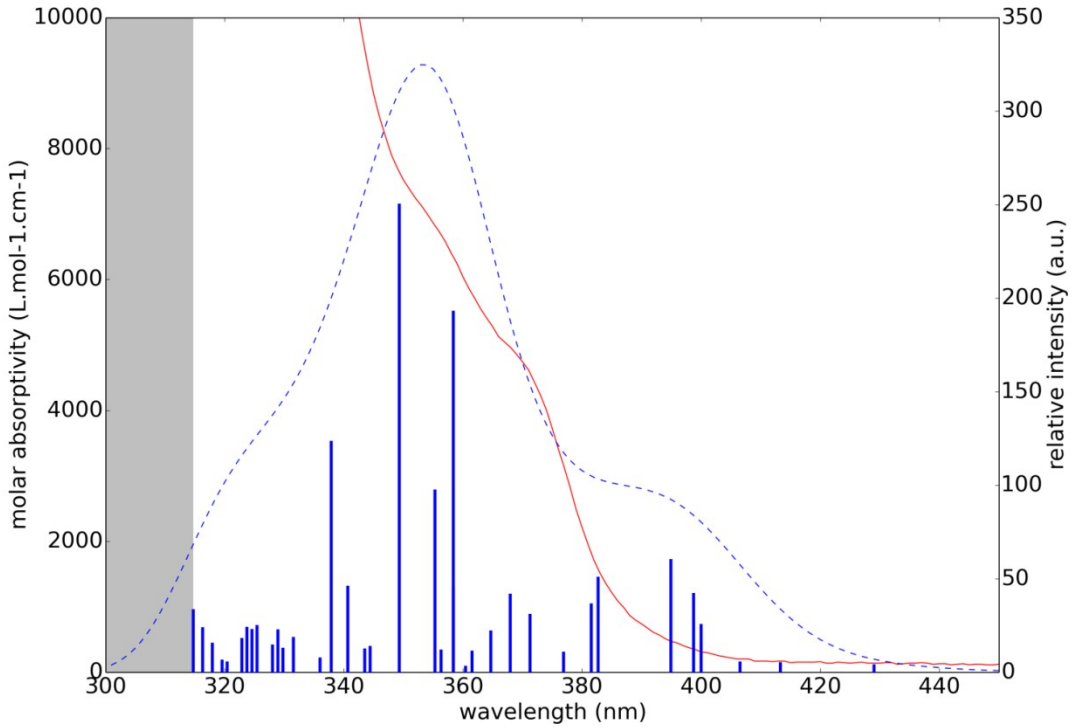

Figure S42 : Simulated UV-visible spectrum for **3** model (dashed blue line: simulated envelope; blue bars: single transitions) versus experimental spectrum (red). Grey area: no calculations.

Summary

As the size of the linear polymer increases, the relative weigh of N_{bdg} is expected to slowly increase with a more-or-less constant contribution around 330-340 nm. On the other hand, the $N_{ext} \rightarrow C_{ext}$ contributions will be more and more red-shifted (322 nm/f=0.183 for the planar monomer, 370 nm/f=0.158 for the dimer, and ~390-400 nm for the trimer.

Independently from its contribution to the UV-visible spectra, the HOMO-LUMO energy gaps computed by TD-DFT (i.e. transitions #1 for the series: monomer, dimer and trimer) decreases.

Note: None of the three (# 1) HOMO→LUMO transitions contribute to the UV-visible spectra (there is no # 1 transitions in Table S3, Table S7 and Table S11).

Models	HOMO→LUMO (nm)	First intense peak visible on exp. spectra (nm)	Computed tail transition(nm) (vs. exp.)
1a	100% 152→153 (**348**)	273	322 (vs. 315)
2	100% 251→252 (**418**)	304	370 (vs. 368)
3	100% 350→351 (**429**)	315	~395 (vs. 370)

Table S15 : Summary of UV-vis properties.

Emission spectroscopy

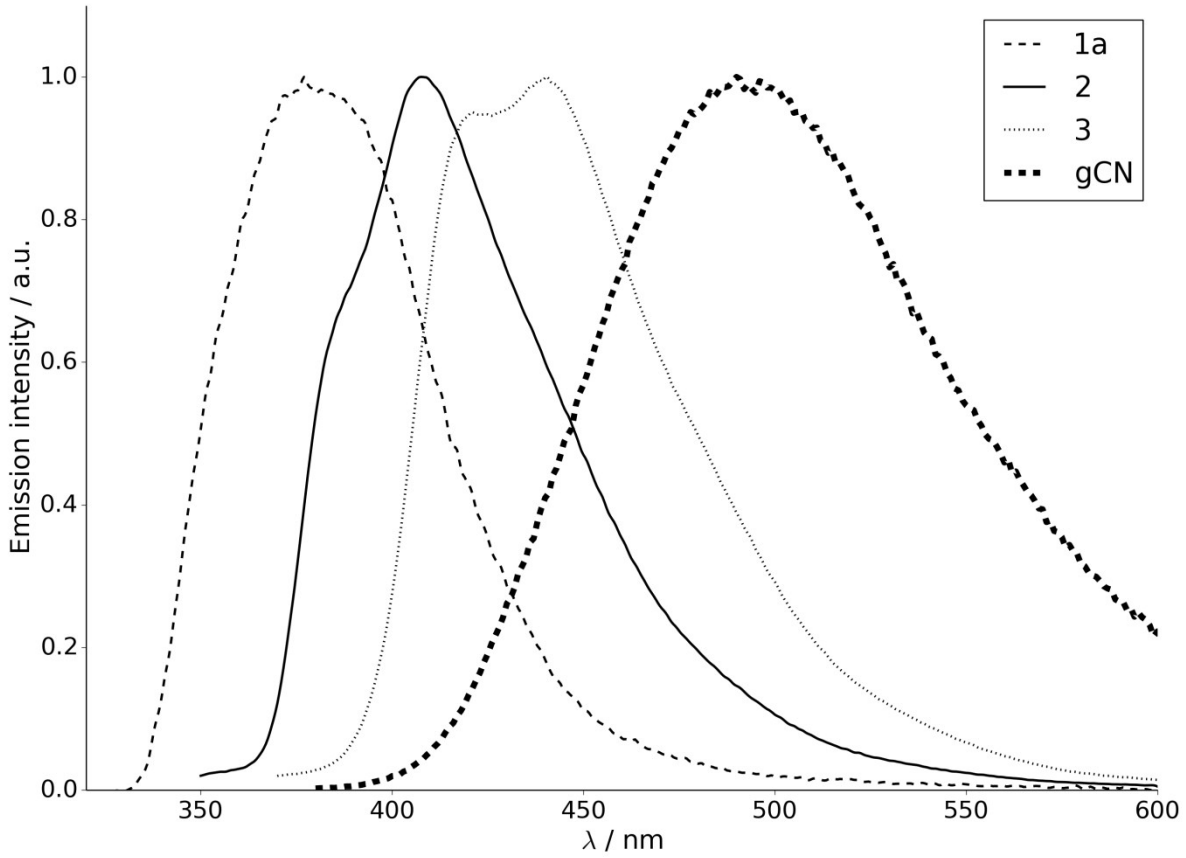

Figure S43: normalized fluorescence spectra of oligomers (in solution in AcN), with gCN (solid state) for comparison. $\lambda_{excitation}$= 273 nm (**1a**) ; 304 nm (**2**) ; 313 nm (**3**) ; corresponding to the most intense measured signal.

Cyclic voltammetry

Experimental

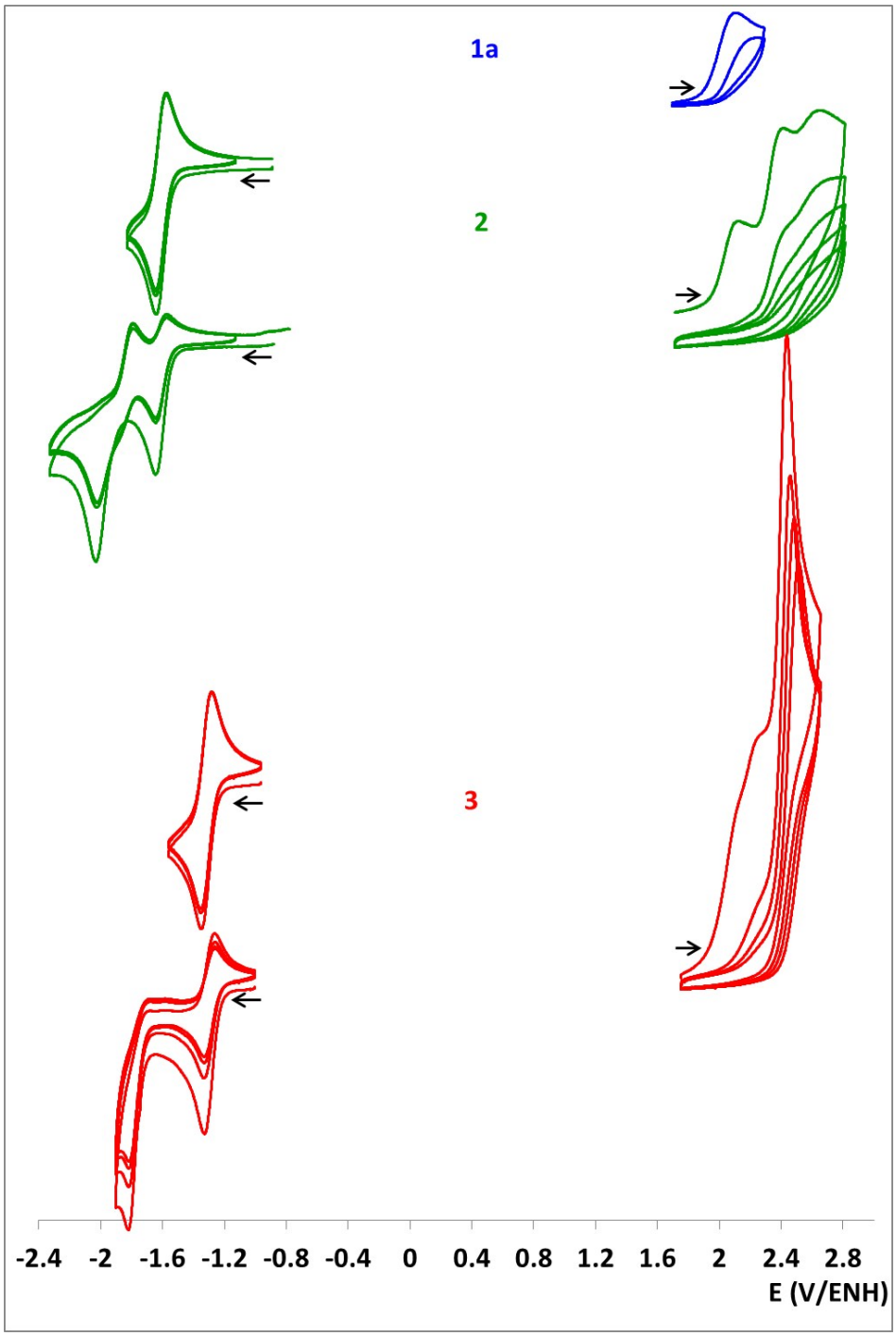

Figure S44: Cyclovoltamograms for **1a** (blue), **2** (green) and **3** (red). In reduction for **2** and **3**, two curves were depicted: top: scanning only the first reduction wave; bottom scanning the second reduction wave. Conditions: room temperature, 1 mM compound, vitreous carbon electrode (dia= 3mm); electrolyte: nBu_4PF_6 (0.1M)/acetonitrile; platinum counter electrode; scan rate: $100mV.s^{-1}$. Arrow indicates starting potential and scanning direction.

DFT calculations

Oxidation state	Computed value	**1a**	**2**	**3**
+1	Energies (eV)[a]	-619.669	-1002.555	-1385.260
	Solvation (eV)[b]	-1.414	-1.629	-1.843
0	Energies (eV)[a]	-626.986	-1009.619	-1392.235
	Solvation (eV)[b]	-0.267	-0.556	-0.852
-1	Energies (eV)[a]	-626.978	-1010.446	-1393.394
	Solvation (eV)[b]	-2.093	-2.435	-2.658

Table S16 **:** All calculations reported in this table have been performed with the ADF2012 DFT code (see DFT Methodology for technical details). (a) Bonding energies E(eV) computed with the B3LYP exchange-correlation potential. (b) Solvation energies computed using the COSMO model (solvent = acetonitrile).

Difference	Computed value	**1a**	**2**	**3**	**range**
(+1) – (0)	IP(0) (eV)[a]	+7.317	+7.064	+6.975	0.34 eV
	$\Delta E_{solv}(0)$ (eV)[b]	-1.147	-1.073	-0.991	0.16 eV
(0) – (-1)	IP(-1) (eV)[a]	-0.008	+0.827	+1.159	**1.17 eV**
	$\Delta E_{solv}(-1)$ (eV)[b]	+1.826	+1.879	+1.806	0.07 eV
	E_{ox} (V)[c]	**+1.89 (exp. 2.10)**	**+1.71 (exp. 2.12)**	**+1.70 (exp. 2.11)**	0.19 eV
	E_{red} (V)[c]	**-2.46 (exp. <-2.4)**	**-1.57 (exp. -1.60)**	**-1.32 (exp. -1.30)**	**1.14 eV**

Table S17 : (a) Ionization potentials IP(eV) for the more reduced member of the redox couple considered. (b) Solvation energy differences ΔE_{solv}(eV). (c) Redox potentials computed from E_{ox} = IP(0) + $\Delta E_{solv}(0)$ -4.28, and E_{red} = IP(-1) + $\Delta E_{solv}(-1)$ -4.28 (with respect to the Standard Hydrogen Electrode: see DFT Methodology).

Comment: it can be seen from Table S15 that the most varying experimental redox potential is that of reduction (1.14 eV range) whereas the range of variation at oxidation is of only 0.19 eV. Both behaviors are related to the fact that, when considering Ionization potentials and solvation energy differences in Table S15, the main variation comes from IP(-1), which is directly related to that of E_{red} (= IP(-1) + $\Delta E_{solv}(-1)$ -4.28). In turn, this is related to the fact that the LUMOs (in the neutral oligomers) or the SOMOs (in the reduced oligomers) molecular energies go down from monomer to dimer to trimer (see Figure S45). This in turn is correlated with the corresponding reduction of the HOMO-LUMO gaps (3.56 eV, 2.97 eV and 2.90 eV, respectively from monomer to trimer: see Table S12). On the other hand, at oxidation, an electron is removed from an electronic quasi-band of nearly-degenerate and extended molecular orbitals (cf. Computational Methods), with little impact on IP(0) and, therefore, on E_{ox}.

Orbitals visualization

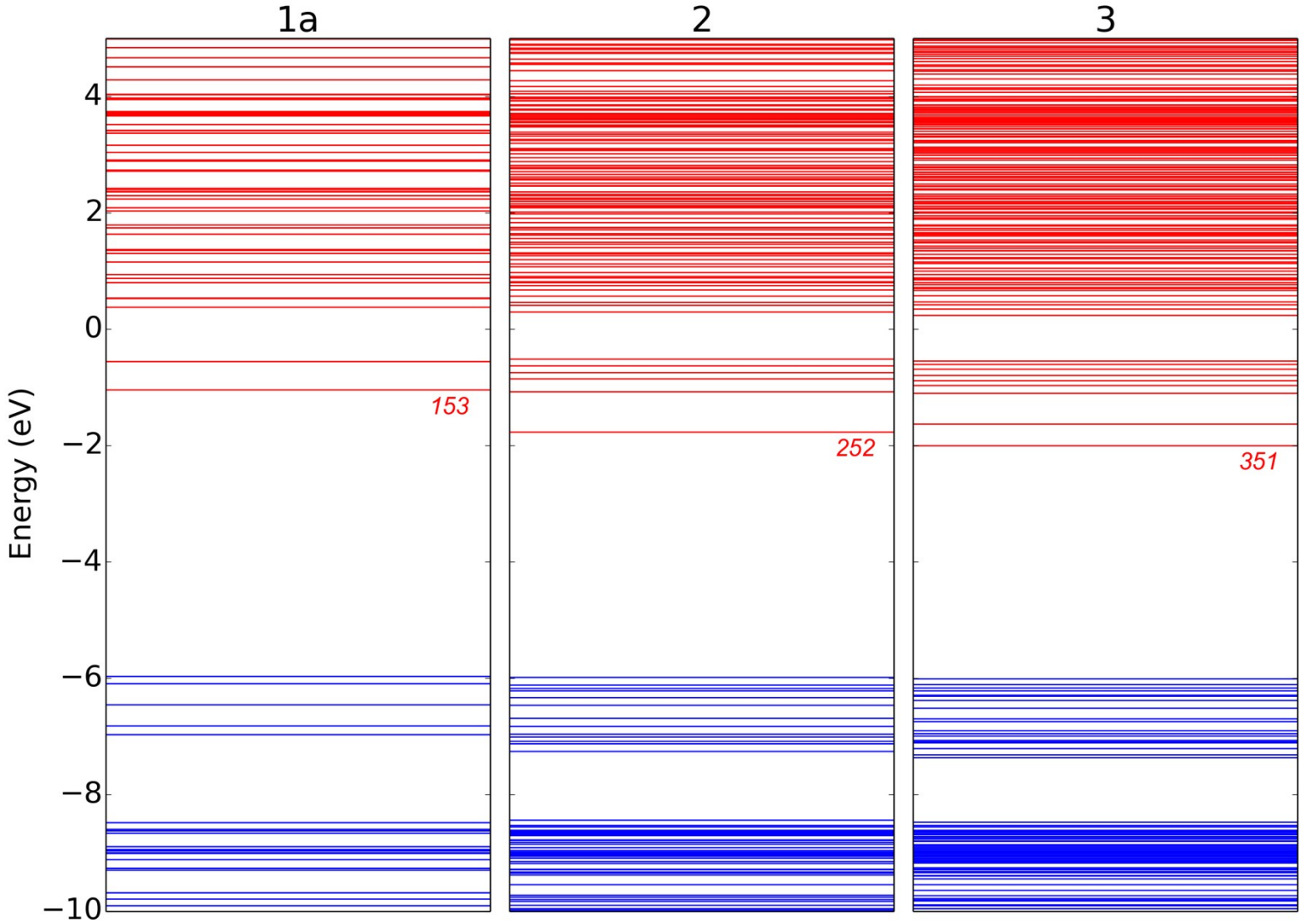

Figure S45 : Partial energy orbital diagrams for neutral 1a, 2 and 3. In blue, occupied orbitals; in red, empty orbitals. Energy range [-10, 5]eV around the HOMOI-LUMO gaps.

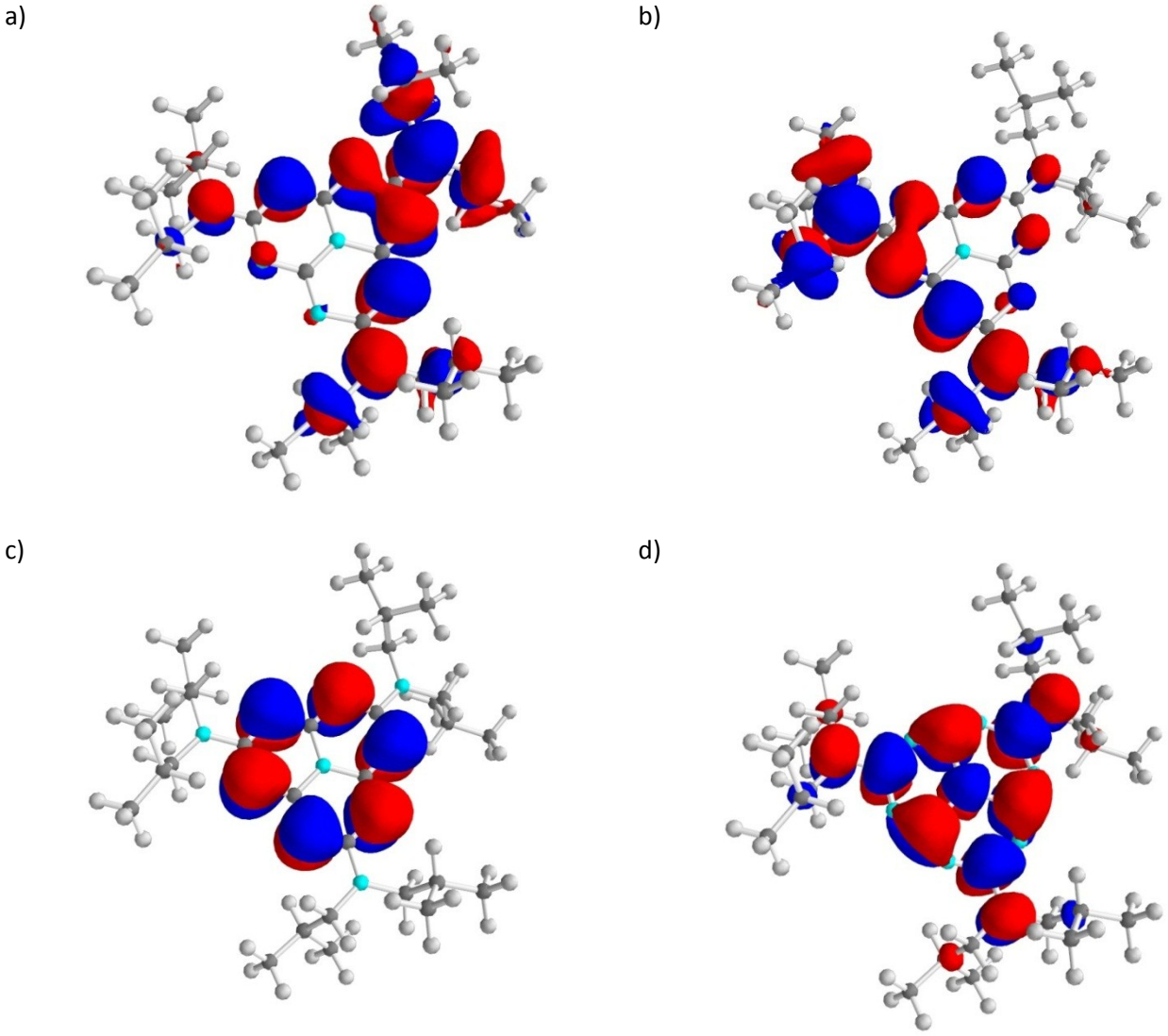

Figure S46 : Computed orbitals for **1a**: a) 150 (HOMO -2), b) 151 (HOMO -1), c) 152 (HOMO) and d) 153 (LUMO) Orbitals 150 and 151 are nearly degenerate (0.004eV difference).

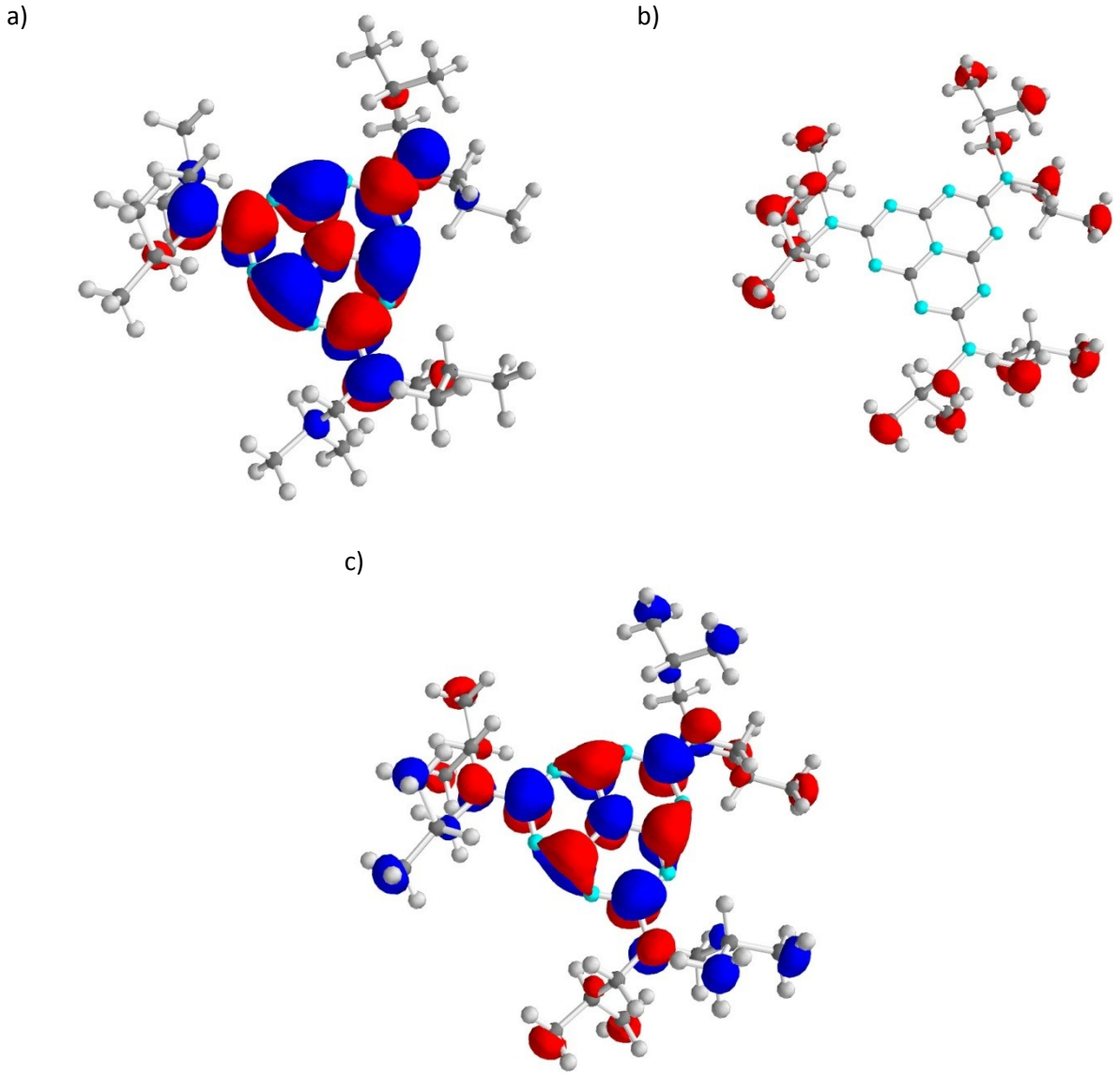

Figure S47 : Computed orbitals for reduced **1a**: a) 153α (SOMO), b) 153β (LUMO) and c) 158α (LUMO +5).

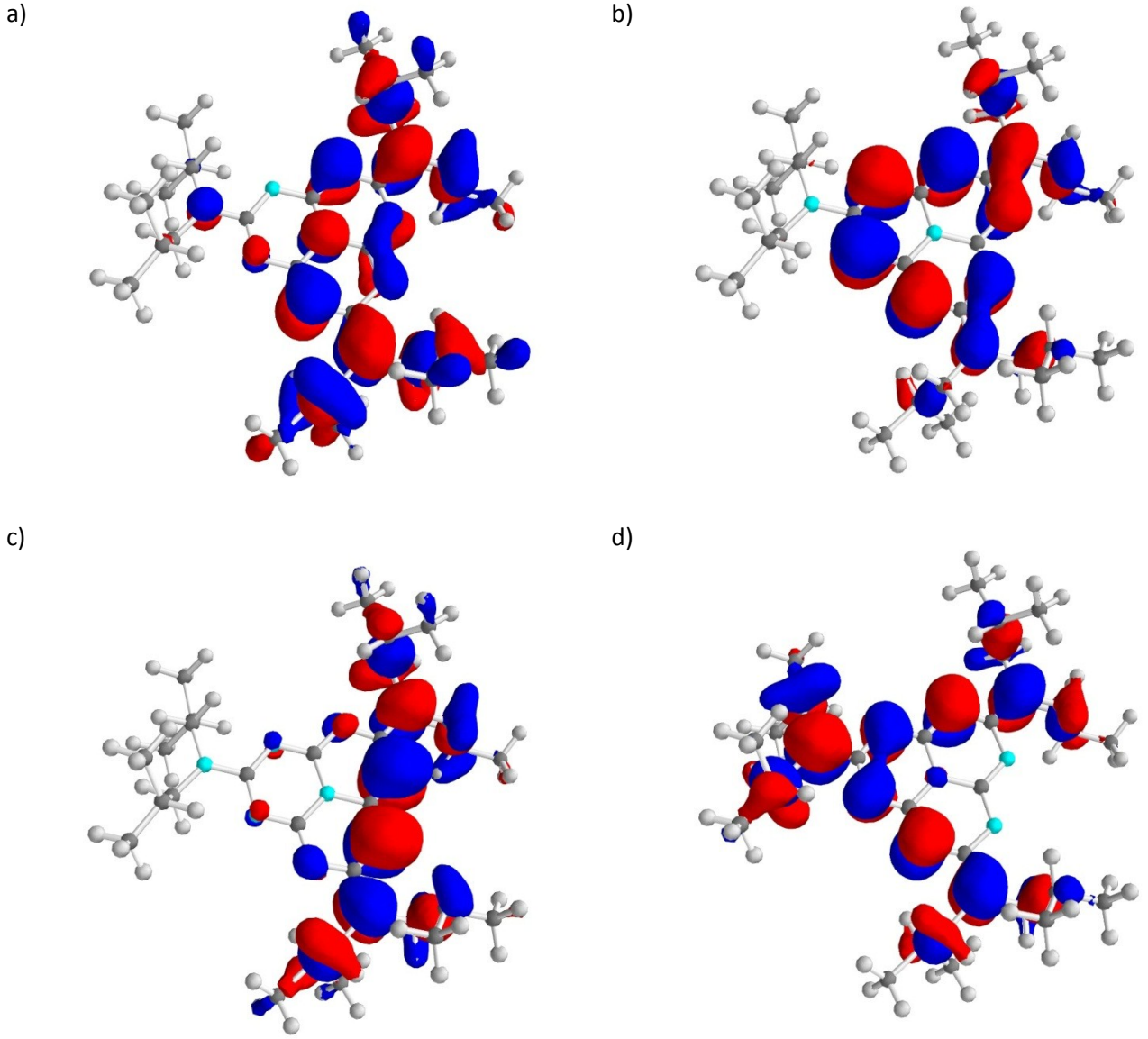

Figure S48 : Computed orbitals for oxidized **1a**: a) 150α (HOMO -2), b) 151α (HOMO -1), c) 152α (SOMO) and d) 152β (LUMO)
Orbitals 150α and 151α are nearly degenerate (0.044eV difference)

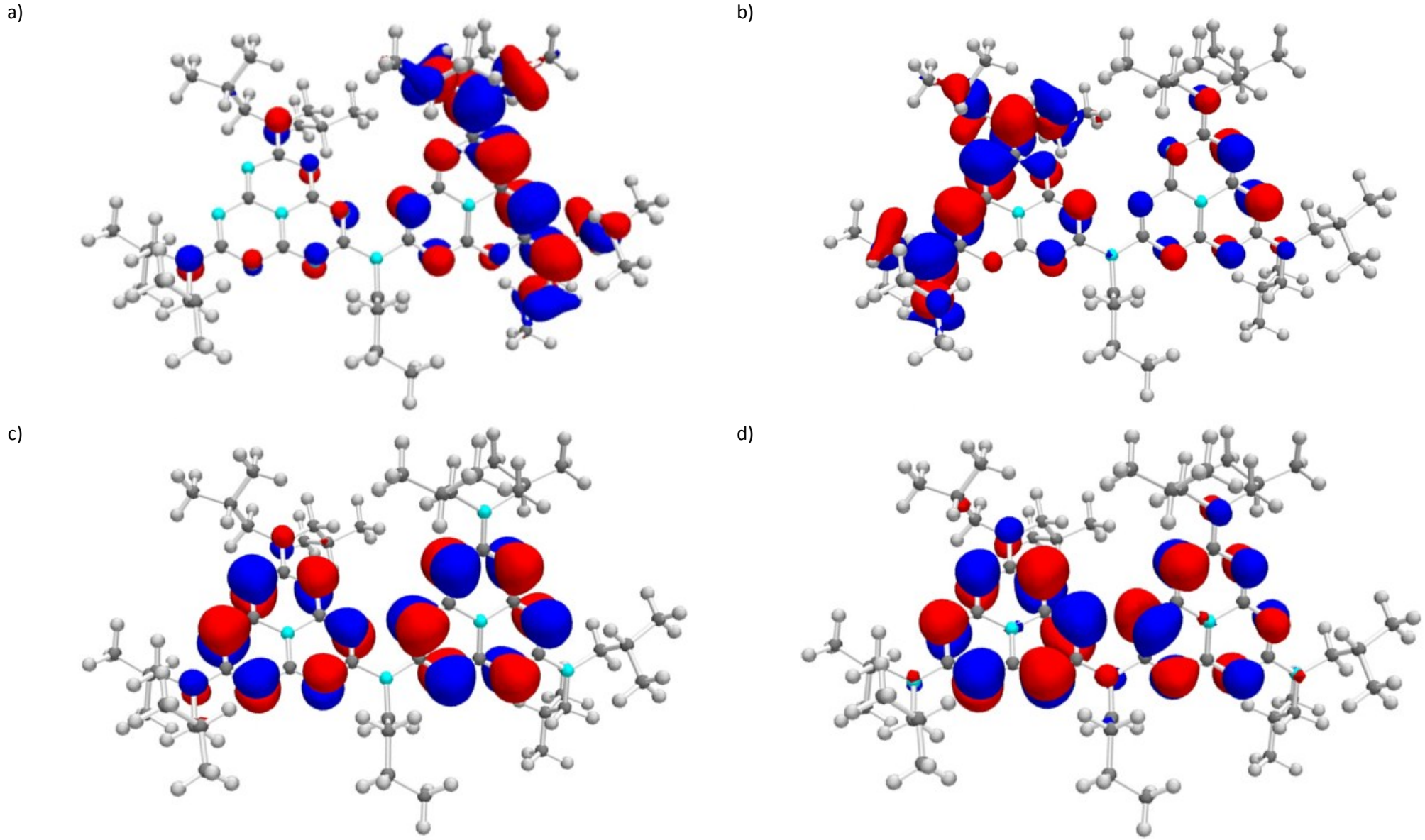

Figure S49: Computed orbitals for **2**: a) 248 (HOMO -3), b) 249 (HOMO -2), c) 250 (HOMO -1) and d) 251 (HOMO) Orbitals 248 and 249 are nearly degenerate (0.041eV difference).

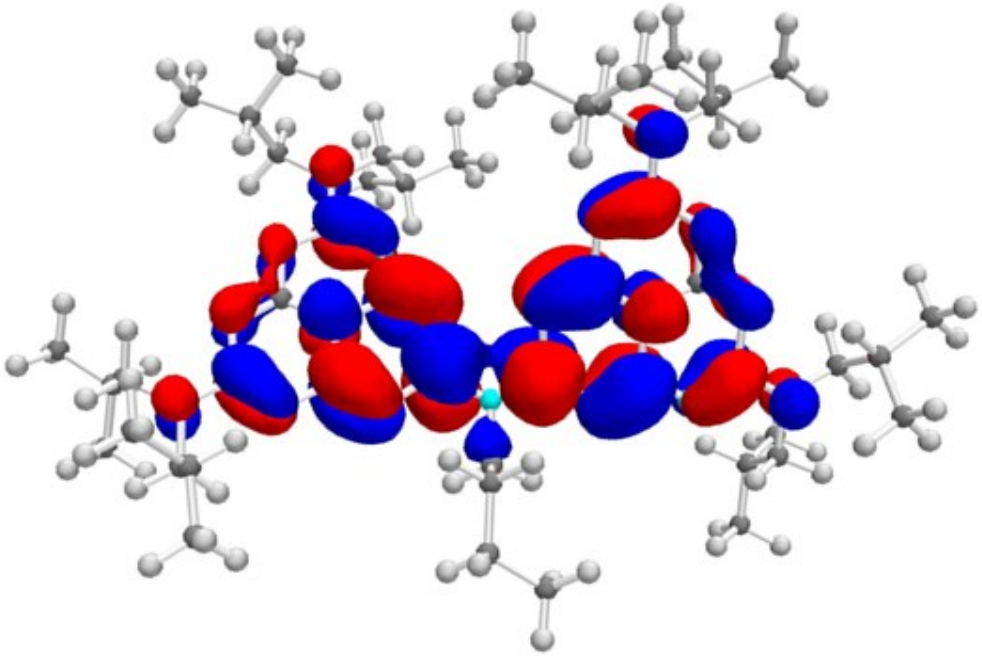

Figure S50 : Computed orbital 252 (LUMO) for **2**.

a)

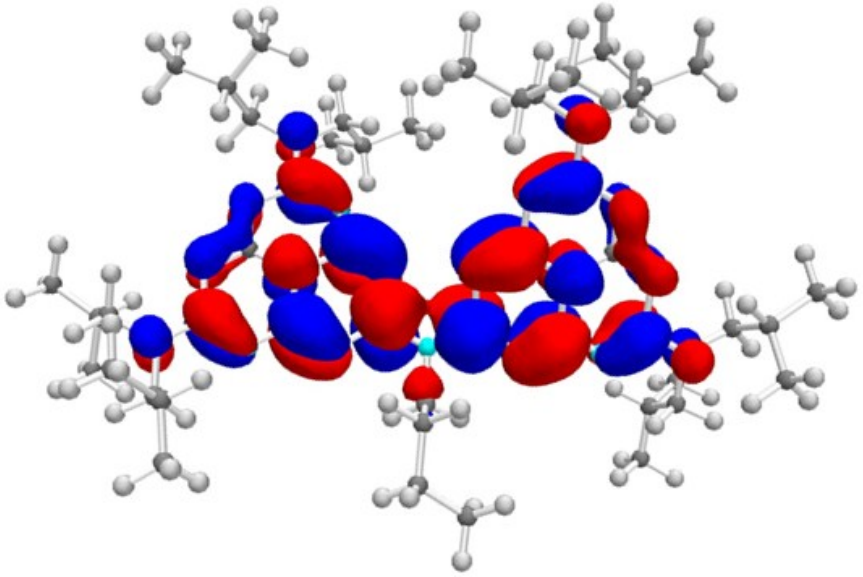

b)

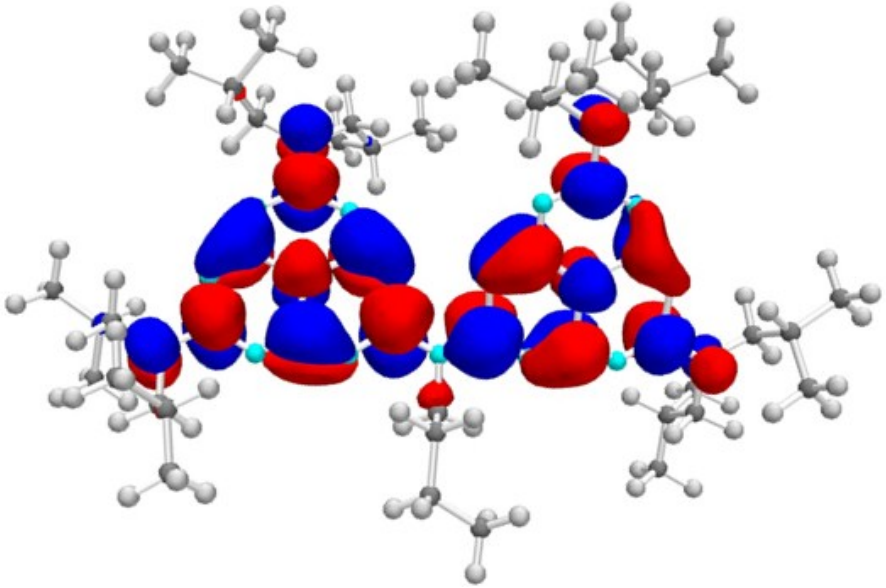

Figure S51 : Computed orbitals for reduced **2**: a) 252α (SOMO) and b) 252β (LUMO).

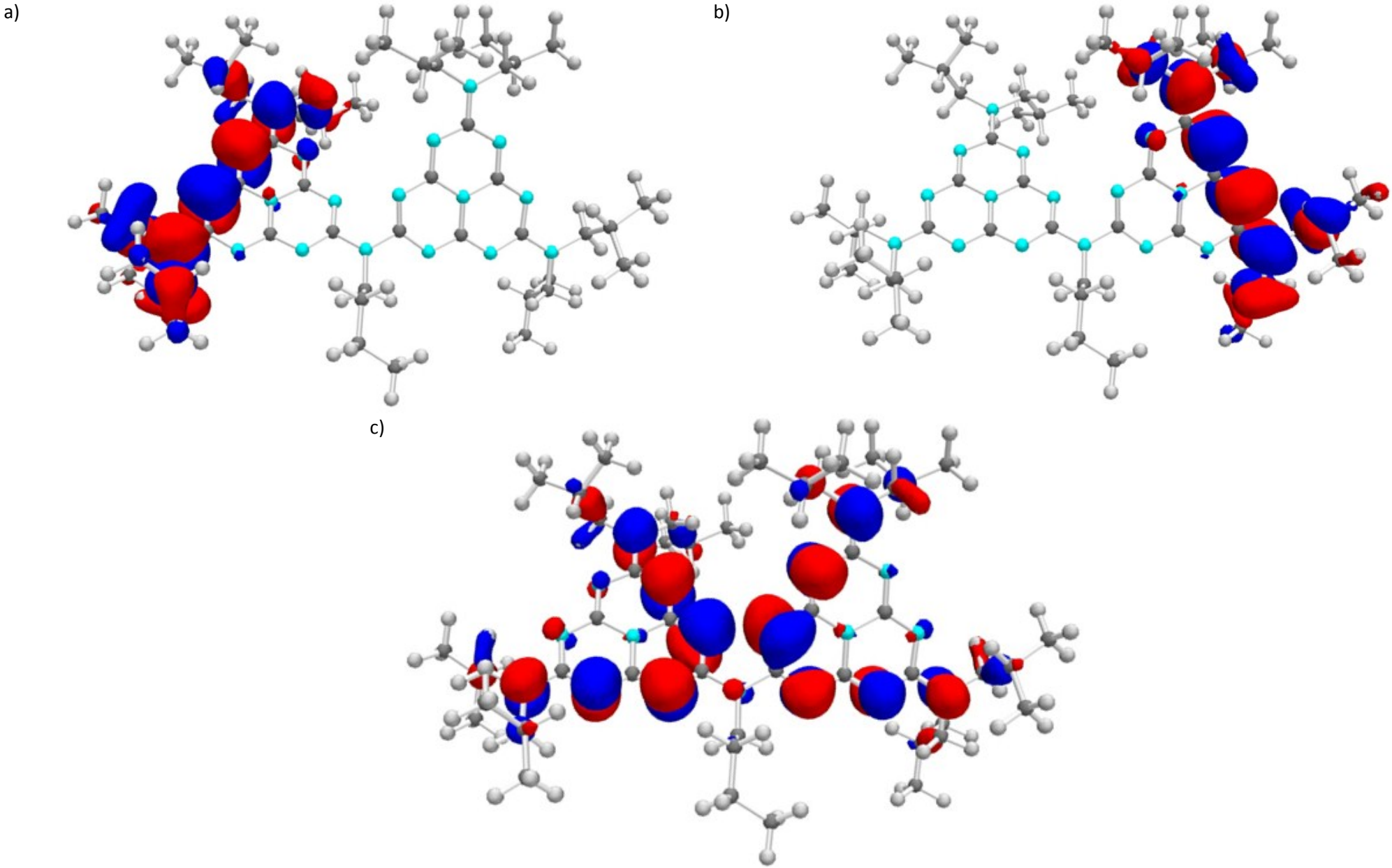

Figure S52: Computed orbitals for oxidized **2**: a) 250α (HOMO -1), b) 251α (SOMO) and c) 251β (LUMO) Orbitals 250α and 250β are nearly degenerate (0.024eV difference).

a)

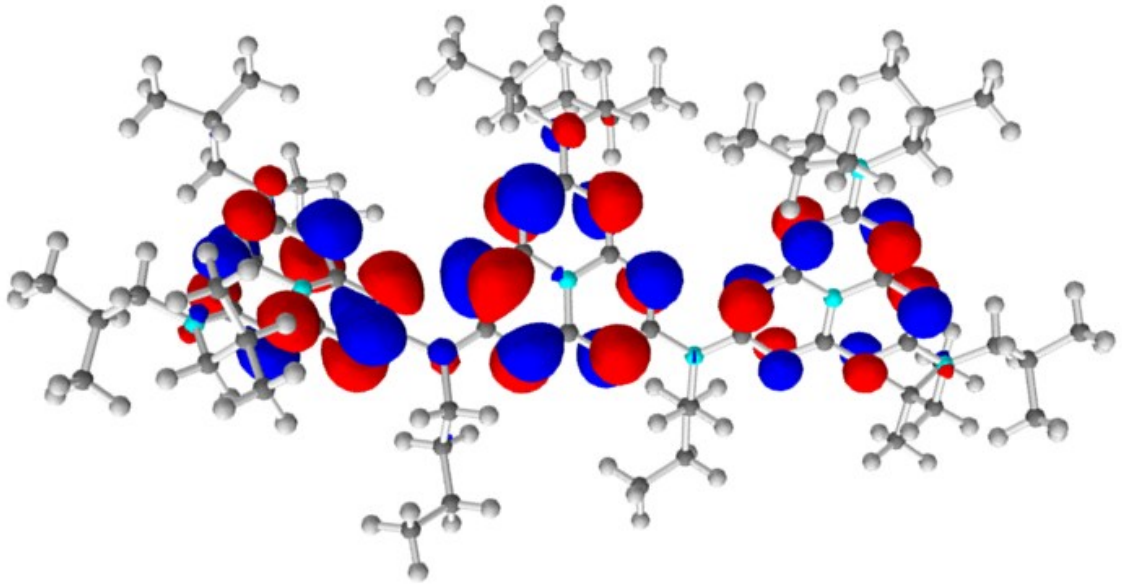

b)

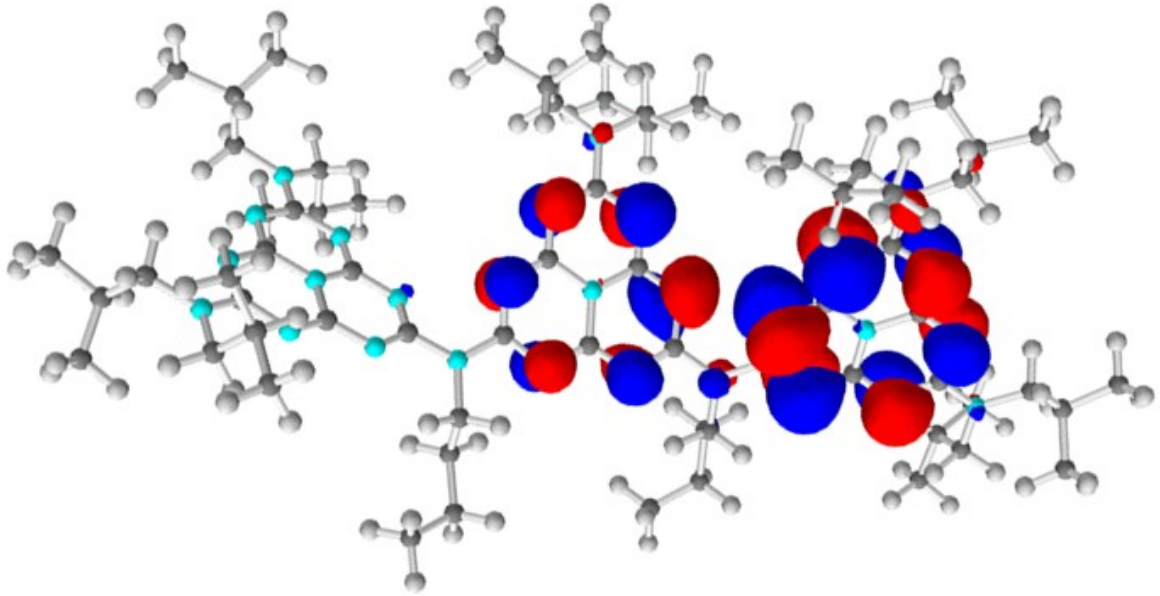

Figure S53 : Computed orbitals for **3**: a) 349 (HOMO -1) and b) 350 (HOMO)
Orbitals 349 and 350 are nearly degenerate (0.099eV difference).

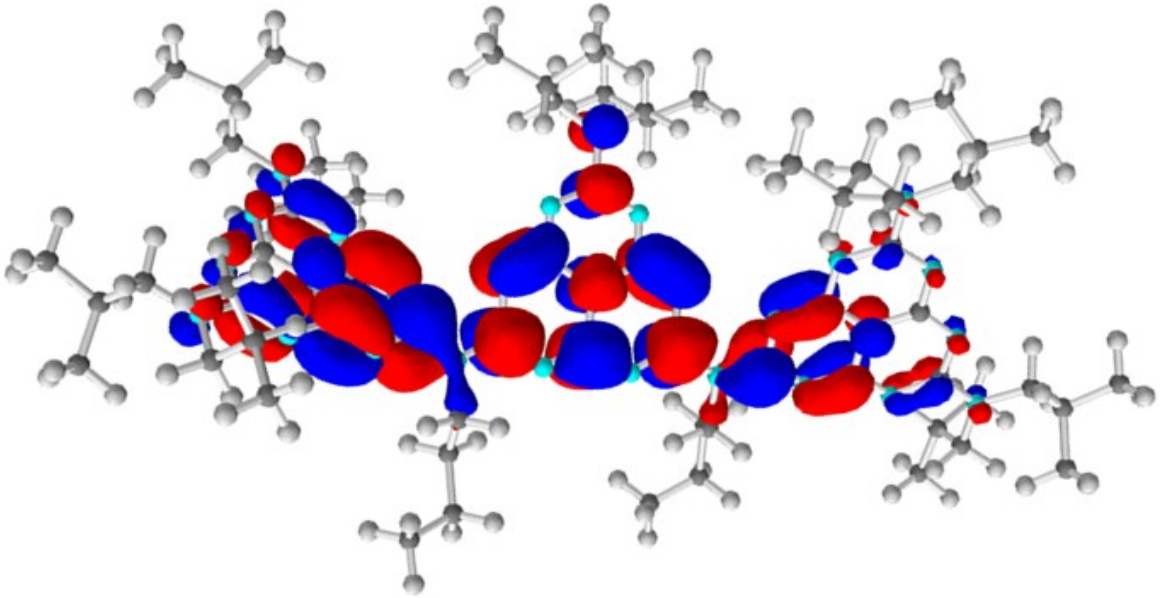

Figure 54 : Computed orbital 351 (LUMO) for **3**.

a)

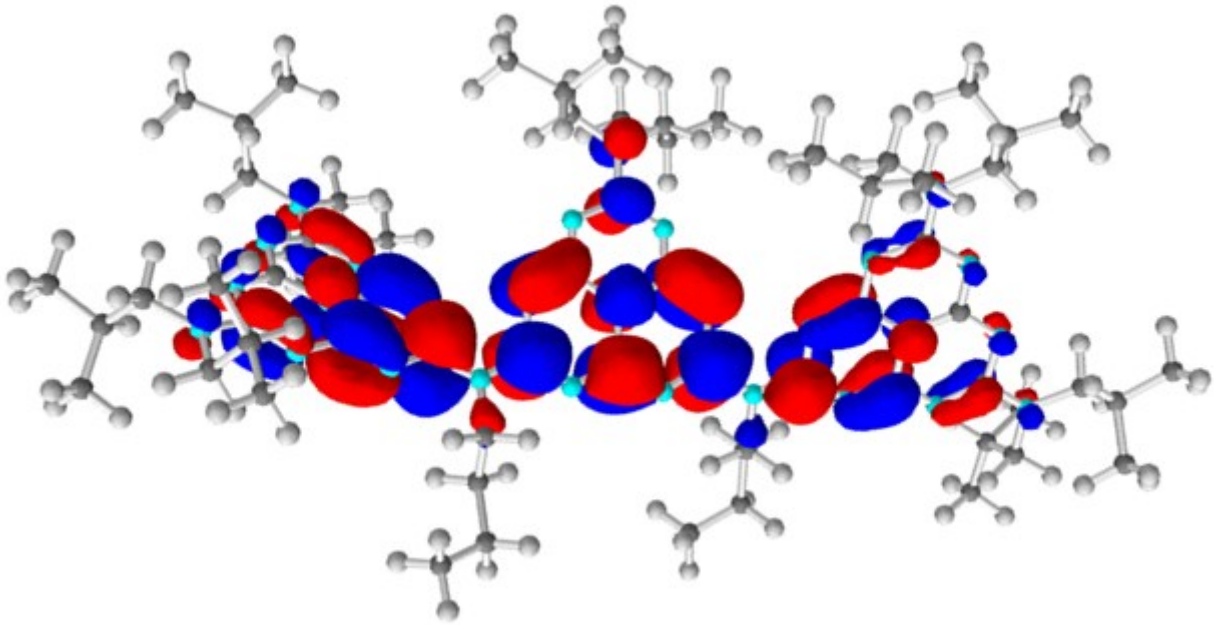

b)

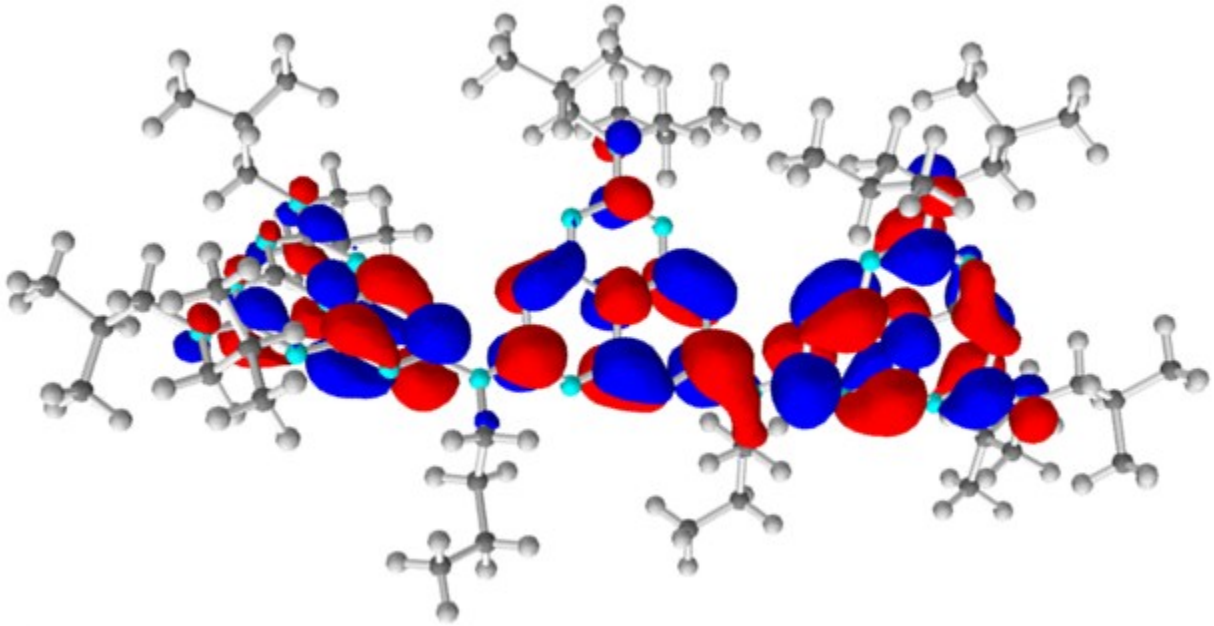

Figure S55 : Computed orbitals for reduced **3**: a) 351α (SOMO) and b) 351β (LUMO).

a)

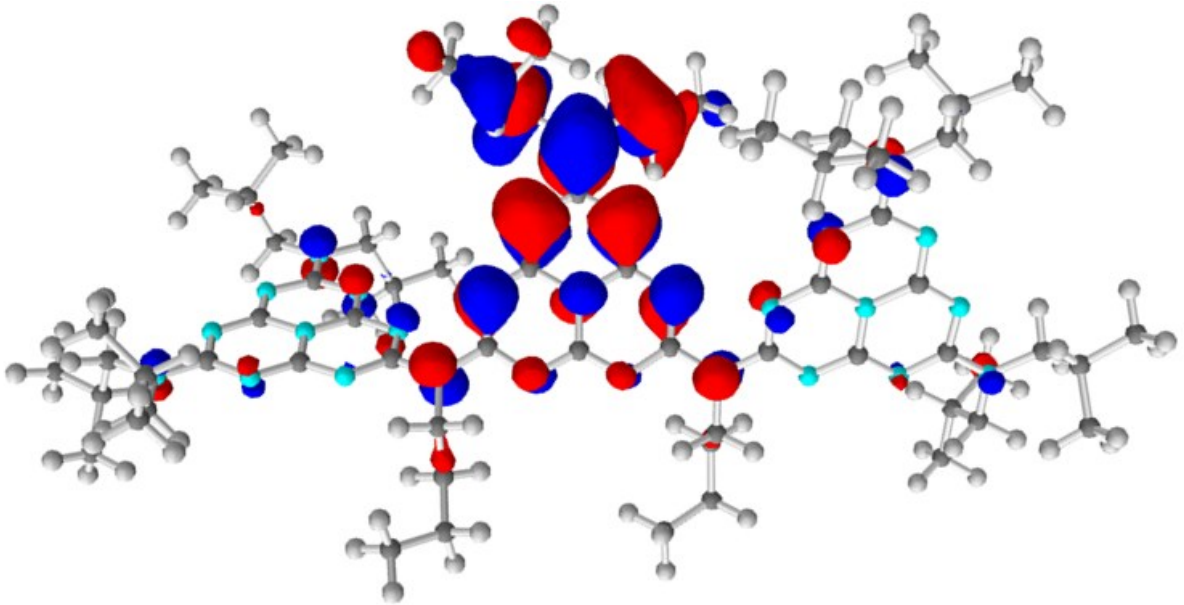

b)

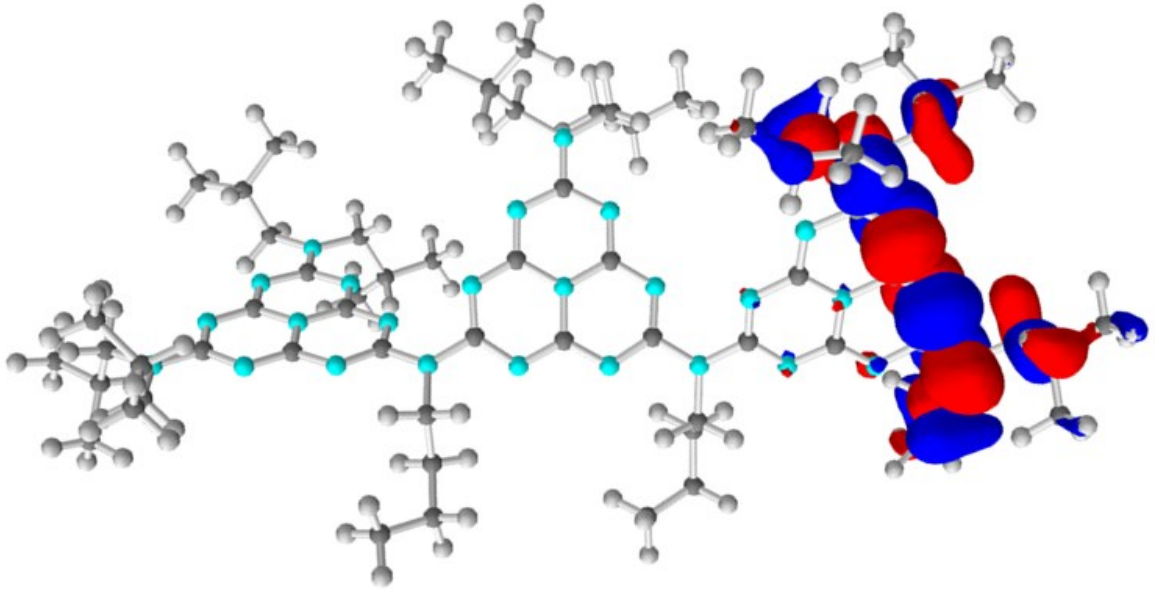

Figure S56: Computed orbitals for oxidized **3**: a) 348α (HOMO -2) and b) 349α (HOMO -1)
Orbitals 349α and 350α are nearly degenerate (0.028eV difference).

a)

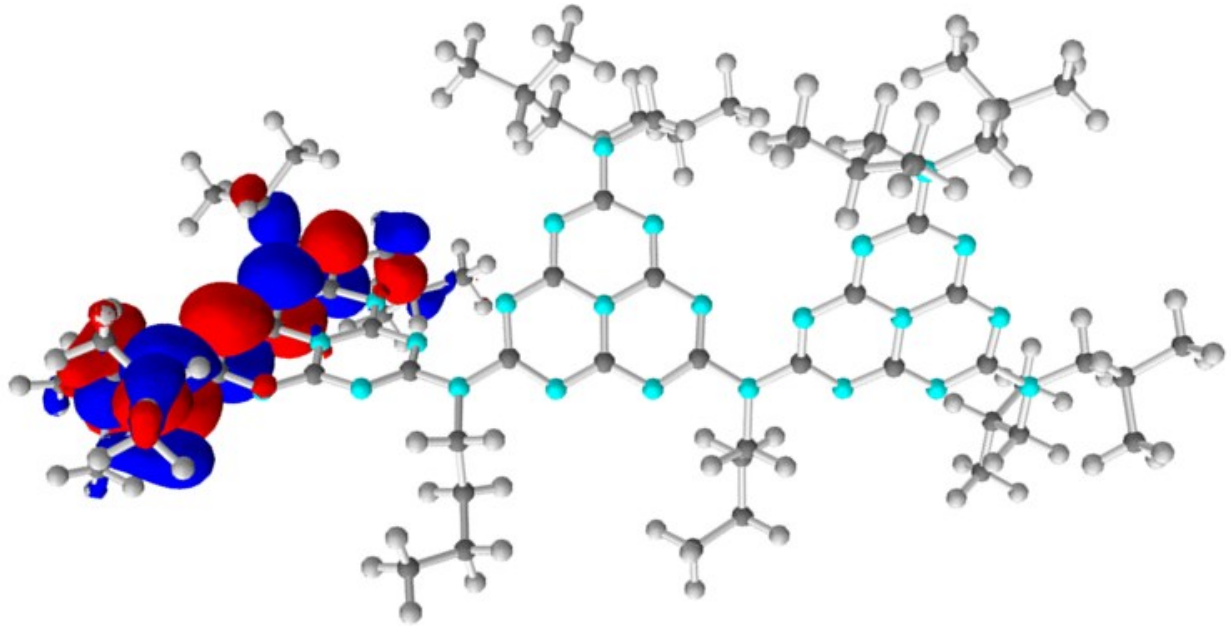

b)

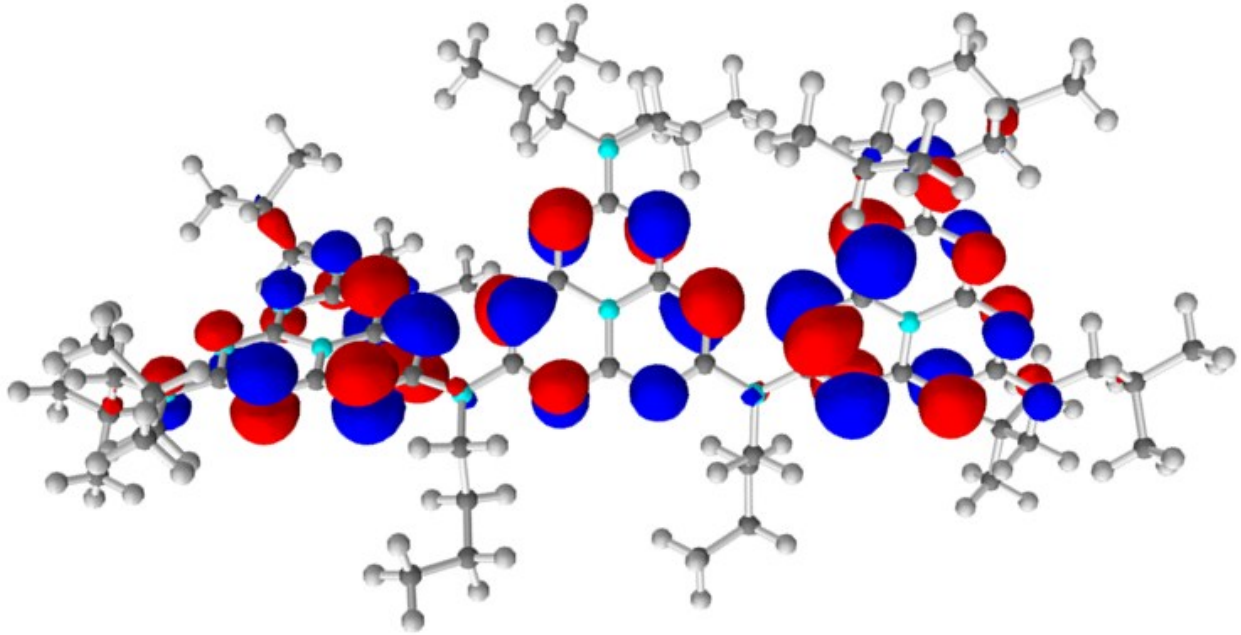

Figure S57: Computed orbitals for oxidized **3**: a) 350α (SOMO) and b) 350β (LUMO).

XPS Characterization

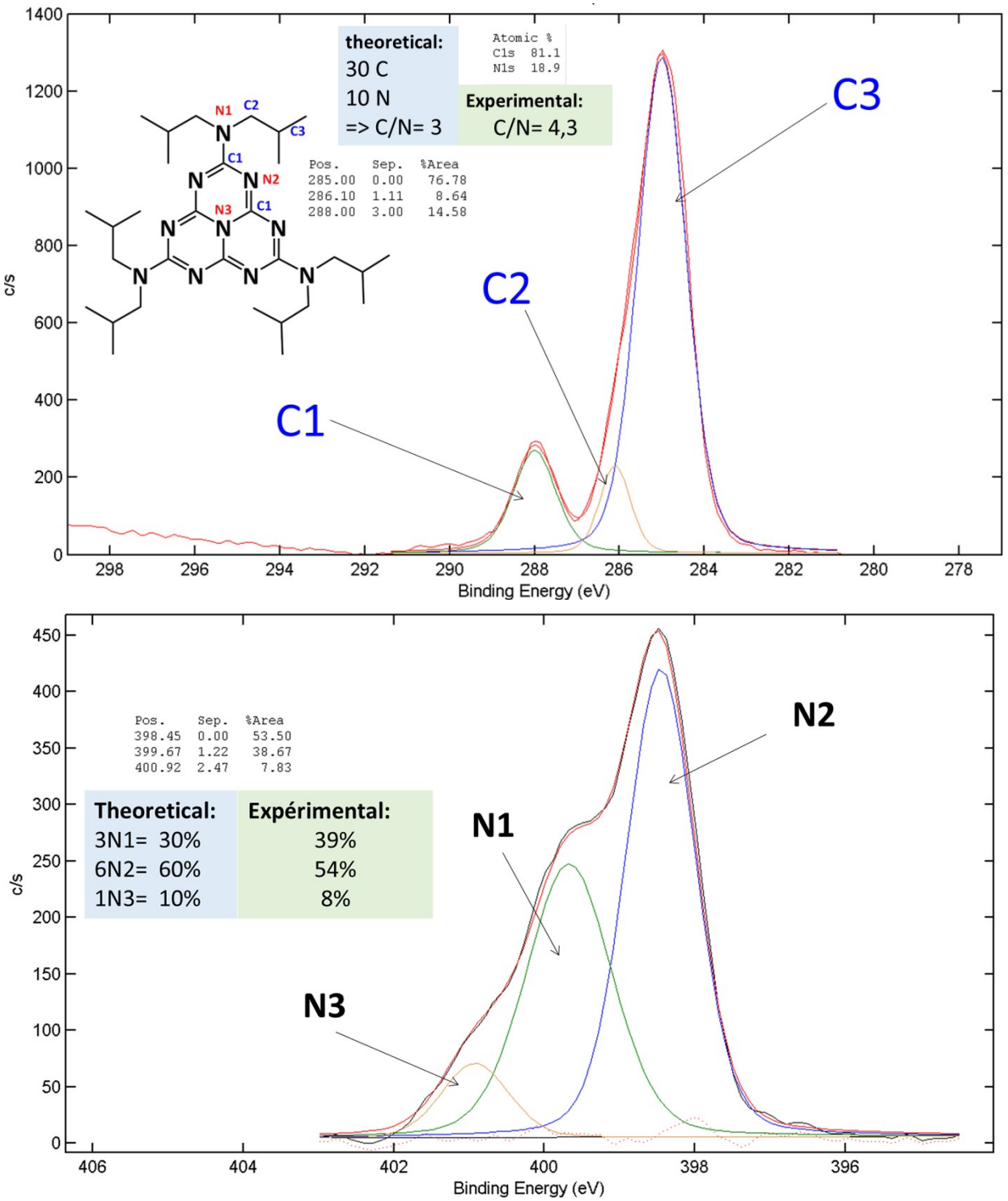

Figure S58: XPS spectra of **1a**, top C1s spectra, bottom C2s spectra.

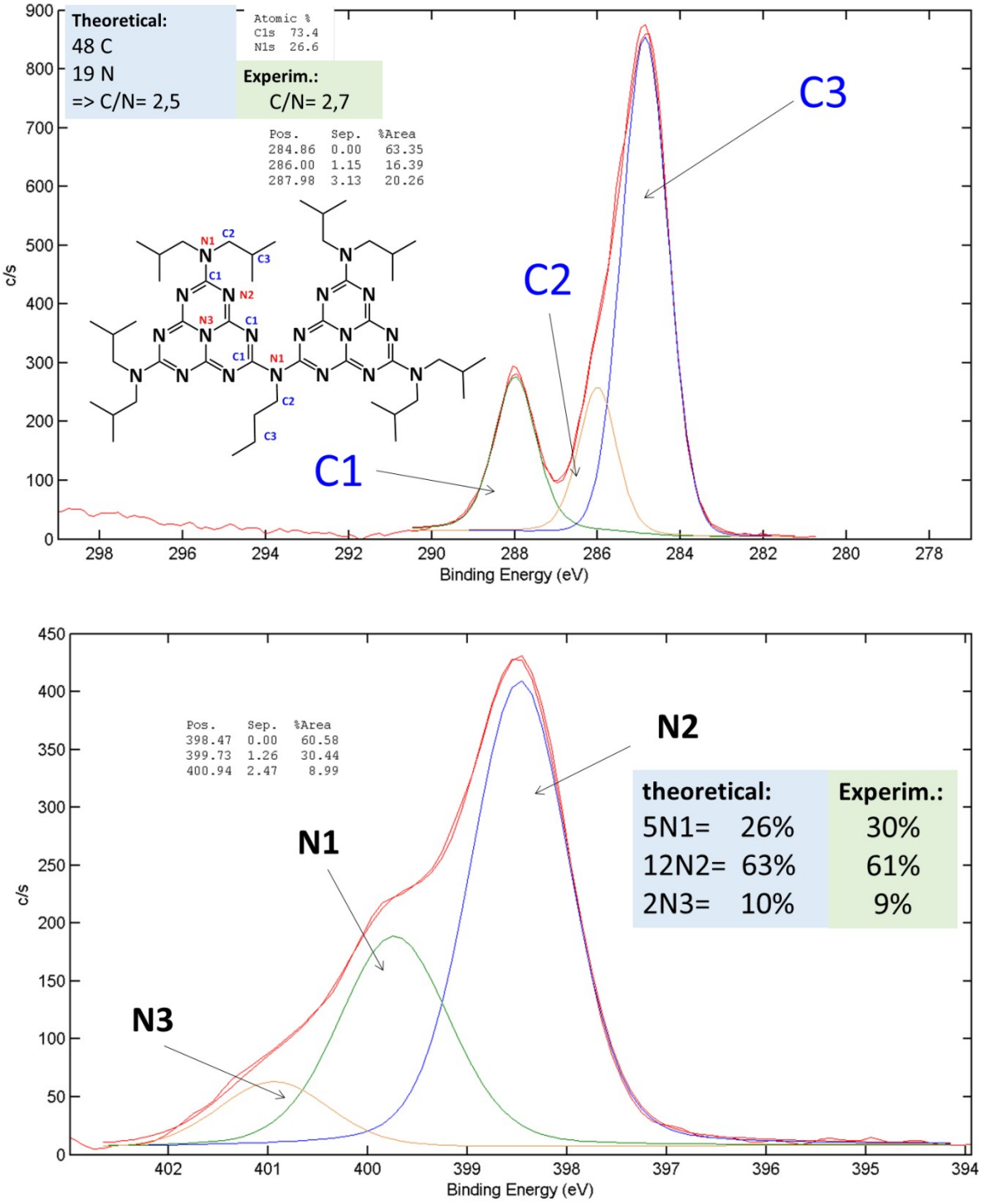

Figure S59: XPS spectra of **2**, top C1s spectra, bottom C2s spectra.

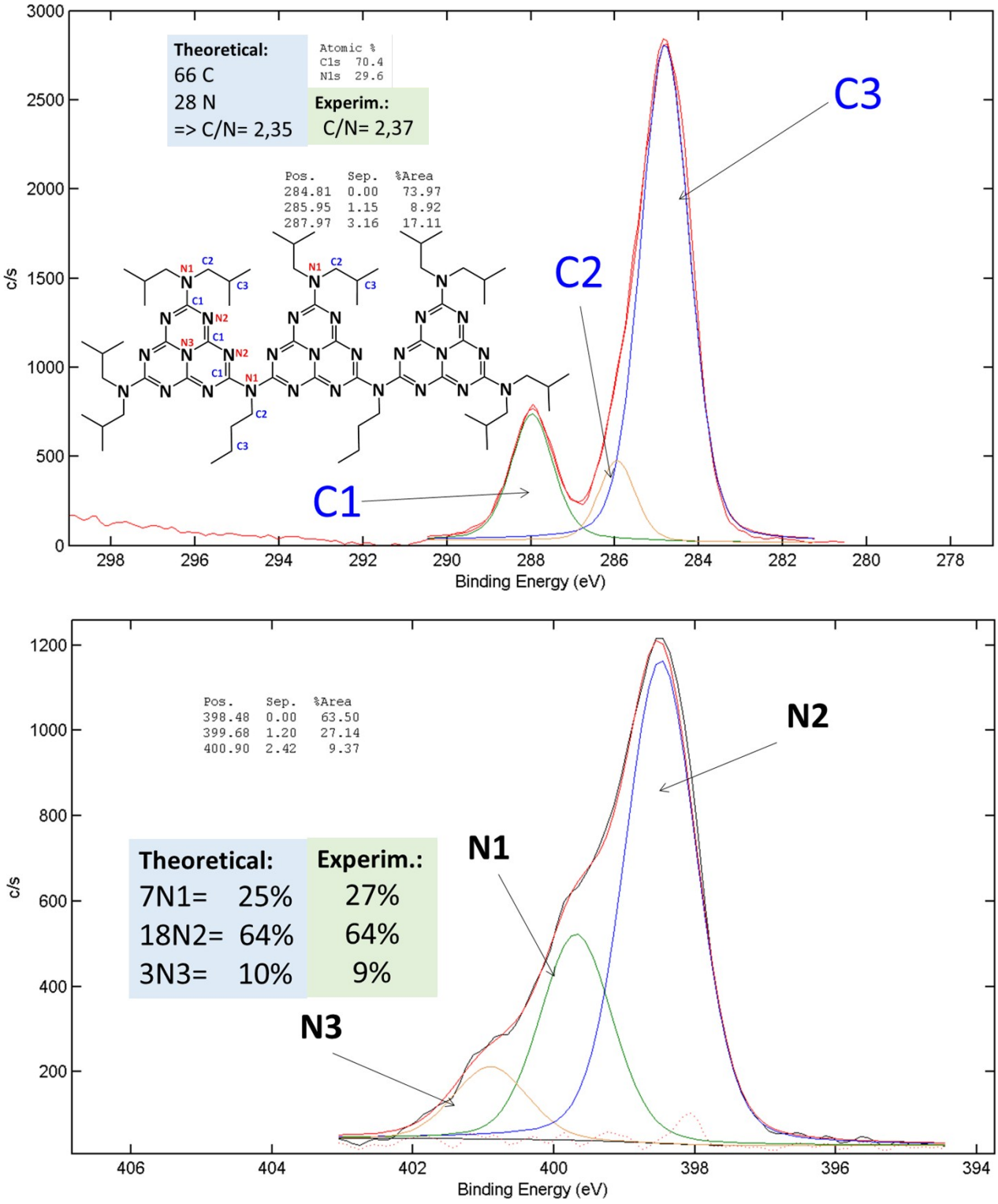

Figure S60: XPS spectra of **3**, top C1s spectra, bottom C2s spectra.

References

[1] E. Kroke, M. Schwarz, E. Horath-Bordon, P. Kroll, B. Noll, A. D. Norman, *New J. Chem.* **2002**, *26*, 508-512.

[2] V. V. Pavlishchuk, A. W. Addison, *Inorganica Chimica Acta* **2000**, *298*, 97-102.

[3] I. Noviandri, K. N. Brown, D. S. Fleming, P. T. Gulyas, P. A. Lay, A. F. Masters, L. Phillips, *Journal of Physical Chemistry B* **1999**, *103*, 6713-6722.

[4] G. t. Velde, E. J. Baerends, *Journal of Computational Physics* **1992**, *99*, 84 - 98.

[5] S. H. Vosko, L. Wilk, M. Nusair, *Canadian Journal of Physics* **1980**, *58*, 1200-1211.

[6] A. D. Becke, *Phys. Rev. A* **1988**, *38*, 3098–3100.

[7] J. P. Perdew, *Phys. Rev. B* **1986**, *33*, 8822–8824.

[8] aA. D. Becke, *The Journal of Chemical Physics* **1993**, *98*, 1372-1377; bC. Lee, W. Yang, R. G. Parr, *Phys. Rev. B* **1988**, *37*, 785–789.

[9] aA. Klamt, *The Journal of Physical Chemistry* **1995**, *99*, 2224-2235; bA. Klamt, V. Jonas, *The Journal of Chemical Physics* **1996**, *105*, 9972-9981; cA. Klamt, G. Schuurmann, *J. Chem. Soc., Perkin Trans. 2* **1993**, 799-805.

[10] A. A. Isse, A. Gennaro, *The Journal of Physical Chemistry B* **2010**, *114*, 7894-7899.

[11] D. Ghosh, A. Roy, R. Seidel, B. Winter, S. Bradforth, A. I. Krylov, *The Journal of Physical Chemistry B* **2012**, *116*, 7269-7280.

[12] O. V. Gritsenko, P. R. T. Schipper, E. J. Baerends, *Chemical Physics Letters* **1999**, *302*, 199 - 207.

[13] aF. Kootstra, P. L. de Boeij, J. G. Snijders, *The Journal of Chemical Physics* **2000**, *112*, 6517-6531; bP. Romaniello, P. L. de Boeij, *The Journal of Chemical Physics* **2007**, *127*, -.

[14] H. Stoll, C. M. E. Pavlidou, H. Preuss, *Theoretica Chimica Acta* **1978**, *49*, 143-149.

[15] G. Berggren, A. Adamska, C. Lambertz, T. R. Simmons, J. Esselborn, M. Atta, S. Gambarelli, J. M. Mouesca, E. Reijerse, W. Lubitz, T. Happe, V. Artero, M. Fontecave, *Nature* **2013**, *499*, 66-+.

[16] B. Spingler, S. Schnidrig, T. Todorova, F. Wild, *CrystEngComm* **2012**, *14*, 751-757.

[17] aM. Oki, *Applications of Dynamic NMR Spectroscopy to Organic Chemistry, Vol. 4*, Deerfield Beach: Florida, USA, **1985**; bJ. Sandström, *Dynamic NMR spectroscopy*, London, **1982**.

[18] CrysAlisPro, 1.171.37.35 ed., Agilent Technologies, **2013**.

[19] R. C. Clark, J. S. Reid, *Acta Crystallographica Section A* **1995**, *51*, 887–897.

[20] L. Palatinus, G. Chapuis, *Journal of Applied Crystallography* **2007**, *40*, 786–790.

[21] I. J. Bruno, J. C. Cole, P. R. Edgington, M. Kessler, C. F. Macrae, P. McCabe, J. Pearson, R. Taylor, *Acta Crystallographica Section B* **2002**, *58*, 389–397.